The Dissertation Committee for Susana Carranza Certifies that this is the approved version of the following dissertation:

Modeling of Oxygen Scavenging Polymers and Composites

Committee:

Roger T. Bonnecaze , Supervisor

Don R. Paul

Benny D. Freeman

Christopher W. Bielawski

Robert Moser

Modeling of Oxygen Scavenging Polymers and Composites

by

Susana Carranza, B.S.; M.S.

Dissertation

Presented to the Faculty of the Graduate School of

The University of Texas at Austin

in Partial Fulfillment

of the Requirements

for the Degree of

Doctor of Philosophy

The University of Texas at Austin

December, 2010

Dedication

To Sergio, my loving husband, best friend and soul mate. You always knew what to say to cheer me up when things got difficult, and were always there to celebrate the small victories along the way.

Acknowledgements

First, I would like to thank my employer Darby Makel for providing enough flexibility in my work schedule, enabling me to balance work and school duties. His patience over the last four and a half years, and in particular during the final three months, was critical to my ability to complete my graduate studies.

I would like to thank Professors Don Paul and Benny Freeman, as this project was motivated by the experimental research in their groups. Professor Don Paul greatly contributed to my understanding of scavenging polymers and how to interpret the modeling results from the perspective of designing barrier materials. I would like to thank Maria Chiara Ferrari, who initiated the modeling efforts; Kevin Tung for his data, images and discussions about experimental observations; and Richard Li for insights on scavenging chemistry.

Belonging to a great research group was a big part of my graduate experience. I would like to thank Derek Bassett for always being willing to answer questions about coding and computing in general. The lively conversations with Jyoti Seth and Babatunde Oguntade generated memories that will remain with me for a long time. Lavanya Mohan, Parag Katira and Michael Clements quickly became great lunch

companions and patient listeners, whenever my research would take unexpected wrong turns.

Finally, I would like to thank my advisor Professor Roger Bonnecaze. He was present and encouraging every step of the way, always knowing when to let me figure out my research path, or when to extend a hand to get me unstuck and moving in the right direction. Despite having a very busy schedule as the department chair, he always found the time to review my progress, provide feedback and meet whenever needed. It was great fortune to have an advisor that truly cared about my development as a student and a researcher. Thank you.

Modeling of Oxygen Scavenging Polymers and Composites

Publication No._____

Susana Carranza, Ph.D.

The University of Texas at Austin, 2010

Supervisor: Roger T. Bonnecaze

Polymers films and membranes with immobile and irreversible reactive sites can provide significant barrier properties for packaging materials. There is a need to develop mathematical models to understand the behavior of these reactive materials and to confidently extrapolate experimental data. Due to mechanical and optical requirements, barrier films may consist of composites, such as polymer blends and multilayer films with alternating reactive and inert layers. The reactive term that consumes the mobile species in the governing transport equations for such materials is a function of both the mobile species and the immobilized reactive sites, leading to non-linear partial differential equations that typically have to be solved numerically. Composite structures add to the complexity of the model. For the polymer blend, a multiscale model was developed, incorporating the reactive details within the particle into the bulk transport equation. For the multilayer film, initial conditions and diffusion coefficients were assigned independently for reactive or inert layers. The models developed for the three

configurations were solved numerically over a wide parameter space. Three regimes were identified, namely early times characterized by an initial flux plateau, and intermediate regime, and long times, characterized by the time lag. Asymptotic analysis of the homogeneous model was used to develop analytical predictions for the three regimes, obviating the need to numerically solve the model's non-linear equations. These predictions were generalized to polymer blends. For multilayer films, predictions for early and long times were developed. Results for polymer blends and multilayer composites were compared and discussions of the most suitable configuration for different scenarios were presented. The reactive barrier configurations studied require the knowledge of parameters such as reaction rates and coefficients of diffusion and solubility of the reactive polymer. Model and predictive equations have been developed to describe the transient mass uptake in reactive homogeneous films, enabling the extraction of these parameters from sorption experiments.

Table of Contents

List of Tables

List of Figures

Chapter 1: Introduction

1.1 BARRIER MATERIALS BACKGROUND

Polymers are widely used as packaging materials for a variety of applications, from food and drugs to consumer electronics, to prevent contamination by oxygen, water or other reactants. Many polymers provide some protection (table 1.1), but for applications where the contents are highly sensitive to environmental exposure (to oxygen or moisture), improved barrier properties are required (table 1.2). There are generally three approaches to improve barrier properties (Yang et al. 2001). The first approach is to seek polymers with intrinsically low permeability. The second approach is to introduce impermeable media in the polymer, such as clay platelets, to increase the tortuosity of the diffusion path. The third approach, which has been recognized since at least the 1960s, is to introduce additives such as adsorptive fillers or reactive additives to immobilize or consume the penetrant as it diffuses through the film (Finger et al. 1960; Paul 1969; Paul and Kemp 1973; Paul and Koros 1976). While the first two approaches reduce the steady-state permeation, the third approach seeks to substantially reduce the transient flux and increase the transition time, or time lag θ, to the steady-state flux of an unwanted mobile species. The earliest examples involve adsorption by filler particles, however, in more recent times interest has turned to incorporation of reactive components.

Table 1.1: Typical properties of polymers used in food packaging.

Polymer	O_2 Permeability, 25°C (STD cm^3mil/100 in^2day atm)	Tensile Strength (1000 psi)	Tensile Modulus (1000 psi)
PET	3.0-6.1	7.0-10.5	400-600
HDPE	100-185	2.5-6.5	90-158
PP	130-240	4.5-6.0	165-225
PS	250-380	5.2-7.5	330-475
PC	300	9.1-10.5	345
LDPE	400-450	1.2-4.6	25-75
MXD6	0.13-1.03	14.5	681
EVOH	$5x10^{-3}$-0.3	5.4-13.6	--
SBS	6700	4.6	--

PET - polyethylene terephthalate, HDPE - high density polyethylene, PP - polypropylene, PS - polystyrene, PC - polycarbonate, LDPE - low density polyethylene (data adapted from Hui 2005)
EVOH – copolymer of ethylene and vinyl alcohol (data range for EVAL™ per Kuraray brochure)
MXD6 – copolymer of m-xylylenediamine and adipic acid (data range for oriented and non-oriented versions per Mitsubishi Gas Chemical Company brochure)
SBS – styrene butadiene styrene block copolymer (data for Kraton D1102, 30% styrene – tensile strength per Kraton brochure, permeability measured by Kevin Tung, University of Texas at Austin)

One example of reactive components is the use of oxygen-scavenging polymers (OSP), which irreversibly and specifically consume oxygen. A number of patents have been issued describing variations on this idea for food and beverage packaging (Cochran et al. 1991; Speer et al. 1993, 1996; Katsumoto and Ching 1998; Blinka et al. 1998; Cahill and Chen 2000; Stewart et al. 2006). New polymer barrier materials that react or

absorb undesirable permeates are also being developed for products that are highly sensitive to oxygen or moisture, such as organic light emitting diodes (OLEDs) for flexible displays, that require oxygen flux < $7x10^{-7}$ STD $cm^3/100\ in^2day$ ($5x10^{-8}$ $\mu mol/cm^2day$) to achieve 10,000 hours lifetime needed for commercial viability (Burrows et al. 2001, Lewis 2006, Choi et al. 2008).

Table 1.2: Oxygen barrier requirements for various foods and beverages.

Food/beverage	**Max Tolerable O_2 Gain [a] PPM**	**Max O_2 Flux[b] STD $cm^3/100\ in^2day(\mu mol/cm^2day)$**	
		1 month	**6 months**
Beer	1-2	$2.7\text{-}5.4x10^{-5}$ ($1.9\text{-}3.8x10^{-6}$)	$4.5\text{-}9.1x10^{-6}$ ($3.1\text{-}6.3x10^{-7}$)
Canned vegetables and soups, baby food	2-5	$5.4\text{-}14x10^{-5}$ ($3.8\text{-}9.4x10^{-6}$)	$9.1\text{-}23x10^{-6}$ ($6.3\text{-}16x10^{-7}$)
Tomato based products	3-8	$8.2\text{-}22x10^{-5}$ ($5.6\text{-}15x10^{-6}$)	$1.4\text{-}3.6x10^{-5}$ ($9.4\text{-}25x10^{-7}$)
High acid fruit juices	8-20	$2.2\text{-}5.4x10^{-4}$ ($1.5\text{-}3.8x10^{-5}$)	$3.6\text{-}9.1x10^{-5}$ ($2.5\text{-}6.3x10^{-6}$)
Oils, shortenings, salad dressings	20-100	$5.4\text{-}27x10^{-4}$ ($3.8\text{-}19x10^{-5}$)	$9.1\text{-}45x10^{-5}$ ($6.3\text{-}31x10^{-6}$)
Jams, jellies, liquor	50-200	$1.4\text{-}5.4x10^{-3}$ ($9.4\text{-}38x10^{-5}$)	$2.3\text{-}9.1x10^{-4}$ ($1.6\text{-}6.3x10^{-5}$)

a) Coles et al. 2003
b) Flux based on 500 cm^3 package, 390 cm^2 (60 in^2) surface area

This dissertation focuses on developing numerical and analytic models describing the third approach discussed above, namely utilizing reactive membrane barriers that react or absorb and effectively immobilize the diffusion of an unwanted species.

Polybutadiene is an example of a polymer that readily oxidizes (Tobolsky et al. 1950; Bauman and Maron 1956; Beaven and Phillips 1974; Rabek et al. 1979; Ivanov et al. 1979; Adam et al. 1989; Piton and Rivaton 1996) particularly in the presence of certain metal catalysts (Sheldon and Kochi 1981). The rate of oxygen uptake by scavenging polymers involves a diffusional process in addition to reaction kinetics (Gillen and Clough 1992, Rincon-Rubio et al. 2001, Coquillat et al. 2007 a, b, c). Colloidal desiccants such as silica gel (Lehto and Lankinen 2004; Ng and Mintova 2008) may be used as a water barrier, and a combination of polybutadiene and silica gel may be used to block both species simultaneously. It is anticipated that incorporation of reactive sites will lead to time lags on the orders of months or even years, making complete experimental characterization impractical. This dissertation studies reactive films where the mobile species reacts irreversibly with the immobilized reactive sites, and the rate of consumption depends on the local concentration of mobile and immobilized species. Furthermore, the problem of interest focuses on packaging applications, where one boundary is exposed to a high concentration of the mobile species and the other boundary is exposed to a vanishingly small concentration.

1.2 COMPOSITE BARRIERS

Oxygen scavenging polymers typically lack adequate structural properties so they are usually employed as composites, such as polymer blends and multilayer films, as illustrated in figure 1.1. For instance, a butadiene-containing polymer may be blended with a matrix polymer like poly(ethylene terephthalate), PET, or polystyrene, PS. However, owing to the immiscibility of these polymers, one can expect the oxygen-

scavenging polymers to form particles (spherical in the simplest case) in the PET or PS matrix. In principle the particle size can be controlled by rheology and compounding conditions.

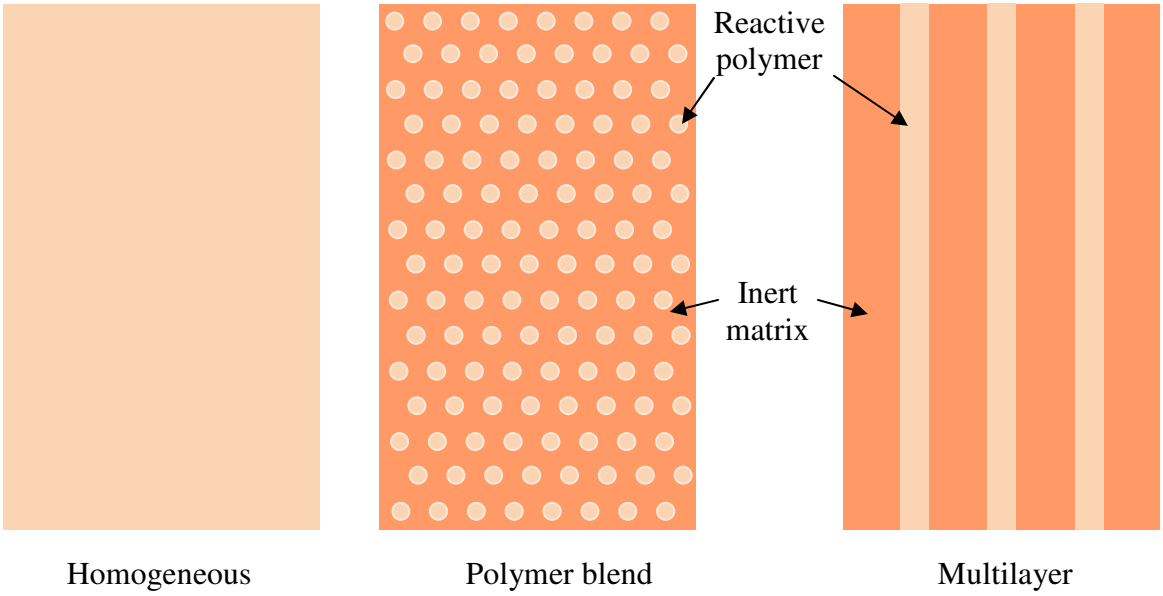

Figure 1.1: Schematic illustration of the three types of reactive barrier films studied.

Alternatively, the scavenging polymer may be co-extruded with PET or PS to form a layered structure, perhaps with many layers (Mueller et al. 1997) as illustrated in figure 1.1. In addition combinations of blends and co-extrusion may be used. The question becomes what is the optimal structure to achieve the best barrier performance while meeting the requirements of mechanical and optical properties. Clearly, there are many variables to consider with a very large experimental matrix to explore. A more efficient approach is to pursue an appropriate modeling strategy in combination with a more targeted experimental program. In the end if the time to reach steady-state

permeation is extended to ranges required by some applications, a totally experimental approach would be unworkable because individual experiments may take years to complete.

There has already been a considerable effort devoted to modeling this type of approach (i.e. immobilization or consumption of mobile species) to improved barrier structures (Finger et al. 1960; Paul 1969; Paul and Kemp 1973; Yang et al. 2001; Yang and Nuxoll 2001; Lape et al. 2002; Siegel and Cussler 2004, 2005; Nuxoll and Cussler 2005; Solovyov and Goldman 2005 a, b, c, 2006 a, b, c, 2008). Traditionally, time lag has been used as the figure of merit for barriers with adsorptive or reactive additives. The time lag is the time it takes for a steady-state concentration profile to be established across a membrane (Frisch 1957; Paul 1969; Paul and Kemp 1973; Paul and Koros 1976). For reactive membranes, time lag is also a measure of how long it takes before all the sites are consumed (Yang et al. 2001; Yang and Cussler 2001; Solovyov and Goldman 2005 c), and it determines the end of life of the barrier. As it turns out, there are relatively simple and accurate schemes to predict the extent scavenging increases the time lag for homogeneous films (Siegel and Cussler 2004) and polymer blends (Ferrari et al. 2009, see Chapter 4). Nuxoll et al. 2005 developed time lag prediction for a layered membrane where a single reactive layer could be placed at different locations within an inert matrix. However, time lag does not predict how much solute (e.g., oxygen or water) will permeate for times before the time lag. While time lag is an important figure of merit, the need to understand the flux prior to time lag has been recognized and some recent work has focused on studying the transient behavior of reactive membranes (Ferrari et al. 2009; Nuxoll and Cussler 2005; Solovyov and Goldman 2005 a, b, c).

Analytical estimates for transient behavior for homogeneous reactive films are currently limited to correlations and narrow ranges of applicability (Yang et al. 2001; Solovyov and Goldman 2005 b). Yang et al. (2001) describe a model valid for very fast reactions, using a pseudo-steady-state solution, but the main focus of the study was to estimate time lag rather than describe the transient. Nuxoll and Cussler (2005) proposed two parameters, namely kill time and leakage parameter, to quantify the transient behavior. However, these parameters are obtained by correlation of many numerical solutions and have a limited range of applicability. Solovyov and Goldman (2005 b) proposed a model that treats a homogeneous reactive membrane as a two-layer system with a moving interface. While an analytical solution was developed, its implicit form precludes its use to predict the transient behavior analytically.

This dissertation develops models and design equations to predict the barrier performance of homogeneous reactive membranes and composite reactive barriers consisting of polymer blends or multilayer films. The partial differential equations for each model were solved numerically, and the influence of design parameters on barrier performance is discussed. The models and design formulae presented here are key components for understanding these materials and confidently extrapolating limited experimental data for product design purposes. While the models and results presented here are applicable to any membrane or film with a mobile solute and immobilized reactive sites, the description throughout all chapters will consider oxygen as the mobile species and oxidation as the reaction.

1.3 DISSERTATION OUTLINE

The outline for the remainder of the dissertation is as follows. In Chapter 2 homogeneous reactive films are studied where the reactive sites are immobilized and the rate of oxygen consumption is a function of the concentration of oxygen and reactive sites. When the partial differential equations were solved numerically, three distinct regimes were identified. For early times most reactive sites remain available, except for a very thin region next to the upstream boundary, and a flux plateau is observed. For intermediate times a moving front is observed. Finally, for long times when most reactive sites have been consumed, the flux approaches its steady-state value, and the time lag is calculated. Analytical predictions for the downstream flux and the characteristic time for each regime are developed and compared to the numerical solutions.

In Chapter 3 a multiscale model is proposed for a polymer blend of spherical particles, using a shrinking core approximation to describe the rate of oxygen consumption in the scavenging polymer particles. Average properties for the blend are used to develop the transport equations for the film. The model equations are solved numerically over a wide parameter space to explore the effects of each parameter on barrier performance. The three regimes observed for homogeneous films are also present in polymer blends.

In Chapter 4 the models for the polymer blend are extended to non-spherical particles. This chapter also expands the methodology described in Chapter 2 to develop design equations for the polymer blend for each of the regimes. Results are compared to

numerical solutions, and the limits of validity of the analytical design equation are discussed.

In Chapter 5 a model is developed for a multilayer system consisting of alternating reactive and inert layers. The methods developed in Chapter 2 are adapted to develop predictive equations for initial flux plateau and time lag. The effect of total number of layers and the specific layer sequence on barrier properties is investigated. Comparison of the numerical solutions to the analytical predictions is presented.

In Chapter 6 the models discussed in Chapters 2-5 are summarized and compared, particularly the barrier performance of polymer blends and multilayer films.

In Chapter 7 an approach is developed to extract physical parameters from oxygen uptake experiments. The model incorporates a variable diffusion coefficient, to reflect reported experimental observations that the diffusion coefficient changes as the film becomes oxidized (Li 2010). The model was applied to experimental data provided by Kevin Tung (Tung 2010) for a polybutadiene containing copolymer with varying levels of metal catalyst.

Finally, in Chapter 8 conclusions and recommendations for future work are presented.

Chapter 2: Homogeneous Reactive Barrier Membranes[1]

2.1 INTRODUCTION

As discussed in Chapter 1, in this dissertation reactive films are studied where the mobile species reacts irreversibly with the immobilized reactive sites, and the rate of consumption depends on the local concentration of mobile and immobilized species. Furthermore, the problem of interest focuses on packaging applications, where one boundary is exposed to a high concentration of the mobile species and the other boundary is exposed to a vanishingly small concentration. In this chapter the focus is on homogeneous reactive membranes, where the reactive sites are uniformly distributed in the bulk polymer. Analytical estimates for transient behavior for homogeneous reactive films are currently limited to correlations and narrow ranges of applicability (Yang et al. 2001; Solovyov and Goldman 2005b). Yang et al. (2001) described a model valid for very fast reactions, using a pseudo-steady-state solution, but the main focus of the study was to estimate time lag rather than describe the transient. Nuxoll and Cussler (2005) proposed two parameters, namely kill time and leakage parameter, to quantify the transient behavior. However, these parameters are obtained by correlation of many numerical solutions and have a limited range of applicability. Solovyov and Goldman (2005b) proposed a model that treats the reactive membrane as a two-layer system with a

[1]Much of this chapter has appeared in Carranza, S., Paul D.R., Bonnecaze, R.T., 2010. Design formulae for reactive barrier membranes. Chemical Engineering Science 65 (3), 1151-1158.

moving interface. While an analytical solution was developed, its implicit form precludes its usefulness to predict the transient behavior.

A model and a complete set of design equations for homogeneous reactive barrier materials are presented in this chapter. When the partial differential equations were solved numerically, three distinct regimes were identified. For early times, most reactive sites remain available, except for a very thin region next to the upstream boundary, and a flux plateau is observed. For intermediate times a moving front is observed. Finally, for long times when most reactive sites have been consumed, the flux approaches its steady-state value, and the time lag is calculated. Predictions of the flux of mobile species, the cumulative permeate, the time lag and kill time have been developed and compared to numerical solutions. While the model and results presented here are applicable to any membrane or film with a mobile solute and immobilized reactive sites, the description throughout the chapter will consider oxygen as the mobile species and oxidation as the reaction. The approach developed in this chapter will be expanded for the analysis of polymer blends in Chapters 3 and 4, and multilayer films in Chapter 5.

2.2 MODEL DESCRIPTION

Consider a one dimensional model of a reactive membrane of thickness L illustrated in figure 2.1. Uniformly distributed, immobile reactive sites are consumed as the reaction progresses. Oxygen transport through the membrane is assumed to obey Fick's law with constant diffusion coefficient D. The transient material balances for oxygen and reactive sites are given by

$$\frac{\partial C}{\partial t} = D\frac{\partial^2 C}{\partial x^2} - k_R\, C\, n\,, \tag{2.1}$$

$$\frac{\partial n}{\partial t} = -\hat{v}\, k_R\, C\, n\,, \tag{2.2}$$

where C is the concentration of oxygen in the film, n is the number density of reactive sites, k_R is the oxidation reaction rate coefficient, $\hat{v}$ is the stoichiometric coefficient for oxidation, x is the position along the membrane thickness and t is time.

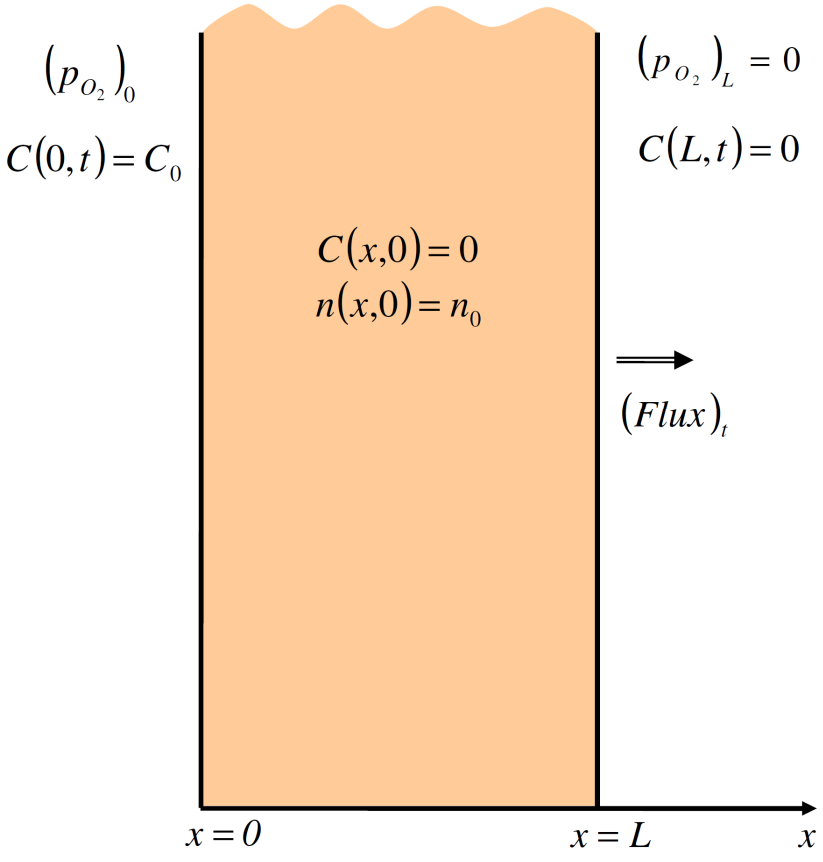

Figure 2.1: Schematic illustration of the reactive membrane film of thickness L.

The film is initially devoid of any oxygen and reactive sites are uniformly distributed throughout the film with number density n_0. For packaging applications the upstream side is exposed to an infinite source of oxygen at partial pressure $\left(p_{O_2}\right)_0$ at time $t = 0$. This source is typically air, and the downstream side has vanishing oxygen partial pressure $\left(p_{O_2}\right)_\ell \sim 0$. The oxygen concentration at the gas/polymer interface is assumed to obey Henry's law. Therefore, the oxygen concentration at the downstream boundary is 0, and the concentration at the upstream boundary, C_0, is given by $C_0 = S_{O_2}\left(p_{O_2}\right)_0$, where S_{O_2} is the solubility of oxygen in the membrane. These initial and boundary conditions can be summarized as

$$\text{I.C.:}\quad C(x,0) = 0, \quad n(x,0) = n_0, \tag{2.3}$$

$$\text{B.C.:}\quad C(0,t) = C_0, \quad C(L,t) = 0. \tag{2.4}$$

The reactive membrane equations can be non-dimensionalized to yield a more convenient form for numerical solution and analysis. Here concentrations, length and time are non-dimensionalized so that

$$\tilde{C} = \frac{C}{C_0}, \quad \tilde{n} = \frac{n}{n_0}, \quad \tilde{x} = \frac{x}{\sqrt{D/k_R\, n_0}}, \quad \tilde{t} = \frac{t}{1/k_R\, n_0}, \tag{2.5}$$

where $\left(D/k_R\, n_0\right)^{1/2}$ and $\left(k_R\, n_0\right)^{-1}$ are the reactive length and time scales, respectively. The dimensionless reactive membrane equations and initial and boundary conditions become

$$\frac{\partial \tilde{C}}{\partial \tilde{t}} = \frac{\partial^2 \tilde{C}}{\partial \tilde{x}^2} - \tilde{C}\,\tilde{n}\,, \tag{2.6}$$

$$\frac{\partial \tilde{n}}{\partial \tilde{t}} = -\nu\, \tilde{C}\, \tilde{n}\ , \tag{2.7}$$

$$\text{I.C.: } \tilde{C}(\tilde{x},0) = 0, \quad \tilde{n}(\tilde{x},0) = 1\,, \tag{2.8}$$

$$\text{B.C.: } \tilde{C}(0,\tilde{t}\,) = 1, \quad \tilde{C}(\tilde{L},\tilde{t}\,) = 0\,, \tag{2.9}$$

where $\nu = \hat{\nu}\, C_0 / n_0$ is the stoichiometric coefficient normalized by upstream oxygen concentration and the initial number density of reactive sites, and the dimensionless film thickness $\tilde{L}$ is the Thiele modulus, i.e., the ratio between the diffusion length scale and reactive length scale, given by $\tilde{L} = L/l_c = \Phi_H = \left(k_R\, n_0 L^2 / D\right)^{1/2}$. Note that the Damköhler number Da is the ratio between the time scales for diffusion and reaction,

$$Da = k_R\, n_0 L^2 / D = {\Phi_H}^2\,. \tag{2.10}$$

The oxygen flux and the total amount of oxygen permeated are quantities of interest derived from the solution of equations 2.6 to 2.9. The downstream flux J at time t is given by

$$J\big|_{x=L} = -D \left.\frac{\partial C}{\partial x}\right|_{x=L}\,, \tag{2.11}$$

and the total oxygen permeated through the membrane Q_t at time t is given by

$$Q_t = \int_0^t J\big|_{x=L}\, dt\,. \tag{2.12}$$

In dimensionless terms, the downstream flux $\tilde{J}$ at time $\tilde{t}$ is given by

$$\tilde{J}\big|_{\tilde{x}=\tilde{L}} = \frac{J\big|_{x=L}}{J_{SS}} = -\tilde{L} \left.\frac{\partial \tilde{C}}{\partial \tilde{x}}\right|_{\tilde{x}=\tilde{L}} = -\Phi_H \left.\frac{\partial \tilde{C}}{\partial \tilde{x}}\right|_{\tilde{x}=\Phi_H}\,, \tag{2.13}$$

where $J_{SS} = C_0 D/L$ is the steady-state oxygen flux. The dimensionless total oxygen permeated through the membrane $\tilde{Q}_{\tilde{t}}$ at time $\tilde{t}$ is given by

$$\tilde{Q}_{\tilde{t}} = \frac{Q_t}{J_{SS}\left(k_R n_0\right)^{-1}} = \int_0^{\tilde{t}} \tilde{J}\Big|_{\tilde{x}=\tilde{L}} d\tilde{t} \ . \tag{2.14}$$

These dimensionless equations may be solved numerically using a finite-difference method. Here the equations were solved using an explicit method using two-point forward difference for time derivatives and three-point central difference for spatial derivative. Time and space increments were adjusted iteratively to ensure numerical convergence. Numerical solutions were calculated for $0.0025 < \nu < 1$ and $2 < \Phi_H < 80$. The range of dimensionless parameters ν and Φ_H were selected based on expected oxidation rates of polybutadiene embedded in polystyrene or poly(ethylene terephthalate) matrices (Ferrari et al. 2009), along with more extreme values of ν (0.1 and 1) to represent limits of very low reactive capacity. In the next section we will show some typical numerical results. These will then motivate the development of an asymptotic analysis of the reactive membrane equations.

2.3 ANALYSIS

Typical evolutions over time of the spatial profiles for the oxygen concentration and the number of reactive sites based on numerical solution of equations 2.6 -2.9 for $\nu = 0.0025$ and $\tilde{L} = \Phi_H = 20$ are shown in figures 2.2 and 2.3. The concentration profiles in figure 2.2 have three distinct zones, as schematically illustrated in figure 2.4. In the first zone the oxygen concentration varies linearly and its transport is

predominantly diffusive. The scavenging sites have all been consumed in this zone. In the second zone there is a faster non-linear decay of oxygen concentration dominated by reaction, with a concomitant change in scavenger concentration. In the third zone there is a vanishing oxygen concentration, which is consistent with the downstream boundary condition. Over time as the reactive sites are consumed, the diffusion zone grows until all sites are consumed and the oxygen concentration profile becomes linear for the whole membrane.

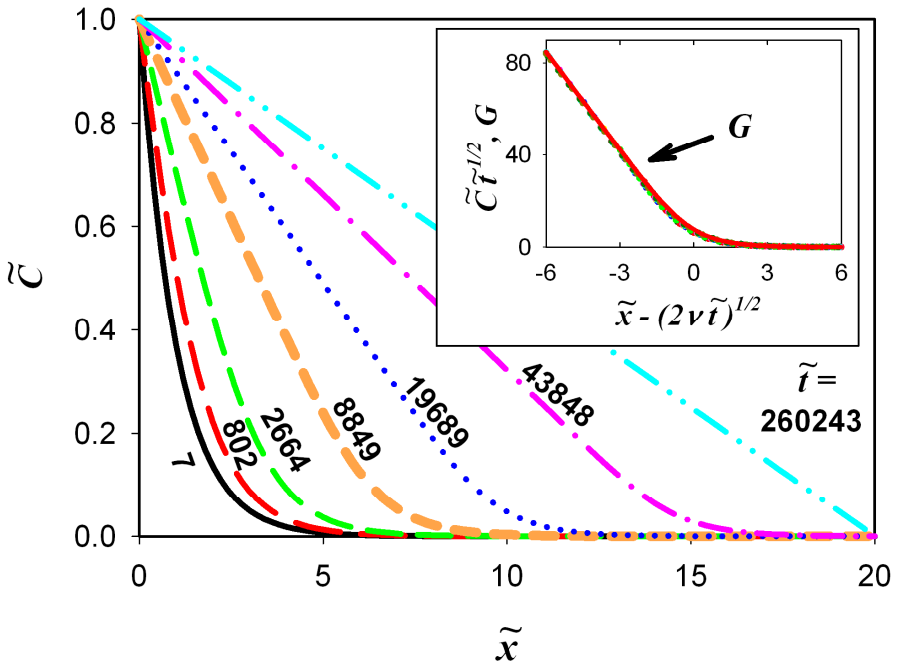

Figure 2.2: Oxygen concentration $\tilde{C} = C/C_0$ versus position in reactive membrane film $\tilde{x} = x\left(D/k_R\, n_0\right)^{-1/2}$ at various times $\tilde{t} = t\, k_R\, n_0$ for $\nu = 0.0025$ and $\tilde{L} = \Phi_H = 20$. Insert shows normalized concentration versus moving front coordinate. Insert legend: solid line - G ; dotted lines - $\tilde{C}\tilde{t}^{1/2}$.

These three zones identified in the oxygen concentration profiles can be mapped to the reactive sites profiles shown in figure 3, where $\tilde{n} \to 0$ corresponds to the diffusion zone, $0 < \tilde{n} < 1$ corresponds to the reaction zone, and $\tilde{n} \to 1$ corresponds to the vanishing oxygen concentration. As reactive sites are consumed, the reaction zone moves across the membrane, until it reaches the downstream boundary. These three zones will be described in more detail in the moving reaction front analysis, which will lead to the normalized insets shown in figures 2.2 and 2.3. Discussion on alternate approaches for describing this moving reaction front is presented at the Supplemental Material section at the end of this chapter.

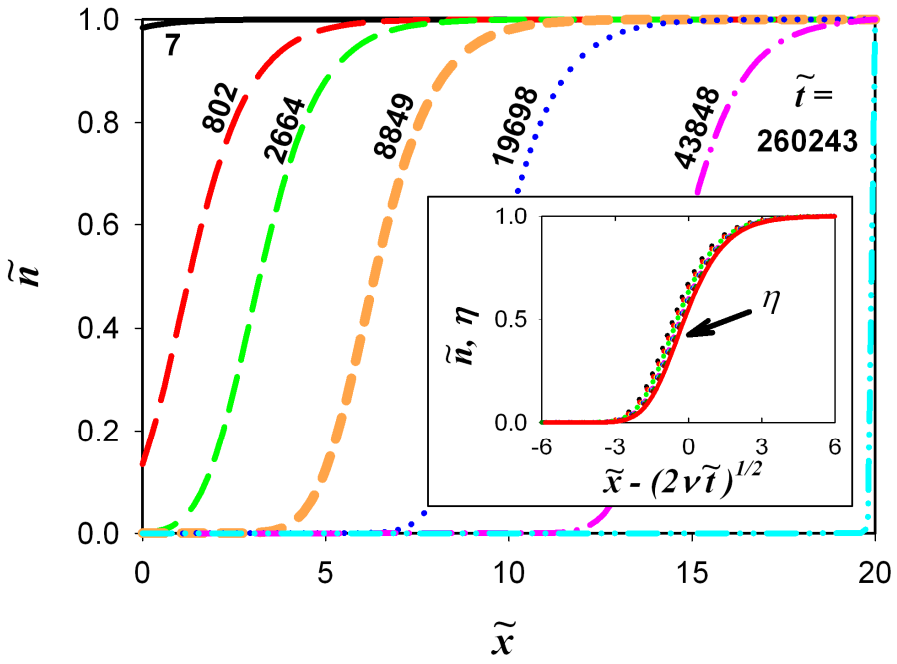

Figure 2.3: Number of reactive sites $\tilde{n} = n/n_0$ versus position in reactive membrane film $\tilde{x} = x\left(D/k_R\, n_0\right)^{-1/2}$ at various times $\tilde{t} = t\, k_R\, n_0$ for $\nu = 0.0025$ and $\tilde{L} = \Phi_H = 20$. Insert shows number of reactive sites versus moving front coordinate. Insert legend: solid line - η; dotted lines - $\tilde{n}$.

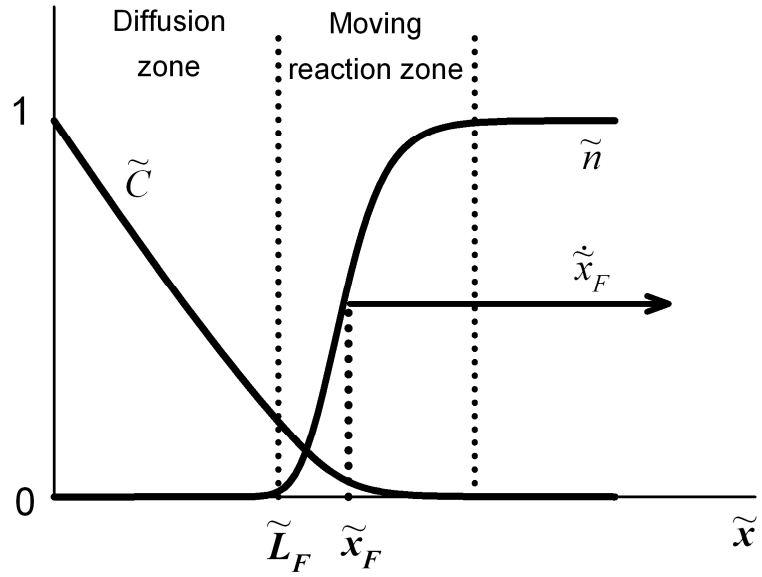

Figure 2.4: Schematic illustration of moving reaction zone

The downstream oxygen flux defined by equation 2.13 is plotted versus time in figure 2.5 for various values of ν and Φ_H. Inspection of the numerical solutions reveals three regimes of interest for the downstream flux, as illustrated in figure 2.6. The early time regime is characterized by a fast rise of the flux, followed by a flux plateau. This early plateau eventually gives way to a regime of rising oxygen flux. The third regime occurs when all the reactive sites have been consumed, and the flux reaches its final steady-state value. The following sections will discuss approaches to analyze the equations in each of these regimes, and the results obtained, which are summarized in table 2.1 in terms of the physical parameters of the reactive membrane, along with the approximate interval of validity for each regime.

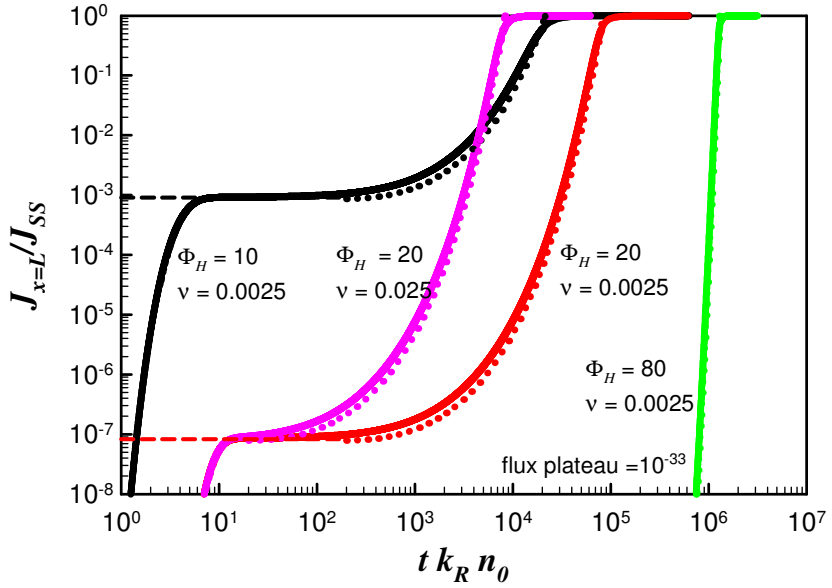

Figure 2.5: Dimensionless downstream oxygen flux versus dimensionless time $\tilde{t} = t\,k_R n_0$ for varying ν and Φ_H. Solid lines represent the numerical solution for each case. Dotted lines represent the moving front estimate for intermediate times. The dashed lines represent the initial flux plateau prediction.

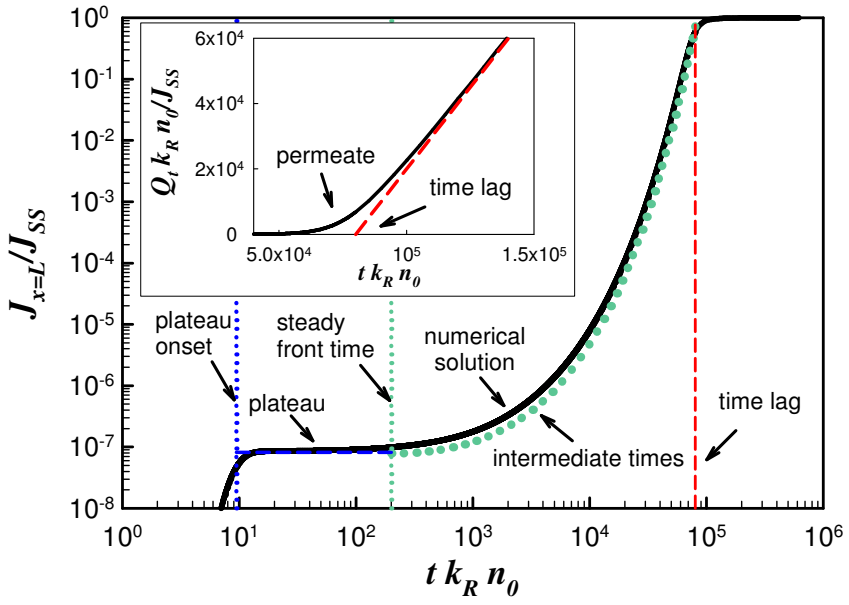

Figure 2.6: Comparison of numerical solution and analytical estimates for the three regimes relevant to analysis of dimensionless downstream oxygen flux, using $\nu = 0.0025$ and $\tilde{L} = \Phi_H = 20$. Insert shows the time lag as determined from the numerical solution, using the asymptote as $\tilde{Q}_{\tilde{t}\to\infty}$.

Table 2.1: Design equations for early, intermediate and long times

Time interval	**Dimensionless equations**	**Dimensional equations**
Early times	$\tilde{J}\big\|_{\tilde{x}=\tilde{L}} \sim 2\tilde{L}\,e^{-\tilde{L}} \quad for\ \tilde{L} >> 1$	$J\big\|_{x=L} = 2J_{SS}\Phi_H\, e^{-\Phi_H}$
$0 \le \tilde{t} \le \tilde{t}_{SF}$	$\tilde{t}_{SF} = \tilde{t}_{\min} = 1/2\nu$	$t_{SF} = t_{\min} = (2\nu\, k_R\, n_0)^{-1}$
Intermediate times	$\tilde{J}\big\|_{\tilde{x}=\tilde{L}} = 0.653\dfrac{\tilde{L}}{e^{\tilde{L}}}\dfrac{e^{\sqrt{2\nu\tilde{t}}}}{\sqrt{2\nu\,\tilde{t}}}$	$J\big\|_{x=L} = 0.653\,J_{SS}\dfrac{L/x_F}{e^{\Phi_H(1-x_F/L)}}$
$\tilde{t}_{SF} \le \tilde{t} \le \tilde{t}_L$	$\tilde{x}_F(\tilde{t}) = \sqrt{2\nu\,\tilde{t}}$	$x_F = \sqrt{2\nu\,Dt}$
Long times	$\tilde{J}\big\|_{\tilde{x}=\tilde{L}} \to 1$	$J\big\|_{x=L} \to J_{SS} = C_0 D/L$
$\tilde{t} > \tilde{t}_L$	$\tilde{t}_L = \tilde{L}^2\left(\dfrac{1}{6}+\dfrac{1}{2\nu}\right)$	$t_L = \dfrac{L^2}{D}\left(\dfrac{1}{6}+\dfrac{1}{2\nu}\right)$

$\nu \equiv \hat{\nu}\, C_0/n_0$, $\tilde{L} \equiv \Phi_H \equiv \sqrt{k_R n_0 L^2/D}$, where all physical (dimensional) parameters are defined with equations 2.1 to 2.4.

2.3.1 Analysis of early times to estimate initial leakage flux plateau

At early times, most of the scavenger sites remain unreacted, except those very close to the upstream boundary, as illustrated in figure 2.3. Therefore, it is reasonable to consider $\tilde{n} \cong 1$ at early times. Also, the oxygen flux in the plateau region of interest is quasi-steady state, thus, the oxygen transport equation and boundary conditions become

$$\frac{\partial^2 \tilde{C}}{\partial \tilde{x}^2} - \tilde{C} = 0, \tag{2.15}$$

$$\text{B.C.:}\quad \tilde{C}(\tilde{x}=0) = 1, \quad \tilde{C}\left(\tilde{x} = \tilde{L} = \Phi_H\right) = 0. \tag{2.16}$$

The analytic solution to this equation and boundary conditions is given by

$$\tilde{C} = -\frac{\cosh(\Phi_H)}{\sinh(\Phi_H)}\sinh(\tilde{x}) + \cosh(\tilde{x})\,. \tag{2.17}$$

Using equation 2.13 for the downstream flux with equation 2.17 for oxygen concentration gives the algebraic expression for the flux plateau

$$\tilde{J}\Big|_{\tilde{x}=\tilde{L}=\Phi_H} = \Phi_H \big/ \sinh\left(\Phi_H\right) \text{ or } \tilde{J}\Big|_{\tilde{x}=\tilde{L}=\Phi_H} \sim 2\Phi_H\, e^{-\Phi_H} \quad for\ \Phi_H \gg 1\,. \tag{2.18}$$

Note that this regime is described by a first order reaction-diffusion model. Solovyov and Goldman (2005b) derived a similar equation for the flux to describe a system with a large excess of reactive sites, as part of their modified moving front model. Here this model is used to describe the flux in the early times regime.

The onset of the initial plateau $\tilde{t}_{onset}$ can be estimated by solving the transient first order reaction-diffusion model. The onset $\tilde{t}_{onset}$ can be interpreted as the time lag for an equivalent first order reactive membrane, which has been calculated by Siegel (1991). In terms of the dimensionless variables utilized here, the estimate of the flux plateau onset time $\tilde{t}_{onset}$ is given by

$$\tilde{t}_{onset} = \frac{\Phi_H \coth\left(\Phi_H\right) - 1}{2}, \text{ or } \tilde{t}_{onset} \sim \frac{\Phi_H - 1}{2} \quad for\ \Phi_H >> 1\,. \tag{2.19}$$

Note that the second approximate expression for the onset time retains the constant 1 in the numerator because it is found to be a good approximation for Φ_H as low as 2 or 3.

2.3.2 Analysis of intermediate times as a moving reaction front

Observation of the time evolution of the spatial profiles for oxygen concentration shown in figure 2.2 and for the reactive sites shown in figure 2.3 indicate that the reactive

membrane can be characterized by a moving front for intermediate times starting when a full front has been established ($\tilde{t}$ ~ 2600) and ending when the moving front reaches the downstream boundary ($\tilde{t}$ ~ 44000). Figure 2.4 provides a schematic illustration of the diffusion zone and the moving reaction zone in the reactive membrane in such interval. $\tilde{L}_F$ is the position of the interface between the diffusion zone and the reaction zone, $\tilde{x}_F$ is the position of the moving front and $\dot{\tilde{x}}_F$ is the moving front speed. As reactive sites are consumed, the reaction zone moves through the thickness of the film, and the diffusion zone (upstream of the reaction zone) grows. Thus, $\tilde{L}_F$, $\tilde{x}_F$ and $\dot{\tilde{x}}_F$ are functions of time. This analysis will seek solutions in the frame of reference of the moving reaction zone, with solutions of the form

$$\tilde{n}(\tilde{x},\tilde{t}) = \eta(\xi), \tag{2.20}$$

$$\tilde{C}(\tilde{x},\tilde{t}) = \tilde{t}^{\,\alpha}\, G(\xi), \tag{2.21}$$

$$\xi = \tilde{x} - \tilde{x}_F(\tilde{t}), \tag{2.22}$$

where $\eta(\xi)$ represents the reactive site in the new frame of reference, α is a constant, and $G(\xi)$ is the self-similar oxygen concentration field. The form of the concentration solution per equation 2.21 was selected to satisfy the quasi-steady flux condition upstream of the reaction zone. The reactive membrane equations thus become

$$\alpha\,\tilde{t}^{\,-1} G + \frac{\partial G}{\partial \tilde{t}} - \dot{\tilde{x}}_F \frac{\partial G}{\partial \xi} = \frac{\partial^2 G}{\partial \xi^2} - G\eta\,, \tag{2.23}$$

$$\frac{\partial \eta}{\partial \tilde{t}} - \dot{\tilde{x}}_F \frac{\partial \eta}{\partial \xi} = -\nu\,\tilde{t}^{\,\alpha} G\eta\,. \tag{2.24}$$

At long times in the frame of reference of the moving front the solutions approach steady state, i.e., $\frac{\partial G}{\partial \tilde{t}} = \frac{\partial \eta}{\partial \tilde{t}} = 0$. Furthermore, equation 2.24 can be made into an ODE if $\dot{\tilde{x}}_F = B\tilde{t}^{\,\alpha}$. Thus, for large enough times, assuming $\alpha < 0$, and looking only at leading order terms, equations 2.23 and 2.24 and their boundary conditions become

$$\frac{d^2 G}{d\xi^2} - G\eta = 0, \tag{2.25}$$

$$\frac{d\eta}{d\xi} = \frac{\nu}{B} G\eta, \tag{2.26}$$

$$\text{B.C.:}\quad \eta(\infty) = 1, \quad G(\infty) = 0, \quad \left.\frac{dG}{d\xi}\right|_{-\infty} = const\ . \tag{2.27}$$

The flux of reactant into the moving reaction zone (see figure 2.4) is provided by the diffusion zone. The flux from the diffusion zone must scale with the flux into reactive zone, so that

$$\underbrace{\frac{1}{\tilde{x}_F} = \frac{\alpha+1}{B\tilde{t}^{\,\alpha+1}}}_{diff\ flux} \sim \underbrace{\tilde{t}^{\,\alpha}\frac{dG}{d\xi}}_{rxn\ flux}. \tag{2.28}$$

Equating time dependence in both terms requires that $\alpha = -1/2$, which is consistent with the assumption of $\alpha < 0$ made earlier, and makes the error of approximation $O\left(\tilde{t}^{\,-1/2}\right)$. This result is consistent with the fact that the change in the front position is limited by diffusion and therefore $\tilde{x}_F$ scales with $\tilde{t}^{\,1/2}$.

To determine B in equation 2.26, consider the interface between the diffusion zone and the reaction zone, identified by $\tilde{L}_F$ in figure 2.4. The concentration field is

assumed linear in the diffusion zone, with concentration approaching 0 at the interface. The interface position may be expressed as $\tilde{L}_F = \tilde{x}_F - \Delta$, where Δ is an offset from the front position $\tilde{x}_F$. To leading order $\tilde{L}_F \approx \tilde{x}_F = 2B\tilde{t}^{1/2}$, since the offset Δ is likely small in comparison to the front position $\tilde{x}_F$, except for positions very close to the upstream boundary. The oxygen flux at either side of the interface is thus given by

$$\underbrace{\frac{1}{2B\tilde{t}^{1/2}}}_{diff\ \ flux} = \underbrace{-\tilde{t}^{-1/2}\left.\frac{dG}{d\xi}\right|_{-\infty}}_{rxn\ flux} \Rightarrow -\left.\frac{dG}{d\xi}\right|_{-\infty} = \frac{1}{2B}. \tag{2.29}$$

The constant B is still unknown. Conservation of oxygen consumed in the reaction zone yields

$$\underbrace{-\tilde{t}^{-1/2}\left.\frac{dG}{d\xi}\right|_{-\infty}}_{flux} = \underbrace{\tilde{t}^{-1/2}\int_{-\infty}^{\infty} G\eta d\xi}_{rate-of-cons}. \tag{2.30}$$

Combining equation 2.30 with equation 2.26 and the boundary conditions of equation 2.27 gives an alternate form of the flux condition, and the value of B

$$-\left.\frac{dG}{d\xi}\right|_{-\infty} = \frac{B}{\nu} \quad \Rightarrow \quad B = \sqrt{\nu/2}\,. \tag{2.31}$$

Thus, the front position becomes

$$\tilde{x}_F = \sqrt{2\nu\,\tilde{t}}\,. \tag{2.32}$$

Introducing $\hat{G} = \sqrt{2\nu}\,G$, the equations and boundary conditions for the concentration fields in the reaction zone are made universal and given by

$$\frac{d^2\hat{G}}{d\xi^2} - \hat{G}\eta = 0, \tag{2.33}$$

$$\frac{d\eta}{d\xi} - \hat{G}\eta = 0, \tag{2.34}$$

$$\text{B.C.:}\quad \eta(\infty) = 1, \quad \hat{G}(\infty) = 0, \quad \left.\frac{d\hat{G}}{d\xi}\right|_{-\infty} = -1, \tag{2.35}$$

where $\xi = \tilde{x} - \sqrt{2\nu\,\tilde{t}}$.

These equations have asymptotic solutions as $\xi \to \infty$, the location of the downstream boundary, of the form,

$$\hat{G} = be^{-\xi}, \quad \eta = 1 - be^{-\xi}. \tag{2.36}$$

Using equation 2.13 for flux and substituting equation 2.36 in equation 2.21 for concentration gives the algebraic expression for the downstream flux

$$\tilde{J}\Big|_{\tilde{x}=\tilde{L}=\Phi_H} = b\frac{\Phi_H}{e^{\Phi_H}}\frac{e^{\sqrt{2\nu\tilde{t}}}}{\sqrt{2\nu\,\tilde{t}}}. \tag{2.37}$$

The value of b can be estimated in two ways. First, this expression has a minimum when $\tilde{t}_{\min} = 1/2\nu$, with the flux values diverging from the numerical solution for times $\tilde{t} < 1/2\nu$. The flux estimate should be valid from the time $\tilde{t}_{SF}$ a steady front has been established to the time before the front has reached the right boundary, see figure 2.3. This time can be estimated by comparing the consumption of reactive sites within the front volume with the influx of oxygen into the front volume,

$$A\sqrt{D/k_R n_0}\,(0.5\,n_0/\hat{v}) \sim A\,t_{SF}\,DC_0/\sqrt{D/k_R n_0}, \tag{2.38}$$

where A is the membrane area, $\sqrt{D/k_R n_0}$ is the reactive length scale and $\hat{\nu}$ is the stoichiometric coefficient for the oxidation reaction; therefore

$$t_{SF} = 1/2\,\nu\,k_R n_0 \text{, or } \tilde{t}_{SF} = 1/2\,\nu\,. \tag{2.39}$$

Note that $\tilde{t}_{SF} = \tilde{t}_{\min}$, confirming the time range of interest. The flux plateau described in the previous section characterizes the time period prior to this transition; therefore one approach to obtain a reasonable solution is to equate the flux at $\tilde{t}_{\min} = 1/2\nu$ to the flux plateau, hence defining the constant b as

$$\underbrace{2\frac{\Phi_H}{e^{\Phi_H}}}_{\text{flux plateau}} = \underbrace{b\frac{\Phi_H}{e^{\Phi_H}}\frac{e^{\sqrt{2\nu\tilde{t}_{\min}}}}{\sqrt{2\nu\,\tilde{t}_{\min}}}}_{\text{flux}@\,\tilde{t}_{\min}} \quad \Rightarrow \quad b = \frac{2}{e} \sim 0.736\,. \tag{2.40}$$

Another approach is to match the asymptotic solutions of the diffusion zone and the moving reaction zone. In the diffusion zone, concentration is linear with slope $-1/\tilde{x}_F$. Thus, the concentration in the diffusion zone is given by

$$\tilde{C}(\tilde{x},\tilde{t}) \sim 1 - \tilde{x}/\tilde{x}_F = -\xi/\sqrt{2\nu\,\tilde{t}}\,. \tag{2.41}$$

In the moving reaction zone, according to equation 2.21, concentration is given by

$$\tilde{C}(\tilde{x},\tilde{t}) \sim \hat{G}(\xi)/\sqrt{2\nu\,\tilde{t}}\,. \tag{2.42}$$

Thus, matching of the two asymptotic solutions requires that

$$\hat{G}(\xi) = -\xi \text{ as } \xi \to -\infty\,. \tag{2.43}$$

Figure 2.7 shows the numerical solution of the universal equations 2.33 and 2.34. The equations were solved by the shooting method using equation 2.36 as the initial conditions, varying b until a solution satisfying equation 2.43 was found. The dashed

line in figure 2.7 shows the asymptotic solution $\hat{G}(\xi) = -\xi$, which matches the full numerical solution when $b = 0.653$, close to the estimate in equation 2.40. Thus, for the moving front regime, the dimensionless downstream flux becomes

$$\tilde{J}\Big|_{\tilde{x}=\tilde{L}=\Phi_H} = 0.653 \frac{\Phi_H}{e^{\Phi_H}} \frac{e^{\sqrt{2\nu\tilde{t}}}}{\sqrt{2\nu\,\tilde{t}}}. \tag{2.44}$$

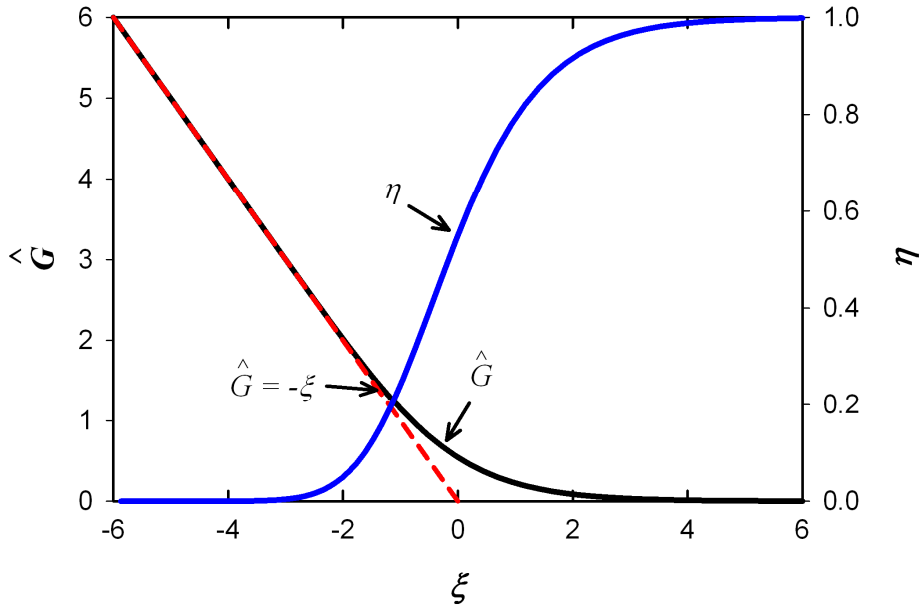

Figure 2.7: Moving front universal solution

2.3.3 Steady-state analysis to estimate time lag

The use of asymptotic steady-state analysis to estimate diffusion time lag was developed by Frisch (1957). Siegel and Cussler (2004) adapted Frisch's method to estimate time lag for homogeneous reactive membranes, using a model that is similar to the one used in this chapter. The derivation was modified to work with the dimensionless equations and boundary conditions described in this chapter. Solovyov and Goldman

(2005c) looked at non-zero initial oxygen concentration and other variations of the reactive membrane model. More recently, the time lag has been derived for reactive polymer blends (Ferrari et al. 2009).

Following Siegel and Cussler (2004), the method to estimate time lag first combines both the mobile species and reactive sites concentration equations to give

$$\frac{\partial \tilde{C}}{\partial \tilde{t}} - \frac{1}{\nu}\frac{\partial \tilde{n}}{\partial \tilde{t}} = \frac{\partial^2 \tilde{C}}{\partial \tilde{x}^2}. \tag{2.45}$$

This equation is integrated from an arbitrary $\tilde{x}$ to $\tilde{L}$, and subsequently integrated from $\tilde{x} = 0$ to $\tilde{L}$, and applying boundary conditions, giving

$$\int_0^{\tilde{L}} \tilde{x}\frac{\partial \tilde{C}}{\partial \tilde{t}}\,d\tilde{x} - \frac{1}{\nu}\int_0^{\tilde{L}} \tilde{x}\frac{\partial \tilde{n}}{\partial \tilde{t}}\,d\tilde{x} = \tilde{L}\left.\frac{\partial \tilde{C}}{\partial \tilde{x}}\right|_{\tilde{L}} + 1. \tag{2.46}$$

Integrating the equation from time 0 to $\tilde{t}$, and evaluating each term for $\tilde{t}$ going to infinity, the concentration profile will be linear and the reactive sites will be consumed (except for the discontinuity at the boundary). Using equation 2.14 for $\tilde{Q}_{\tilde{t}}$ yields the asymptotic equation

$$\tilde{Q}_{\tilde{t}\to\infty} = \tilde{t} - \Phi_H{}^2\left(\frac{1}{6} + \frac{1}{2\nu}\right). \tag{2.47}$$

Recall that $\tilde{L} = \Phi_H$. The time lag is determined by the point where $\tilde{Q}_{\tilde{t}\to\infty}$ intercepts the $\tilde{t}$ axis

$$\tilde{t}_L = \Phi_H{}^2\left(\frac{1}{6} + \frac{1}{2\nu}\right). \tag{2.48}$$

2.3.4 Design parameters based on transient behavior

For oxygen sensitive products, the goal of barrier or packaging materials is to minimize the cumulative oxygen contamination during the entire product life. Nuxoll and Cussler (2005) discussed the need to quantify the transient behavior of reactive membranes. They defined a so-called kill time to predict when a predefined amount of the mobile species (e.g., oxygen) will breakthrough, and proposed an experimental correlation to estimate it. This section describes an analytical approach to calculate the cumulative oxygen permeate $\tilde{Q}_{\tilde{t}}$ and kill time $\tilde{t}_K$.

The cumulative oxygen permeate $\tilde{Q}_{\tilde{t}}$ is obtained by the integration of the downstream flux, per equation 2.14. Analytical estimates of the downstream flux were developed for initial times, (equation 2.18), and intermediate times $\tilde{t}_{SF} \le \tilde{t} \le \tilde{t}_L$, see equation 2.44, where $\tilde{t}_{SF} = 1/2\nu$. Thus, adding the contributions from each regime, the oxygen permeate can be estimated by

$$\tilde{Q}_{\tilde{t}} = \underbrace{\int_0^{\tilde{t}_{SF}} \tilde{J}\Big|_{\tilde{x}=\tilde{L}=\Phi_H} d\tilde{t}}_{\text{early times}} + \underbrace{\int_{\tilde{t}_{SF}}^{\tilde{t}} \tilde{J}\Big|_{\tilde{x}=\tilde{L}=\Phi_H} d\tilde{t}}_{\text{moving front regime}} = \frac{\Phi_H}{\nu\, e^{\Phi_H}} + 0.653\frac{\Phi_H}{\nu\, e^{\Phi_H}}\left(e^{\sqrt{2\nu\tilde{t}}} - e\right). \tag{2.49}$$

For times below $\tilde{t}_{SF} = 1/2\nu$, the above equation reduces to $\tilde{Q}_{\tilde{t}} = 2\Phi_H e^{-\Phi_H}\tilde{t}$, which is simply the flux at the early plateau multiplied by time. Note that the flux is zero before the flux plateau onset $\tilde{t}_{onset}$. Equation 2.49 integrates the flux plateau for all times below $\tilde{t}_{SF}$ for simplicity, because typically $\tilde{t}_{onset} << \tilde{t}_{SF}$, making the contribution prior to $\tilde{t}_{onset}$

negligible. The kill time $\tilde{t}_K$ can be found by solving equation 2.49 for the time when the oxygen permeate reaches a predefined max $\tilde{Q}_{\max}$, giving

$$\tilde{t}_K^{\,1/2} = (2\nu)^{-1/2} \ln\left(e + \frac{\nu\, e^{\Phi_H} \tilde{Q}_{\max} - \Phi_H}{0.653\, \Phi_H} \right). \tag{2.50}$$

Note that if kill time $\tilde{t}_K$ is much smaller than time lag $\tilde{t}_L$, the end of life of the barrier will occur well before the reactive sites have been exhausted, therefore, a significant portion of the reactive capacity will be wasted. If one of the design goals is to maximize the use of the reactive capacity, either to preserve mechanical properties, or for cost effectiveness, then in the ideal system $\tilde{t}_K$ and $\tilde{t}_L$ will be of the same order of magnitude.

2.4 NUMERICAL SOLUTIONS VERSUS ANALYTICAL ESTIMATES

The reactive membrane problem defined by equations 2.6 to 2.9 was solved numerically for a range of ν and $\tilde{L}$ values. Selected results are presented here and compared to the analytical estimates described in previous sections. Figure 2.2 presents the time evolution for the oxygen concentration profiles for $\nu = 0.0025$ and $\tilde{L} = \Phi_H = 20$ in the main chart, while the inset compares the concentration profiles time-normalized by $\tilde{C}\tilde{t}^{\,1/2}$, with G from the moving front equation 2.33 to 2.35, both plotted against the moving front coordinate $\xi = \tilde{x} - (2\nu\,\tilde{t}\,)^{1/2}$. Likewise, figure 2.3 shows the reactive site profiles in the main chart, while the inset shows the comparison between η and $\tilde{n}$ plotted versus $\tilde{x} - (2\nu\,\tilde{t}\,)^{1/2}$. The simpler asymptotic formulae agree very well with the numerical solution.

Figure 2.8 compares the position of the moving front $\tilde{x}_F$ calculated from the numerical solution as the position where $\tilde{n} = 0.5$ with the asymptotic prediction that $\tilde{x}_F(\tilde{t}) = \sqrt{2\nu\,\tilde{t}}$, per equation 2.32 for several values of ν and $\tilde{L} = \Phi_H = 20$. Figure 2.8 curves show very good agreement starting at intermediate times. For the case of $\nu = 0.0025$, the intermediate time range can be mapped to the range of established fronts in figure 2.3.

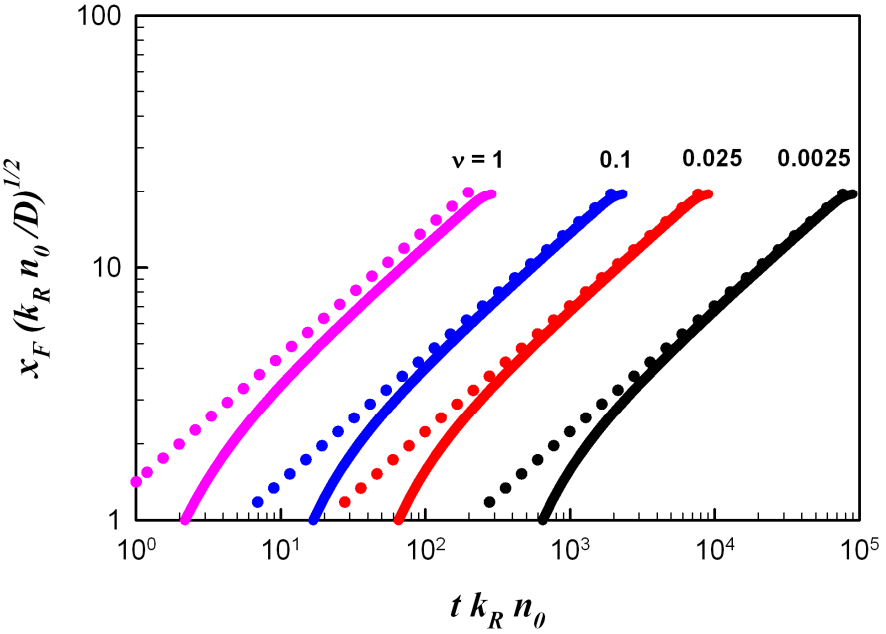

Figure 2.8: Front position versus time for $\tilde{L} = \Phi_H = 20$ and several values of ν. Solid lines represent numerical solution, where $\tilde{x}_F$ is defined as the position corresponding to $\tilde{n} = 0.5$; dotted lines are asymptotic prediction that $\tilde{x}_F(\tilde{t}) = \sqrt{2\nu\,\tilde{t}}$ per Eq. (32), or $x_F = \sqrt{2\nu D t}$ in dimensional terms.

There are two additional transient quantities of interest for designing packaging materials: the downstream oxygen flux and the total oxygen permeate, expressed in dimensionless terms in equations 2.13 and 2.14, respectively. Figure 2.5 illustrates the

effects of varying ν and $\tilde{L}$ on the transient behavior of the downstream flux and compares the numerical solution to the analytical estimates for each regime described in the analysis section. Figure 2.6 shows the validity intervals for $\nu = 0.0025$ and $\tilde{L} = \Phi_H = 20$. For early times, the flux plateau estimated by equation 2.18 matched the numerical solution within a 5% margin for all cases computed ($5 \le \Phi_H \le 80$). For intermediate times ($\tilde{t}_{SF} \le \tilde{t} \le \tilde{t}_L$, see table 2.1), the flux estimated by equation 2.44 provided a reasonable prediction of the numerical solutions, with highest deviation in the lower flux range (~30% underestimation). As shown in figure 2.5 increasing Φ_H leads to a decrease of the initial values of the dimensionless downstream flux, which agrees with the flux plateau prediction per equation 2.18. This behavior can be explained physically, since the ratio between the diffusion and reaction time scales increases with Φ_H per $\Phi_H = Da^{1/2}$, therefore increasing the time available for the mobile oxygen to react. For a constant Φ_H, increasing ν has no effect on the value of the flux plateau. Note that the validity of the moving front estimate for intermediate times can be known a priori, by comparing the onset of the flux plateau $\tilde{t}_{onset}$ with the time $\tilde{t}_{SF}$ a steady front has been established. If $\tilde{t}_{SF} > \tilde{t}_{onset}$ the initial flux plateau and the moving front regimes will be observed, and the analytical predictions will be reasonable approximations of the numerical solutions. However, if $\tilde{t}_{SF} < \tilde{t}_{onset}$, there will not be a clear distinction of regimes and the analytical approximations will not be valid.

The inset in figure 2.6 shows the time lag as determined from the numerical solution using the asymptote as $\tilde{Q}_{\tilde{t}\to\infty}$. The time lag estimated by equation 2.48 and the time lag obtained numerically are in excellent agreement for all cases computed, with the largest relative errors on the order of 10^{-4}. This is not surprising since equation 2.48 was calculated by analytically obtaining the asymptote $\tilde{Q}_{\tilde{t}\to\infty}$. The dimensionless time lag decreases with increasing ν or increase in Φ_H, which is in agreement with the asymptotic prediction of the time lag per equation 2.48. Physically, when ν increases, the polymer capacity relative to the oxygen concentration at the upstream boundary decreases, consequently it is not surprising that the time lag decreases. While there is an apparent effect of Φ_H on the dimensionless time lag, this is an artifact of the time scale chosen for non-dimensionalization. Reverting equation 2.48 to dimensional terms,

$$\frac{t_L}{\underbrace{1/k_R n_0}_{\tilde{t}_L}} = \underbrace{\frac{k_R n_0 L^2}{D}}_{\Phi_H{}^2}\left(\frac{1}{6}+\frac{1}{2\nu}\right) \quad \Rightarrow \quad t_L = \frac{L^2}{D}\left(\frac{1}{6}+\frac{1}{2\nu}\right), \tag{2.50}$$

reveals that Φ_H does not affect time lag, as noted earlier by Siegel and Cussler (2004).

2.5 SUMMARY AND CONCLUSIONS

Design formulae for homogeneous reactive membranes have been developed based on analysis of three time regimes observed in the numerical solution of the model and are summarized in table 2.1. The homogeneous reactive membrane model has two dimensionless parameters, Φ_H and ν. Φ_H is the Thiele modulus, defined by the ratio between the length scale of diffusion and the length scale of reaction, and ν is the ratio

between oxygen content in the film and its scavenging capacity. By comparing the numerical solution and the design formulae, the parameter space of validity for the analytical predictions has been established.

The predictions for the initial flux plateau and for time lag are accurate throughout the range studied. The limits of validity for the intermediate times based on the moving reaction front are wide enough that the equations developed can be confidently used in the range of interest for packaging applications (Ferrari et al. 2009). Furthermore, the validity of the analytical estimates can be predicted by calculating $\tilde{t}_{onset}$ and $\tilde{t}_{SF}$, which are functions of the dimensionless parameters Φ_H and ν, respectively. Finally, the framework presented here is in fact applicable to multiphase reactive membranes, composed say of polymer blends (Carranza et al. 2010 b).

SUPPLEMENTAL MATERIAL – 2.A

Yang et al. (2001) proposed an approximate analytical solution for equations 2.1 and 2.2 valid for the limit of very fast reactions. Yang assumed that all reaction took place at a moving front, and that the mobile species is completely consumed at the front, hence $C(x_F,t)=0$. The moving front position obtained by this approximation $x_F=\sqrt{2\nu Dt}$ matches our results, as shown in table 2.1. However, the concentration and time lag predictions using this approximation have a narrower applicability than the 3-regime analysis presented in this chapter and are limited to infinite reaction rates. An alternate moving front approximation is to consider a non-zero concentration at the front, with the condition that the diffusion equals the rate of consumption at the front

$$J\big|_{x=x_F}=k_S\,C(x_F,t), \tag{2.A.1}$$

where $J\big|_{x=x_F}$ is the diffusive flux at the moving front and k_S is the effective surface rate constant. This approach enables the incorporation of finite reaction kinetics in the model.

Based on the analysis for intermediate times in this chapter, the mobile species concentration can be estimated by

$$C(x,t)=0.653\,C_0\,\frac{e^{-\sqrt{k_R n_0/D}\left(x-\sqrt{2\nu Dt}\right)}}{\sqrt{k_R n_0/D}\,\sqrt{2\nu Dt}}. \tag{2.A.2}$$

The flux at the moving front x_F is thus given by

$$J\big|_{x=x_F}=-D\frac{\partial C}{\partial x}\bigg|_{x=x_F}=\frac{0.653\,D\,C_0}{\sqrt{2\nu Dt}}. \tag{2.A.3}$$

Using equation 2.A.2 to calculate the concentration at the moving front, and combining it with the flux as calculated in equation 2.A.3, the rate of consumption at the moving front is first order, with an effective surface rate constant k_S. Thus, the moving front boundary is given by

$$J\big|_{x=x_F} = k_S\, C(x_F, t) \quad with \quad k_S = \sqrt{D\, k_R n_0}\,, \tag{2.A.4}$$

which is consistent with the boundary condition described by equation 2.A.1. Thus, the sharp reaction front model may be related to the diffuse reaction front model.

Nomenclature

b constant for moving front flux prediction

C O_2 concentration in the film, mol/cm^3

C_0 oxygen concentration at the surface $C_0 = p_{O_2} S$, mol/cm^3

D oxygen diffusion coefficient of the film, cm^2/s

Da Damköhler number, $Da = k_R \, n_0 L^2 / D = \tilde{L}^2$

G variable for moving front analysis

$\hat{G} = \sqrt{2\nu}\, G$

J oxygen flux, mol/cm^2 s

k_R reaction rate constant for reactive membrane, cm^3 /mol$_{RS}$ s

L thickness of the film, cm

n concentration of reactive sites, mol$_{RS}$/cm^3

n_0 initial concentration of reactive sites, mol$_{RS}$/cm^3

p_{O_2} oxygen partial pressure, MPa

Q_t oxygen permeate, mol/cm^2

S solubility coefficient for oxygen in polymer, cm^3(STP)/cm^3 MPa

t time, s

t_K kill time, s

t_L time lag, s

$t_{\min}$ time of the minimum value of the moving front equation, s

t_{onset} onset time for the initial flux plateau, s

t_{SF} time when a steady moving front is established, s

x position along film thickness, cm

x_F moving front position, cm

$\dot{x}_F$ moving front speed, cm/s

~ denotes dimensionless variables

Greek letters

η reactive sites expressed in terms of moving front coordinate

$\hat{\nu}$ stoichiometric coefficient

ν ratio between dissolved oxygen and reactive capacity, $\nu = \hat{\nu} C_0 / n_0$

ξ moving front coordinate

Φ_H Thiele's modulus, $\Phi_H = \sqrt{k_R n_0 L^2 / D} = \tilde{L}$

Chapter 3: Modeling of Reactive Polymer Blends[2]

3.1 INTRODUCTION

As discussed in Chapter 1, one of the easier ways to incorporate an oxygen-scavenging polymer into a barrier film is to simply blend a butadiene-containing polymer with a matrix polymer like poly(ethylene terephthalate), PET, or polystyrene., PS. However, owing to the immiscibility of these polymers, one can expect the oxygen-scavenging polymers to form particles in the PET or PS matrix. In principle the particle size can be controlled by rheology and compounding conditions.

While the transport of mobile species in a homogeneous reactive barrier material was studied in Chapter 2, this chapter develops the model for a reactive polymer blend consisting of an inert matrix with uniformly dispersed spherical particles of oxygen-scavenging polymer. A multiscale model is formulated here, coupling the reaction at the particle level with the transport in the bulk film. The system of non-linear partial differential equations was solved numerically over a wide parameter space relevant to packaging applications.

The model developed in this chapter assumes all particles are spheres of the same size. In practice there will often be a distribution of particle sizes and possibly shapes. In Chapter 4 the discussion is extended to non-spherical particles and develops design equations based on volume to surface ratio.

---

[2]The model and results of this chapter have appeared in Ferrari, M.C., Carranza, S., Bonnecaze, R.T., Tung, K.K., Freeman, B.D., Paul, D.R., 2009. Modeling of oxygen scavenging for improved barrier behavior: Blend films. Journal of Membrane Science 329, 183–192.

3.2 MODEL DESCRIPTION

Consider a blend film of thickness L with spherical particles of radius R uniformly dispersed throughout the film, as illustrated schematically in figure 3.1. An inert polymer, such as PET or PS is used as the matrix, and the particles are made of oxygen-scavenging polymer, OSP. Since the matrix is inert, oxygen consumption occurs solely within the OSP particles, as will be discussed later in this chapter. Oxygen diffuses in the matrix polymer according to Fick's law

$$Flux = -D_m \frac{\partial C_m}{\partial x}, \tag{3.1}$$

where D_m is the oxygen diffusion coefficient in the matrix polymer phase, C_m is the concentration of oxygen, and x is the position along the film thickness. The film is assumed to be initially devoid of oxygen, i.e., $C_m(x=0, t=0)=0$. For packaging applications, the upstream boundary is typically air, making the oxygen partial pressure $p_{O_2,0}$ = 21 kPa (0.21 atm). The downstream boundary is maintained at a low oxygen partial pressure, or for simplicity $p_{O_2,L}$ ~ 0. Oxygen is assumed to dissolve in the matrix polymer according to Henry's law at the upstream surface

$$C_m(x=0,t) \equiv C_{m,0} = S_m p_{O_2,0}, \tag{3.2}$$

where $C_{m,0}$ is the concentration of oxygen in the matrix polymer phase at $x=0$ and S_m is the effective oxygen solubility coefficient.

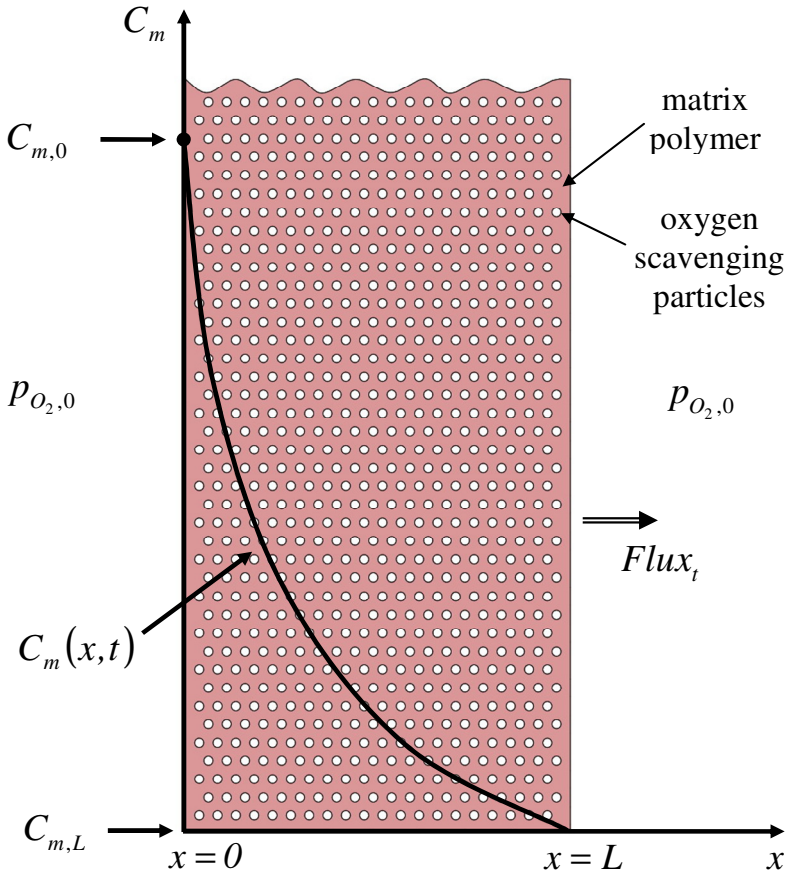

Figure 3.1: Schematic illustration of a blend film containing particles of an oxygen scavenging polymer in a matrix polymer.

3.2.2 Particle model

The oxygen consumption within the OSP particles is approximated by the shrinking core model illustrated in figure 3.2. Here it is assumed that at any given time each particle has an unreacted/unoxidized core of radius a surrounded by a completely oxidized outer shell, $R > r > a$. The radius a of the unreacted core reduces with time, until the reactive sites within the particle are completely consumed, i.e., $a = 0$. The use of the shrinking core approximation was motivated by experimental observations with

OSP, indicating the presence of an oxidation layer (Ashcroft 2007; Li 2010) which increased in thickness over time. The range of validity of the shrinking core approximation and the evaluation of an alternate kinetics model for the OSP particles are discussed in Chapter 4.

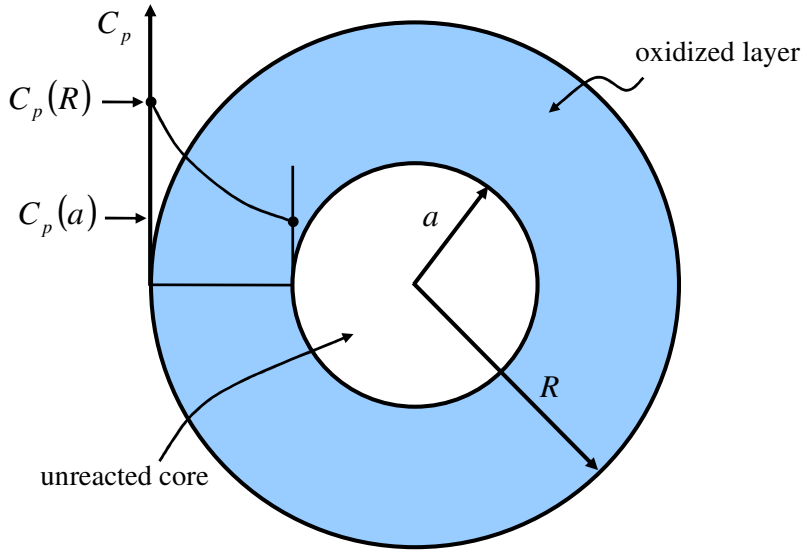

Figure 3.2: Schematic illustration of the "shrinking core" model for oxygen diffusion and reaction within an oxygen scavenging particle.

For a particle located in the film at position x (see figure 3.1), where the oxygen concentration in the matrix is $C_m(x,t)$, oxygen will partition into the oxidized surface according to

$$C_p(R) = C_m(x,t)/H, \tag{3.3}$$

where $C_p(R)$ denotes the dissolved oxygen concentration in the oxidized polymer at the interface between the particle and the matrix, H is a partition coefficient given by $H = S_m / S_p$, and S_p is the solubility coefficient for oxygen in the oxidized polymer.

The concentration $C_m(x,t)$ in the bulk polymer is assumed to change much slower relative to the time required to achieve steady state within an OSP particle, thus a pseudo-steady-state approximation is used. The concentration profile within the oxidized shell is obtained by applying the transient boundary conditions shown in figure 3.2 to the steady-state mass balance for a spherical particle,

$$\frac{D_p}{r^2}\frac{d}{dr}\left(r^2\frac{dC_p}{dr}\right)=0, \tag{3.4}$$

$$C_p = C_p(R) = \frac{C_m(x,t)}{H} \text{ at } r = R, \tag{3.5}$$

$$C_p = C_p(a) \text{ at } r = a, \tag{3.6}$$

where D_p is the oxygen diffusion coefficient in the oxidized OSP, C_p is the oxygen concentration within the particle, and $C_p(a)$ is the oxygen concentration at the reaction front. Integrating equation 3.4 twice the concentration profile in the shell for a concentration $C_p(R)$ at the particle surface is given by

$$C_p(r) = C_p(R) - \left[C_p(R) - C_p(a)\right]\left(\frac{1-R/r}{1-R/a}\right). \tag{3.6}$$

According to Fick's law, the radial oxygen flux within the particle is given by

$$J = -D_p\frac{dC_p}{dr} = -D_p\frac{C_p(R)-C_p(a)}{R/a-1}\left(\frac{R}{r^2}\right). \tag{3.7}$$

At the reaction front ($r = a$) the flux of oxygen equals the rate of oxygen consumption (Fogler 1999; Levenspiel 1999), which is approximated by a simple first order surface reaction. Thus,

$$-D_p \frac{dC_p}{dr} = -k_p C_p(a), \tag{3.8}$$

where k_p is the surface reaction rate constant for the particle. Combining equations 3.7 and 3.8, the concentration of dissolved oxygen at the reaction front can be expressed as

$$C_p(a) = C_p(R)\left[1 + \frac{k_p a^2}{D_p R}\left(\frac{R}{a} - 1\right)\right]^{-1}. \tag{3.9}$$

The Rate of Oxygen Consumption (ROC) for the single particle is given by the product of the flux of oxygen and the surface area at $r = a$,

$$ROC = 4\pi a^2 k_p C_p(a) = 4\pi a^2 k_p C_p(R)\left[1 + \frac{k_p a^2}{D_p R}\left(\frac{R}{a} - 1\right)\right]^{-1}. \tag{3.10}$$

A simple mass balance relates the time profile of the unreacted core radius to the ROC,

$$\frac{d}{dt}\left(\rho_{polymer}\frac{4\pi a^3}{3}\right) = -\frac{ROC}{\beta}\rho_{polymer}, \tag{3.11}$$

where β is OSP scavenging capacity, defined as the moles of oxygen consumed per unit volume of OSP and can be determined by experimentally measuring the mass uptake of pure OSP films (Li et al. 2008; Li 2010). Combining equations 3.10 and 3.11 leads to the dynamic equation for the radius of unreacted OSP particles,

$$\frac{\partial a}{\partial t} = -\frac{k_p C_p(R)}{\beta}\left[1 + \frac{k_p a^2}{D_p R}\left(\frac{R}{a} - 1\right)\right]^{-1}. \tag{3.12}$$

Recall that $C_p(R)$ is a function of x and t, see equation 3.5; thus the radius of the unreacted core is also a function of x and t.

3.2.3 Transport in the film

With the particle model defined, it is now possible to consider the complete membrane consisting of particles dispersed within the matrix (see figure 3.1). A one-dimensional model is used for the concentration through the film, assuming the complex three-dimensional composition field around a reactive particle does not significantly affect the bulk transport through the film. The particles are assumed to be sufficiently small, numerous, and well dispersed, so that effective and average properties over a particular film volume can be used. The transport of oxygen through the membrane can be described considering the Fickian diffusion in the matrix and the consumption due to the reaction within the particle. The latter term can be calculated from the ROC of a single particle multiplied by the number density, ρ, of particles in the film

$$\rho = \frac{3\phi}{4\pi R^3}, \tag{3.13}$$

where ϕ is the volume fraction of particles of radius R. The resulting diffusion equation is given by

$$\frac{\partial C_m}{\partial t} = D_m \frac{\partial^2 C_m}{\partial x^2} - \frac{3\phi}{R^3} \frac{a^2 k_p C_m}{H} \left[1 + \frac{k_p a^2}{D_p R} \left(\frac{R}{a} - 1 \right) \right]^{-1}. \tag{3.14}$$

This equation must be solved simultaneously with the equations describing the decrease in the radius of the unreacted core of the OSP particle for all x and t,

$$\frac{\partial a}{\partial t} = \begin{cases} -\dfrac{k_p C_m}{\beta H} \left[1 + \dfrac{k_p a^2}{D_p R} \left(\dfrac{R}{a} - 1 \right) \right]^{-1} & for \quad a \geq 0 \\ 0 & for \quad a = 0 \end{cases}. \tag{3.15}$$

The initial and boundary conditions relevant for packaging applications and transient permeation experiment are given by:

$$\text{I.C.:}\quad C_m\left(x,t=0\right)=0,\quad a\left(x,t=0\right)=R\,, \tag{3.16}$$

$$\text{B.C.:}\quad C_{m,0}\equiv C_m\left(x=0,t\right)=S_m\ p_{O_2},\quad C_{m,L}\equiv C_m\left(x=L,t\right)=0\,. \tag{3.17}$$

The equations can be expressed in a more convenient non-dimensional form by defining the following dimensionless variables

$$\tilde{C}=\frac{C}{C_{m,0}},\quad \tilde{x}=\frac{x}{L},\quad \tilde{a}=\frac{a}{R},\quad \tilde{t}=\frac{t}{L^2/D}\,. \tag{3.18}$$

The differential equations plus initial and boundary conditions become

$$\frac{\partial\tilde{C}}{\partial\tilde{t}}=\frac{\partial^2\tilde{C}}{\partial\tilde{x}^2}-3\phi\,\frac{\Phi_p\,\Delta}{\varepsilon^2 H}\left[\frac{\tilde{a}^2}{1+\Phi_p\left(\tilde{a}-\tilde{a}^2\right)}\right]\tilde{C}\,, \tag{3.19}$$

$$\frac{\partial\tilde{a}}{\partial\tilde{t}}=\begin{cases}-\dfrac{C_{m,0}}{\beta}\dfrac{\Phi_p\,\Delta}{\varepsilon^2 H}\left[\dfrac{1}{1+\Phi_p\left(\tilde{a}-\tilde{a}^2\right)}\right]\tilde{C} & for\quad \tilde{a}>0\\ 0 & for\quad \tilde{a}=0\end{cases}, \tag{3.20}$$

$$\text{I.C.:}\quad \tilde{C}\left(\tilde{x},\tilde{t}=0\right)=0\,,\ \tilde{a}\ (\tilde{x},\ \tilde{t}=0)=\ 1\,, \tag{3.21}$$

$$\text{B.C.:}\quad \tilde{C}\left(\tilde{x}=0,\tilde{t}>0\right)=1,\quad \tilde{C}\left(\tilde{x}=1,\tilde{t}>0\right)=0\,. \tag{3.22}$$

where $\Phi_p=k_pR/D_p$ is the Thiele modulus for the OSP particle, i.e., the ratio between the length scale of diffusion and the length scale of reaction, $\varepsilon=R/L$ is the ratio of the radius of the OSP and the film thickness, and $\Delta=D_p/D_m$ is the ratio of the diffusion coefficient of the OSP to the diffusion coefficient of the film matrix. The term $C_{m,0}$ is

the concentration of oxygen in the matrix at the upstream surface of the membrane and was defined in equation 3.17. Note that the product $C_{m,0}/\beta$ is dimensionless.

The non-dimensional equations 3.19 and 3.20 were solved numerically using an explicit finite difference method. The equations were discretized using a three-point central difference for the spatial derivatives and two point forward difference for the time derivatives. For this problem, the early transient as well as steady-state behavior are of interest. The numerical solution utilized variable time steps to capture the behavior over the entire time span while keeping computational times within practical limits. While the numerical solution was developed in MATLAB for convenient matrix manipulation, it did not rely on any specialized solvers. When there are no reactive particles in the matrix, the solution should reduce to the classical transient diffusion in a membrane film; the numerical results for the case with no particles was found to be in excellent agreement with the analytical solution given by Crank (1975).

The solution of equations 3.19 and 3.20 provides space and time profiles for the dimensionless oxygen concentration, $\tilde{C}(\tilde{x},\tilde{t})$, and the dimensionless radius of the unreacted core of the OSP particles, $\tilde{a}(\tilde{x},\tilde{t})$. For barrier applications, it is important to know the time evolution of the oxygen flux and the cumulative amount of permeate, Q_t, exiting the downstream surface of the barrier film. Both quantities can be derived from the concentration profile. The flux is given by

$$Flux_t \equiv J(x=L,t) = -D_m \left.\frac{\partial C}{\partial x}\right|_{x=L} = -D_m \frac{C_{m,0}}{L} \left.\frac{\partial \tilde{C}}{\partial \tilde{x}}\right|_{\tilde{x}=1} \quad , \tag{3.23}$$

$$\tilde{J}\Big|_{\tilde{x}=1} = \frac{Flux_t}{Flux_{ss}} = -\frac{\partial \tilde{C}}{\partial \tilde{x}}\Big|_{\tilde{x}=1}, \tag{3.24}$$

where $D_m C_{m,0}/L$ is the flux at steady state. The cumulative amount of permeate is given by

$$Q_t = \int_0^t J\Big|_{x=L} dt = -Flux_{ss}\frac{L^2}{D_m}\int_0^{\tilde{t}} \frac{\partial \tilde{C}}{\partial \tilde{x}}\Big|_{\tilde{x}=1} d\tilde{t} = -Flux_{ss} 6\theta_0 \int_0^{\tilde{t}} \tilde{J}\Big|_{\tilde{x}=1} d\tilde{t}, \tag{3.25}$$

$$\frac{Q_t}{Flux_{ss}\theta_0} = -6\int_0^{\tilde{t}} \frac{\partial \tilde{C}}{\partial \tilde{x}}\Big|_{\tilde{x}=1} d\tilde{t} = -6\int_0^{\tilde{t}} \tilde{J}\Big|_{\tilde{x}=1} d\tilde{t}, \tag{3.26}$$

where $\theta_0 = L^2/6D_m$ is the diffusion time lag for the matrix without any OSP. From the dimensionless equations we see that $\tilde{C}$ is a function of $\tilde{x}$ and $\tilde{t}$ plus the dimensionless parameters ϕ, $C_{m,0}/\beta$, Δ, ε, H and Φ_p. Consequently, $\frac{Flux_t}{Flux_{ss}}$ and $\frac{Q_t}{Flux_{ss}\theta_0}$ are functions of $\tilde{t}$ and the same dimensionless parameters.

The dimensionless flux presented in the results section was obtained numerically from equation 3.24 using the five-point backward difference at $\tilde{x} = 1$. The dimensionless oxygen permeate was obtained numerically from equation 3.26 using the trapezoidal rule for integration. Note that the dimensionless time used in the derivation is defined as $\tilde{t} = t/\left(L^2/D_m\right)$; however, for comparison with diffusion time scales, all graphs presented in the results section use $t/\theta_0 = 6\,\tilde{t}$.

3.3 MODEL PARAMETER RANGES

The mathematical model described in the previous section contains numerous parameters that must be determined or specified to make the model predictive, see summary in table 3.1. These parameters are discussed here with some selections made for the purpose of showing example predictions in the next section. The thickness L of typical barrier film or sheet would generally be in the range 50 to 500 μm. Polymer particles dispersed in a polymer matrix prepared by melt compounding and extrusion would have radii R in the range of 0.5 to 5 μm (Paul and Bucknall 2000). The volume fraction ϕ of these particles in the blend might be expected to be within the range of 0.05 to 0.20. A typical matrix polymer might be poly(ethylene terephthalate), PET, which is used extensively for conventional barrier applications. Published values of S_m and D_m for PET from the literature (Polyakova et al. 2001) are shown in table 3.1. Values for polystyrene, which is not such a good barrier material, are also included in table 3.1. As of yet, there are no reported values of S_p and D_p for butadiene-based polymers (the oxygen-scavenging polymer of interest here) in the fully oxidized state. Since the fully oxidized material is hard and glassy, one could expect S_p to be similar to S_m. Efforts are underway currently to evaluate S_p, D_p and k_p from oxygen uptake experiments like those recently published (Li et al. 2008; Li 2010); an analysis of such data will be the subject of a forthcoming publication. For now, table 3.1 includes some preliminary estimates of the ranges of D_p and k_p from this type of analysis. The parameter β characterizes the ultimate oxygen scavenging capacity of the butadiene-based polymer,

which has been found experimentally to be in the range of 8- 32% by weight. The values of β in table 3.1 reflect this range in the units shown.

Table 3.1: Range of model parameters of interest.

Parameter	Estimated Range	Base Case for Calculations	Ref
L	50 to 500 μm	250 μm	
R	0.5 to 5 μm	2.5 μm	
ϕ	0.05 to 0.20	0.1	
S_m	0.97 cm^3(STP)/cm^3 MPa (0.098 cm^3(STP)/cm^3 atm) for PET 1.9 cm^3(STP)/cm^3 MPa (0.19 cm^3(STP)/cm^3 atm) for PS	0.97 cm^3(STP)/cm^3 MPa (0.098 cm^3(STP)/cm^3 atm)	a) b)
D_m	5.6 x 10^{-9} cm^2/sec for PET 1.0x 10^{-7} cm^2/sec for PS	5.6 x 10^{-9} cm^2/sec	a) b)
S_p	measurements needed, probably ~ S_m	0.97 cm^3(STP)/cm^3 MPa (0.098 cm^3(STP)/cm^3 atm)	
D_p	estimated to be ~(1 to 6) x 10^{-9} cm^2/sec	2 x 10^{-9} cm^2/sec	
k_p	estimated to be 10^{-5} to 10^{-3} cm/sec	8 x 10^{-5} cm/sec	
β	(2.5 to 10) x 10^{-3} mol O_2/cm^3 OSP	4 x 10^{-3} mol O_2/cm^3 OSP	
$H = \frac{S_m}{S_p}$	~1	1	
$\varepsilon = \frac{R}{L}$	10^{-3} to 50 x 10^{-3}	10^{-2}	
$\Delta = \frac{D_p}{D_m}$	10^{-2} to 100	2/5.6 for PET	
$\Phi_p = \frac{k_p R}{D_p}$	0.1 to 500	10	

a) Polyakova et al. 2001, b) Hodge et al. 2001

The physical parameters described above were used to estimate the range of values the various dimensionless groups in the model, see equations 3.18-3.22, might be expected to have. Table 3.1 also lists a "base case" set of parameters that will be used in the next section to illustrate the model predictions; this case considers PET as the matrix and uses mid-range values of the geometrical parameters. Some of the calculations shown later illustrate the effects of varying some of these parameters from the base case. For reference, the diffusion time lag for a PET film with a thickness of 250 μm without scavenging particles would be $\theta_0 = L^2/6D_m$ ~5.2 hours. For polystyrene, θ_0 at this thickness would be only 0.3 hours.

It should be noted that in this model, the physical effects of the particles on the oxygen diffusion process have been ignored. In the extreme case, the particles might be considered impermeable in which case Maxwell's equation (Maxwell 1872) would predict the following relationship between the steady-state permeability of the blend, P_{blend}, to that of the matrix, P_m

$$\frac{P_{blend}}{P_m} = \frac{1-\phi}{1-\phi/2}, \tag{3.27}$$

which for ϕ = 0.2 amounts to about an 11% reduction for the blend. This is of no consequence for the current considerations.

3.4 EXAMPLE CALCULATIONS

In this section, numerical calculations made are shown to illustrate the predictions of the model developed in this chapter. The model involves a considerable parameter space so the strategy here is to use the "base case" values listed in table 3.1 and then

systematically explore the trends produced by varying each parameter individually within the "estimated range" shown in table 3.1; however, it is instructive to examine cases when the rate parameter k_p is outside this range.

Figure 3.3 explores the effect of varying the loading of oxygen-scavenging polymer in a matrix of poly(ethylene terephthalate) or PET. Figure 3.3a shows results in terms of the dimensionless cumulative amount of oxygen exiting the downstream surface of the film versus dimensionless time (defined here as t/θ_0) for several values of ϕ all plotted on arithmetic coordinates. After an initial transient period, a linear asymptote is approached which can be extrapolated to the time axis to define the time lag θ with scavenging. Note that scavenging extends the time lag by several thousand-fold. However, such plots do not give a full picture of what is happening for times less than θ; as discussed in Chapter 1, the "leakage" through the film for $t < \theta$ is of great interest. Figure 3.3b shows the dimensionless downstream oxygen as a function of dimensionless time plotted on a log-log scale, which enables visualization of small leakage for $t < \theta$. All flux plots in this chapter are presented in the same manner. Here, the fluxes for times $t < \theta$ are at least 10^4 times smaller than the steady-state values, but it will be shown later that the leakage flux is not always so small.

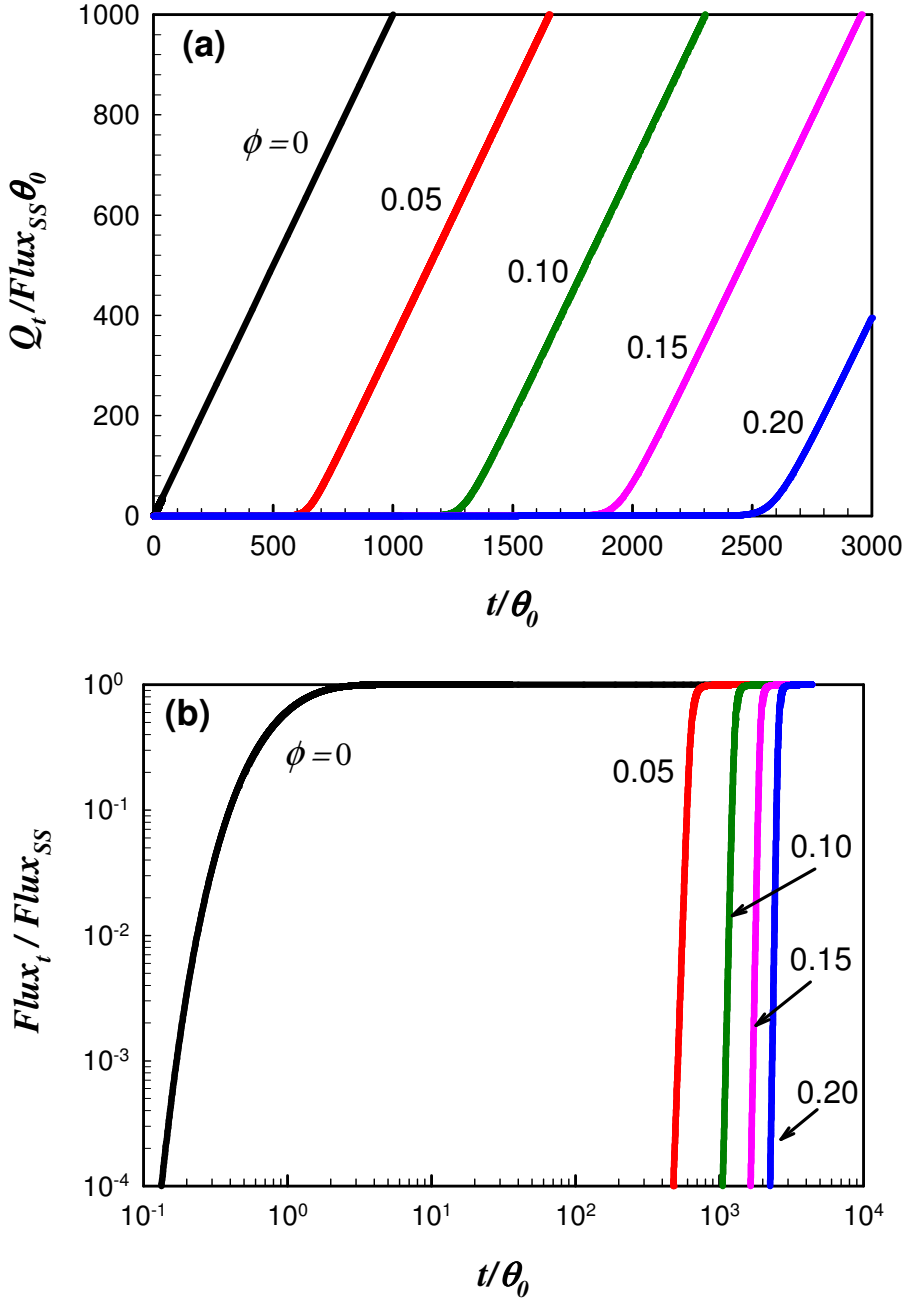

Figure 3.3: Predicted transient permeation behavior for a blend film containing various volume fractions of oxygen scavenging polymer shown as (a) cumulative oxygen permeate and (b) flux of oxygen exiting the downstream film surface. All parameters set at base case values (see table 3.1) except for ϕ as noted.

Figure 3.4 shows analogous plots as in figure 3.3 where β is varied rather than ϕ. Increasing the capacity of the oxygen-scavenging polymer to take up oxygen for a fixed loading ϕ = 0.10 by increasing β has somewhat similar effects as increasing ϕ. Interestingly, the asymptotic solutions illustrated in figure 3.3a and figure 3.4a, and consequently θ, are independent of the kinetics of the scavenging reactions and all the parameters that affect the rate of reaction. Thus, θ/θ_0 depends only on the capacity to absorb oxygen, ϕ and β, and the solubility of oxygen in the polymer matrix or $C_{m,0}$. As shown in the Chapter 4, the method of Frisch (1957) used for homogeneous film in Chapter 2 can be used to develop the following analytical expression for θ/θ_0

$$\theta/\theta_0 = 1 + 3\phi\beta/C_{m,0} \,. \tag{3.28}$$

Figure 3.5 shows how the time lag relative to the case of no scavenging depends on ϕ and β for PET (3.5a) and PS (3.5b) matrices calculated by numerical solution of the model described above; these values of θ/θ_0 are in excellent agreement with those calculated by equation 3.28. These plots are linear and could be collapsed into master plots for all matrix polymers using the dimensionless ratio $C_{m,0}/\beta$ rather than β as the parameter, as predicted by equation 3.28. Note that owing to the lower solubility of oxygen in PET than PS, see table 3.1, the extension of the time lag caused by scavenging is greater for PET than PS by almost a factor of two.

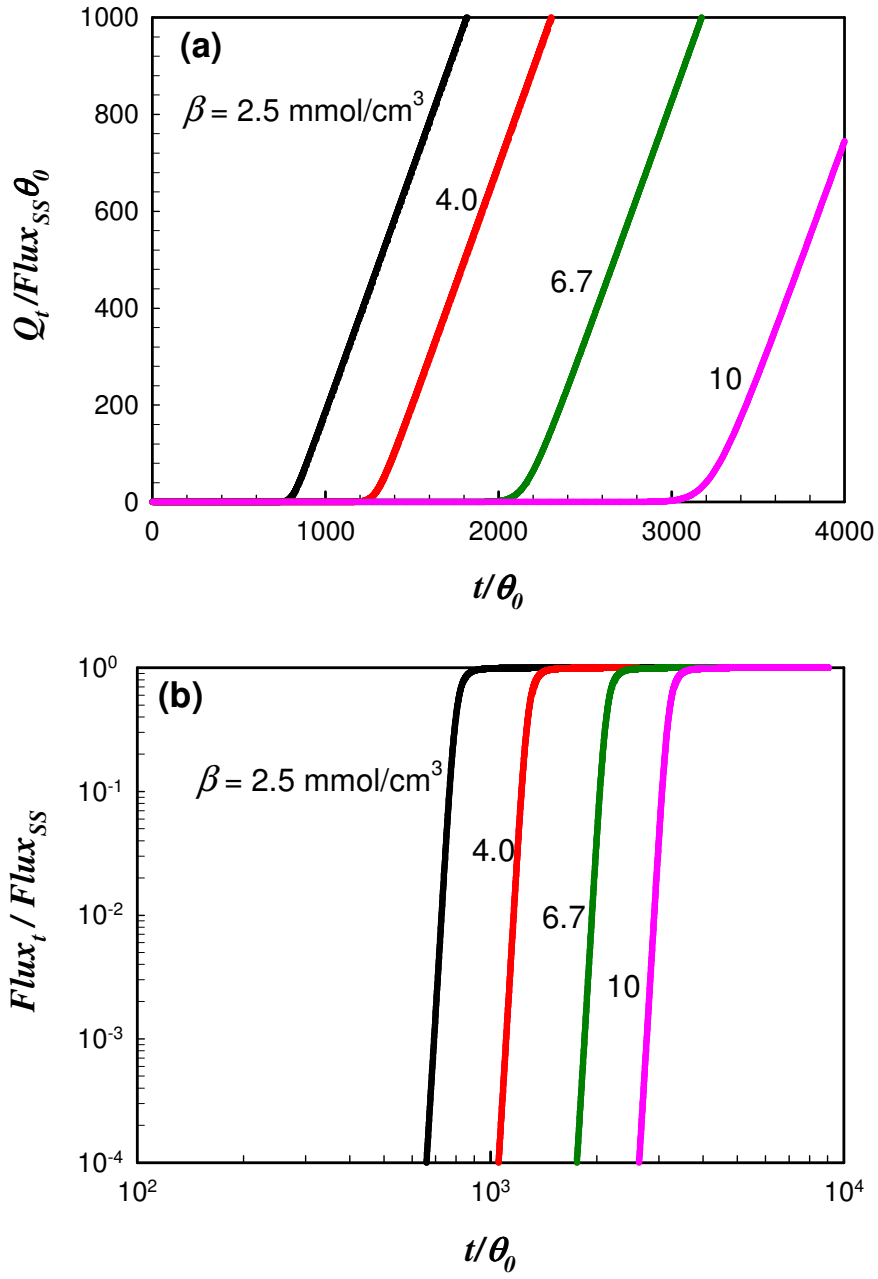

Figure 3.4: Predicted transient permeation behavior for a blend film containing various volume fractions of the oxygen reaction capacity of the oxygen scavenging polymer shown as (a) cumulative oxygen permeate and (b) flux of oxygen exiting the downstream film surface. All parameters set at base case values (see table 3.1) except for β as noted; β is given in units of millimoles O_2/cm^3 OSP.

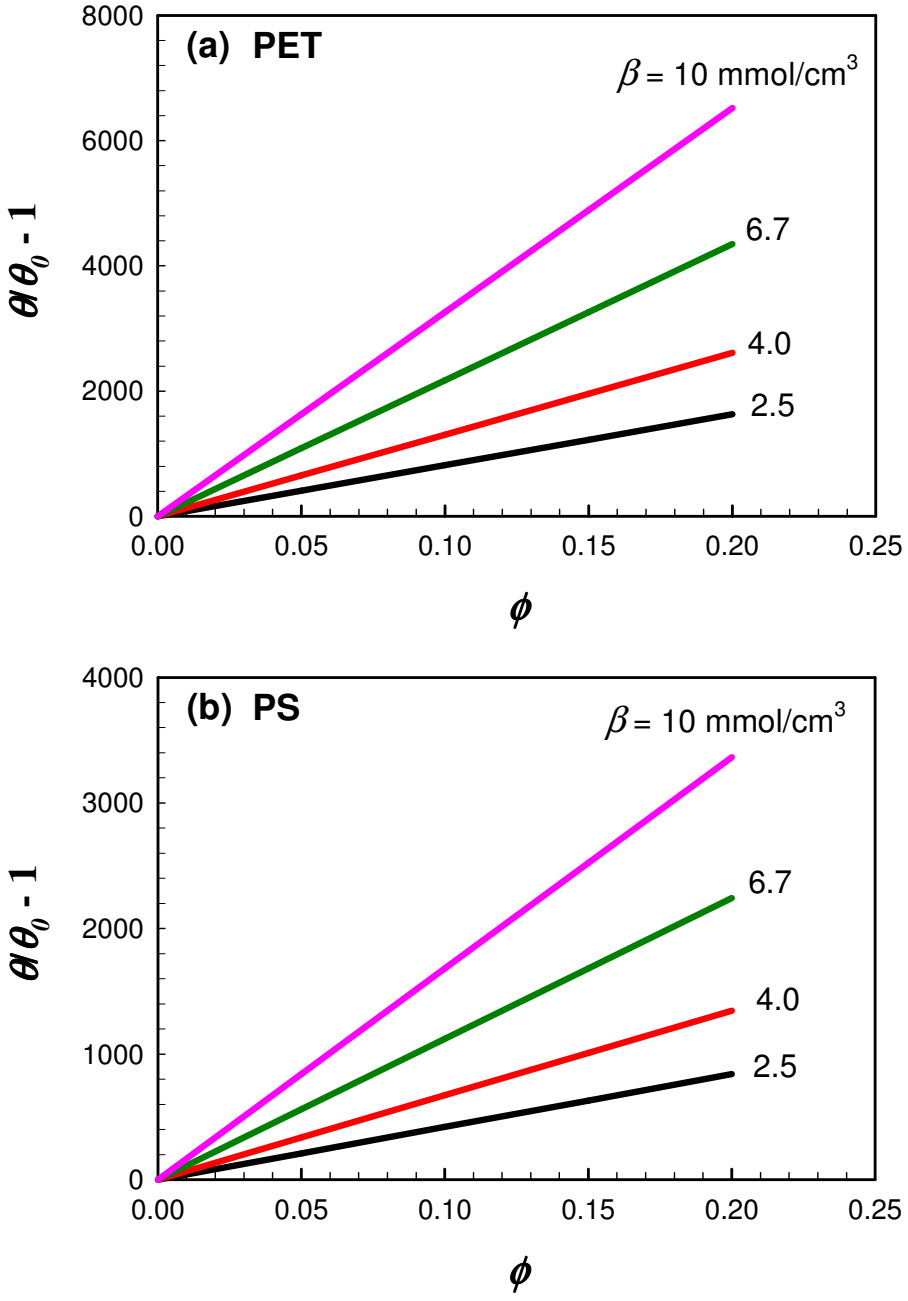

Figure 3.5: Predicted extension of the transient permeation time lag, θ, caused by scavenging as function of ϕ and β for (a) poly(ethylene terephthalate) and (b) polystyrene as the matrix polymer. All parameters set at base case values (see table 3.1) except as shown.

Figure 3.6 shows how the transient response varies with the reaction rate constant k_p. All parameters are set at the base case values, except for k_p, as indicated in the charts. Values of k_p well below the range presented in table 3.1 are used to illustrate the effects on the transient flux. All cumulative oxygen permeate curves in figure 3.6a eventually approach a single asymptote with θ/θ_0 ~ 1250, except of course, for the case of no scavenging ($k_p = 0$), with $\theta/\theta_0 = 1$. Clearly, the approach to this asymptote depends strongly on k_p. The effect of k_p is better illustrated by figure 3.6b, which shows the downstream oxygen flux versus time using logarithmic scales. There are two rapid rises in flux; the first occurs at times of the order of θ_0 and the second at times of order of θ with a plateau region between these limits. As discussed in Chapter 2, this plateau region was also present in homogeneous reactive films. Analytical predictions for the value of the plateau region as well as the plateau start and end times were derived in Chapter 2 for homogeneous films and in Chapter 4 for polymer blends. Note that figures 3.3b and 3.4b don't show a plateau region because the flux lower limit in the graph is set to 10^{-4} but the plateau is on the order of 10^{-43}.

Figure 3.7 shows, on a time scale zoomed near $t \sim \theta$, how the radius R of the OSP particles affects the flux of oxygen exiting the film. For a given time, the flux increases as the particles become larger owing to the coupling of mass transfer within the particle with the reaction, see figure 3.2. Clearly, there is some advantage to having the OSP finely dispersed in the matrix polymer.

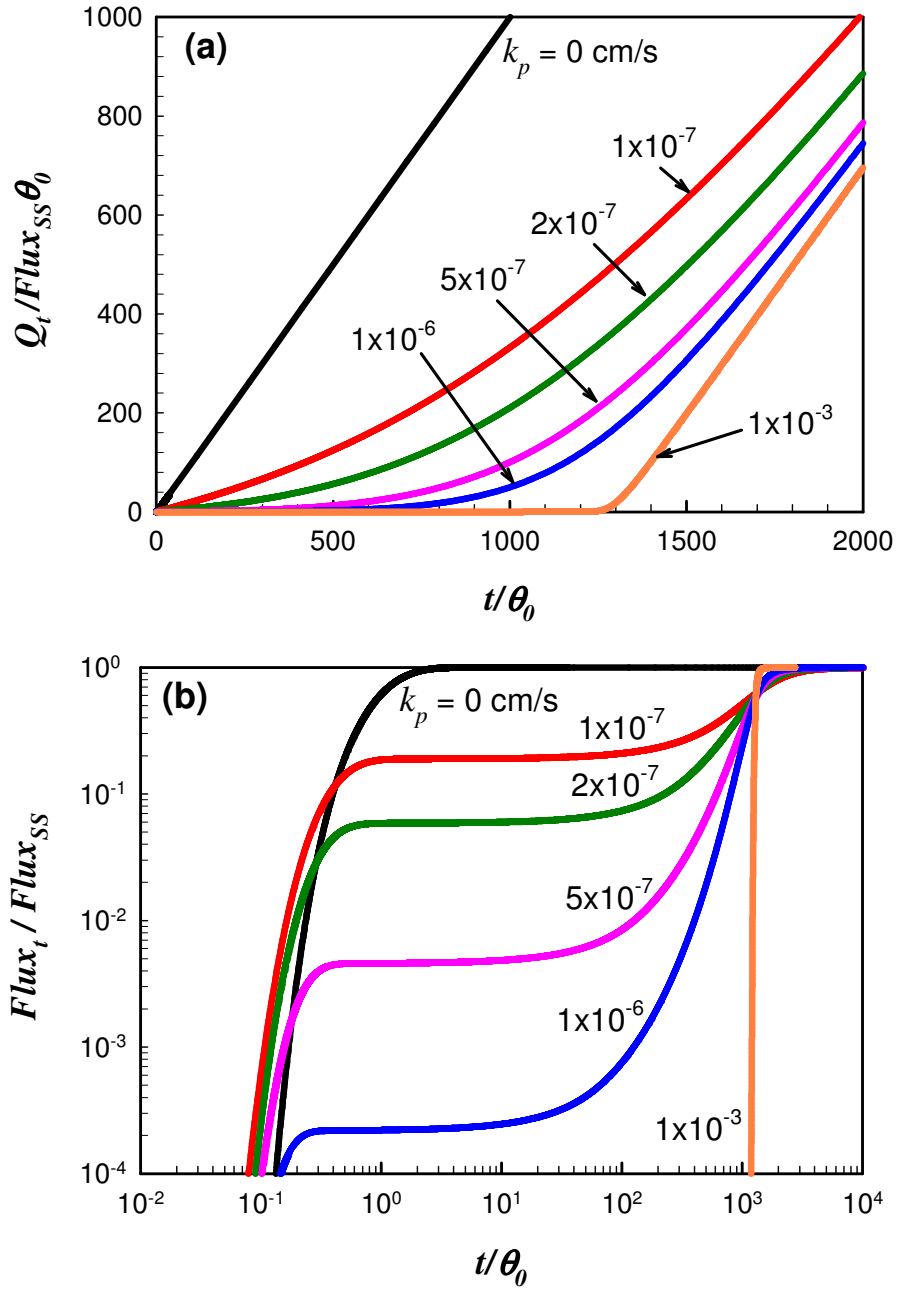

Figure 3.6: Predicted transient permeation behavior for a blend film for different values of the oxygen scavenging reaction rate shown as (a) cumulative amount of oxygen and (b) flux of oxygen at the downstream film surface. All parameters set at base case values (see table 3.1) except for k_p as noted.

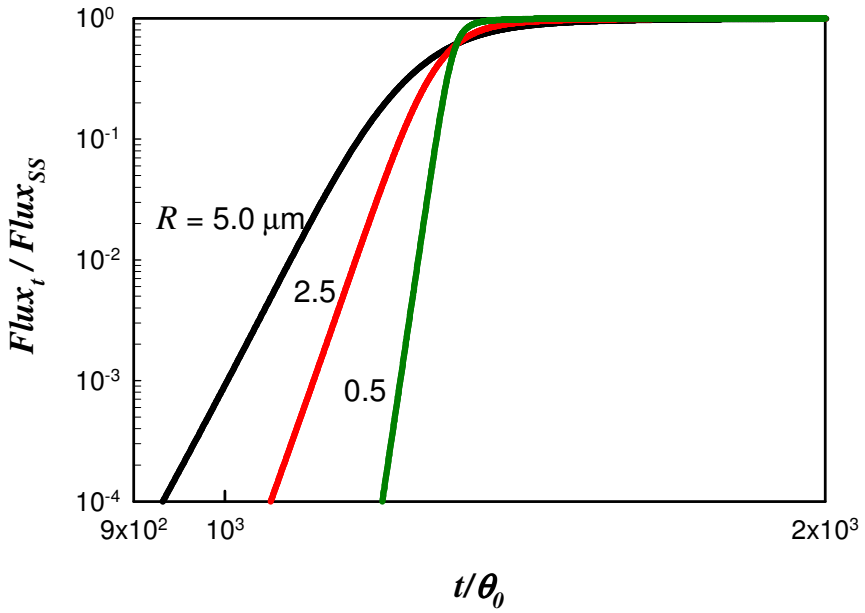

Figure 3.7: Predicted effect of oxygen scavenging polymer particle radius on the flux of oxygen exiting the blend film. All parameters set at base case values (see table 3.1) except R as noted.

Figure 3.8a shows the effects of the overall film thickness L on the dimensionless flux at a given dimensionless time, with all other parameters corresponding to the base case. The dimensionless flux becomes larger as the film becomes thinner, which can be explained looking at the times scales for reaction, which is independent of L, and diffusion $\theta_0 \propto L^2$. For thinner films there is less time for the scavenging reaction to occur before oxygen breakthrough. As the value of k_p becomes lower the extent of "leakage" in the time range $\theta_0 < t < \theta$ relative to $Flux_{SS}$ becomes more significant and strongly dependent on L as illustrated in figure 3.8b for $k_p = 5\times10^{-7}$ cm/sec for various values of L with all other parameters corresponding to the base case. The effect on the absolute flux leakage is even greater since $Flux_{SS} \propto L^{-1}$.

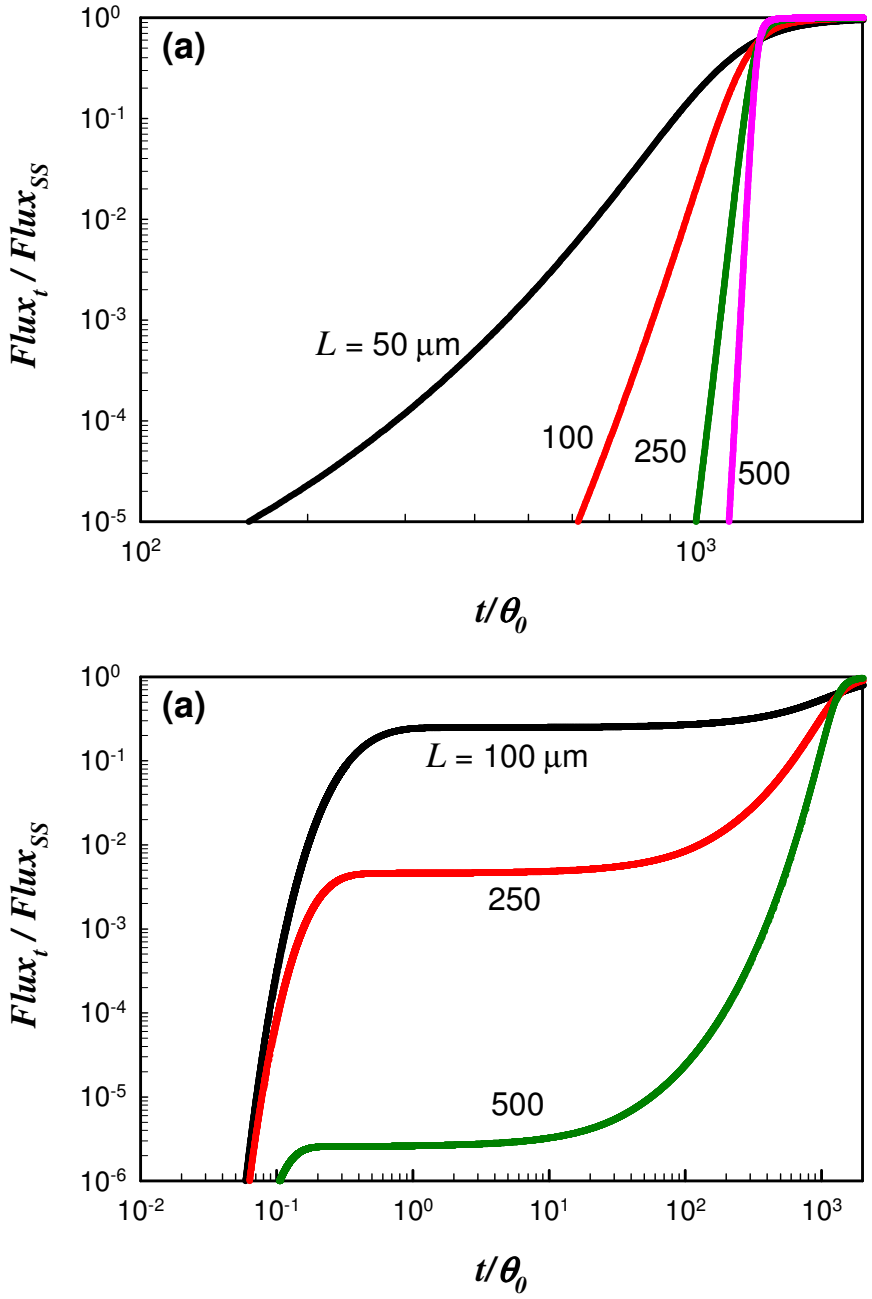

Figure 3.8: Predicted effect of blend film thickness on oxygen flux exiting the downstream surface for (a) $k_p = 8\times10^{-5}$ cm/sec (note expanded time scale) and (b) $k_p = 5\times10^{-7}$ cm/sec. All other parameters set at base case values (see table 3.1) except L as noted.

The effect of the diffusion coefficient within the oxidized layer of the butadiene containing particles, D_p, over the expected range of values (2 to 6) x 10^{-9} cm^2/sec, see table 3.1, turns out to be very small as illustrated in figure 3.9 where the dimensionless flux is plotted versus an expanded time scale in the vicinity of θ. Reducing the values of D_p by and order of magnitude to 2 x 10^{-10} cm^2/sec produces a more noticeable effect, as seen in figure 3.9. Overall, D_p is not a very influential parameter in the barrier performance of blend films as represented by this model.

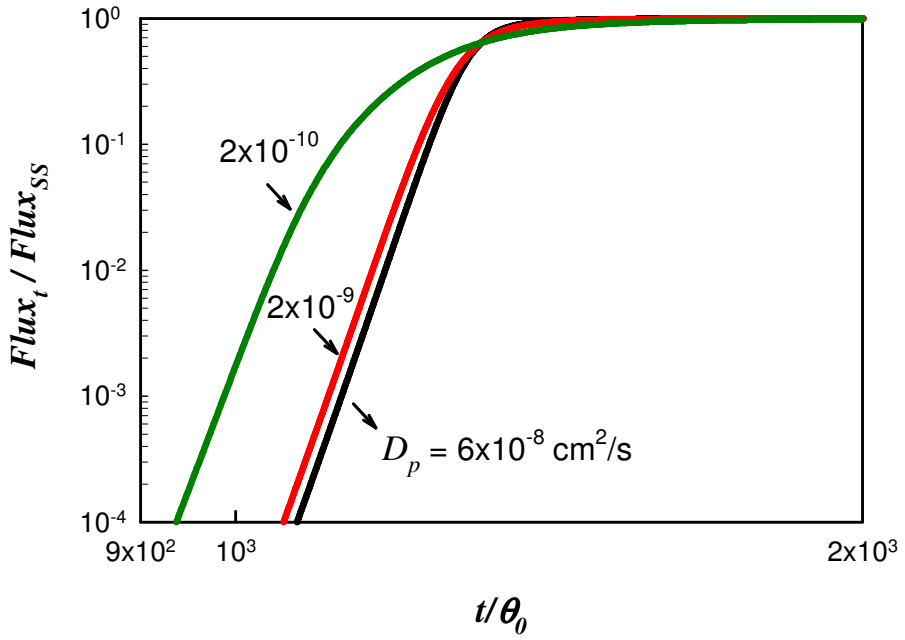

Figure 3.9: Predicted effect of diffusion coefficient in the oxidized layer of the oxygen scavenging particle on the oxygen flux exiting the downstream surface of the blend film. All parameters set at base case values (see table 3.1) except for D_p as noted.

As a final issue, the effect of varying the matrix polymer is explored by comparing the performance of films based on PS versus PET as the matrix; all the parameters are kept the base case values given in table 3.1 except for changing S_m and D_m to the values for PS. Because of the higher oxygen solubility in PS, the dimensionless time lag θ/θ_0 is smaller for PS than PET, see figure 3.10a; of course, because of the higher D_m of PS than PET, the value of θ_0 is about 18 times smaller for PS than PET. Considering the effect of both S_m and D_m, the absolute value of θ for PET is about 37 times that of PS. Furthermore, the slope of the dimensionless flux-time plots for PET is much steeper than for PS in the region of θ, see figure 3.10b. PS is prone to show greater "leakage" permeation in the region $t < \theta$ than PET.

The effects illustrated quantitatively above by actual numerical solution of the model equations can be understood qualitatively, within certain limitations, by examining the scavenging terms in the model, i.e., the last term in equations 3.19 and 3.20 for $\tilde{a} < 0$. A more rigorous analysis leading to the development of design equations is presented in Chapter 4. As seen earlier, θ/θ_0 is a function of ϕ and $C_{m,0}/\beta$ only, and they affect the outcome in opposite directions. Increasing $C_{m,0}/\beta$, which appears only in equation 3.20 accelerates the rate of change of the shrinking core radius a and results in a decrease of θ/θ_0. Conversely, increasing ϕ, which appears only in equation 3.19, accelerates the rate of change of the oxygen concentration $\tilde{C}$ and results in an increase of θ/θ_0.

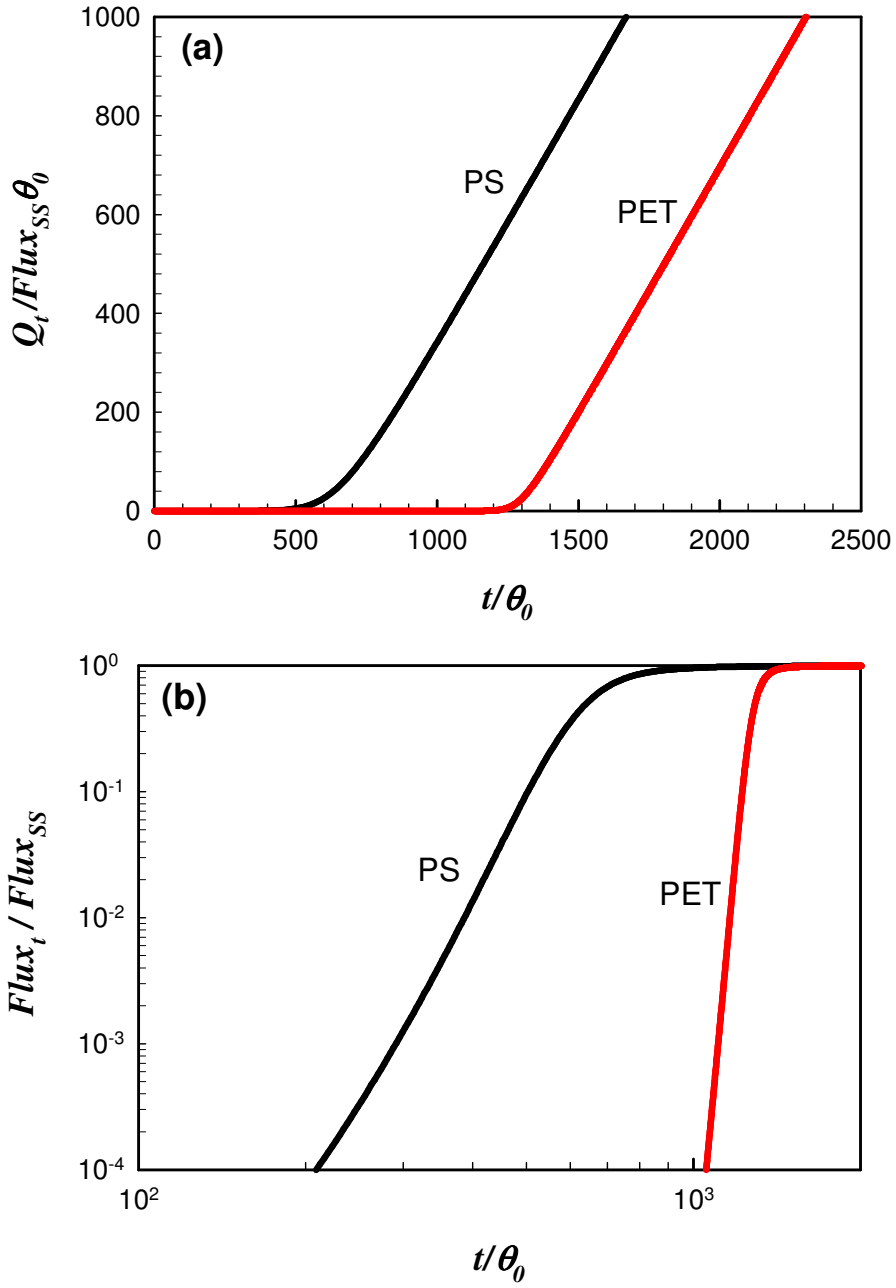

Figure 3.10: Comparison of predicted transient permeation behavior for poly(ethylene terephthalate) versus polystyrene as the matrix polymer shown as (a) cumulative amount of oxygen and (b) flux of oxygen exiting the downstream surface of blend film. All parameters set at base case values (see table 3.1) except as needed for polystyrene.

The effective Thiele modulus for the blend

$$\Phi_b = \sqrt{\frac{3\phi\Phi_p\Delta}{\varepsilon^2 H}} = \sqrt{\frac{3\phi k_p L^2}{RD_m H}}, \tag{3.29}$$

appears in equation 3.19 as $\Phi_b^{\,2}$ and plays a dominant role in the extent of leakage flux prior to reaching the asymptotic steady-state flux. However, the Thiele modulus for the scavenging particle, Φ_p, appears in the variable term in braces, and plays a more limited role since it is damped by the $\left(\tilde{a} - \tilde{a}^2\right)$ term. In general, the extent of leakage flux prior to reaching the asymptotic steady-state flux can be reduced by making choices (materials, formulation, and geometry) that maximize the effective Thiele modulus Φ_b.

3.5 SUMMARY AND CONCLUSIONS

A model has been developed for predicting the oxygen barrier behavior of a blend film containing particles of an oxygen-scavenging polymer, e.g., polymers containing butadiene segments, dispersed in a matrix polymer. It is assumed that the oxygen scavenging by the particles can be described by a "shrinking core" model while the diffusion of oxygen in the matrix can be approximated as a function only of the coordinate axis in the thickness direction and of time. The model equations have been solved numerically for the cases where the matrix polymer is either poly(ethylene terephthalate) or polystyrene for values of the geometric and physical parameters that are believed to be realistic in order to show how barrier behavior is affected by each one. Scavenging extends the time lag θ for transient permeation by a factor that depends only on the loading of the oxygen-scavenging polymer and its capacity to consume oxygen

relative to the capacity of the matrix polymer to dissolve oxygen; the time lag can easily be extended by factors of thousands. However, for demanding applications like displays based on organic light-emitting diodes, the flux of oxygen exiting the downstream surface of the film on time scales of the order of θ and less may be the limiting criteria for the utility of this technology. This model was used to estimate this leakage flux for $t < \theta$, which depends on the factors that affect the rate of oxygen consumption relative to the rate of oxygen diffusion and can be summarized in terms of an effective Thiele modulus. As it will be discussed in Chapter 4, similar predictions can be done for scavenging concepts for other species like water and carbon dioxide by replacing the appropriate kinetic details.

Nomenclature

a	radius of the unreacted core, see figure 3.1
C_m	oxygen concentration in matrix polymer
C_p	oxygen concentration in oxidized scavenging polymer
Da	Damköhler number
D_m	diffusion coefficient for oxygen in matrix polymer
D_p	diffusion coefficient for oxygen in oxidized scavenging polymer
H	partition coefficient, S_m / S_p
k_p	oxidation rate constant for the scavenging particle
L	film thickness
p_{O_2}	oxygen partial pressure
P	oxygen permeability coefficient
Q_t	cumulative amount of oxygen permeate
R	scavenging polymer particle radius
S_m	solubility coefficient for oxygen in matrix polymer
S_m , S_p	solubility coefficient for oxygen in oxidized scavenging polymer
t	time
x	position in film
~	denotes dimensionless variables, see equation 3.18

Greek Symbols

β	oxygen scavenging capacity, moles O_2/cm^3 OSP

$\Delta = D_p / D_m$

$\varepsilon = R / L$

ϕ volume fraction of scavenging polymer

Φ_b effective Thiele's modulus for the polymer blend, $\Phi_b = \sqrt{3\phi k_p L^2 / R D_m H}$

Φ_p Thiele's modulus for the scavenging particle, $\Phi_p = k_p R / D_p$

θ time lag with scavenging

θ_0 time lag without scavenging

$\rho_{polymer}$ density of scavenging polymer

Chapter 4: Analytic Formulae for Reactive Polymer Blends[3]

4.1 INTRODUCTION

Chapter 3 developed a multiscale model to describe polymer blends of reactive spherical particles in an inert polymer matrix. The system of non-linear partial differential equations was solved numerically over a wide parameter space relevant to packaging applications. This chapter significantly extends the methodology described in Chapter 2 (Carranza et al. 2010) for homogeneous reactive membranes to derive design formulae for polymer blends. It is also shown that this analytical approach can be easily adapted for blends to the practically important case of non-spherical particles. Furthermore, the methodology is demonstrated to accommodate variations in the kinetic model within the reactive particle. In fact it is found that the functional forms of the design equations obtained by asymptotic analysis are independent of the details of the reactive term in the model equations. In particular the limits of fast and slow reactions within the particles are considered here. The derivation of analytical design equations based on approximate solutions of the non-linear model eliminates the need for lengthy simulations and provide clear relationships between critical design parameters and the physical and chemical properties of the polymer blend.

The results in this chapter will be developed in the context of oxygen scavenging but in fact are generally applicable to any reactive permeate and barrier system. Three

[3]Much of this chapter has appeared in Carranza, S., Paul, D.R., Bonnecaze, R.T., 2010b. Analytic formulae for the design of reactive polymer blend barrier materials. Journal of Membrane Science 360, 1-8.

regimes for the flux of oxygen were observed in the numerical solutions of the multiscale model. At early times an initial quasi-steady-state flux occurs. This leakage flux, though much smaller than that at true steady state when all the scavengers have been consumed, is likely the most critical characteristic of such barrier materials. At intermediate times, the initial plateau gives way to a transient regime with increased oxygen flux, leading to the final regime, characterized by the time lag, when the flux approaches its steady-state value. Analytical estimates for the initial flux plateau, for the intermediate transient flux, the time lag and kill time are presented along with their ranges of validity. The extent and nature of the dependence of each regime on the particle geometry and reactivity is discussed.

4.2 MODEL DESCRIPTION

Consider a membrane composed of reactive particles in an inert polymer matrix, as illustrated schematically in figure 4.1. The matrix is typically an inert polymer with good mechanical properties, such as poly(ethylene terephthalate) (PET) or polystyrene (PS), while the particles are oxygen scavenging polymers (OSPs) such as polybutadiene (PB). As the matrix is inert, the reaction is confined to the scavenging particles. The particles and the matrix are assumed initially devoid of oxygen. A transport model at the particle-scale is first developed and then used to develop a multiscale transport model in a film of the blend.

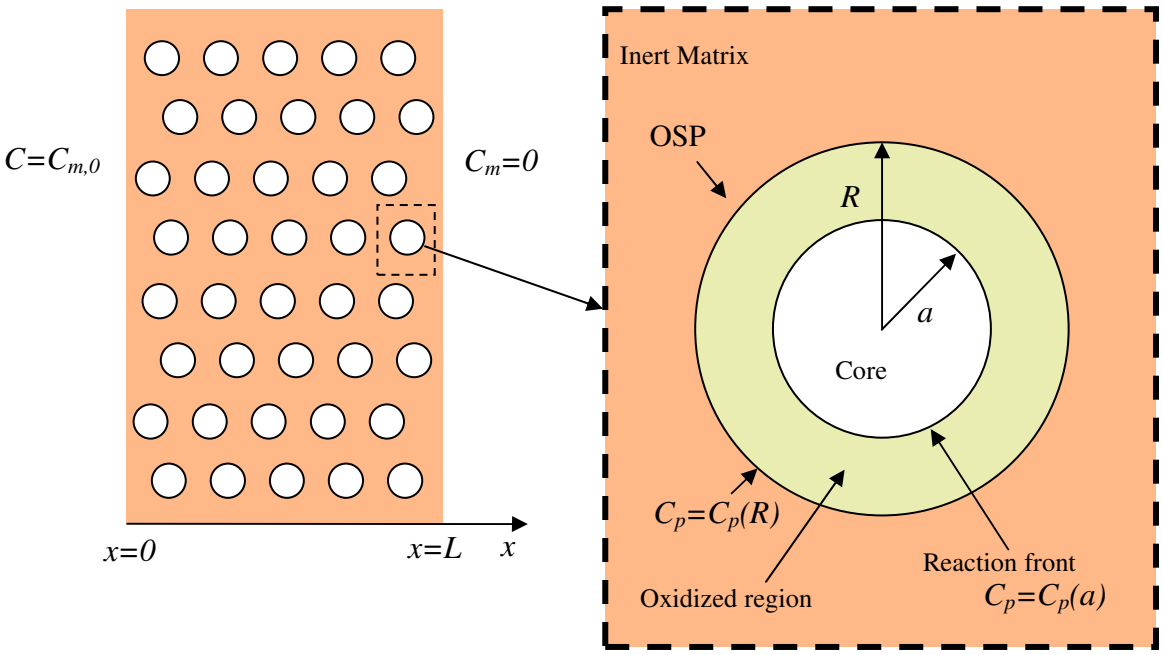

Figure 4.1: Schematic illustration of the polymer blend film and a particle in the limit of fast reaction.

4.2.2 Particle model

The reactive sites within each particle are immobilized and are consumed as the reaction progresses. Oxygen transport through the particle obeys Fick's law. Initially, the particles are devoid of oxygen and all reactive sites are available. The material balances, initial and boundary conditions for oxygen and the reactive materials within a spherical particle, for example, are given by

$$\frac{\partial C_p}{\partial t} = \frac{D_p}{r^2}\frac{\partial}{\partial r}\left(r^2 \frac{\partial C_p}{\partial r}\right) - k_R n C_p , \tag{4.1}$$

$$\frac{\partial n}{\partial t} = -\hat{\nu}\, k_R\, n\, C_p , \tag{4.2}$$

$$\text{I.C.:}\quad C_p\left(r,t=0\right)=0,\quad n\left(r,t=0\right)=n_0\,,$$

$$\text{B.C.:}\quad \left.\frac{\partial C_p}{\partial r}\right|_{r=0}=0,\quad C_p\left(r=R,t\right)=C_m/H\,, \tag{4.3}$$

where C_p is the oxygen concentration within the OSP particle, t is time, r is the radial position in spherical coordinates, D_p is the oxygen diffusion coefficient within the particle, k_R is the bulk reaction rate constant for reactive particle, n is the concentration of reactive sites, $\hat{v}$ is the stoichiometric constant relating moles of oxygen to moles of reactive sites, R is the radius of the OSP particle, C_m is the concentration of oxygen in the inert matrix, $H=S_m/S_p$ is the partition coefficient relating the solubility of oxygen in the matrix S_m to the solubility of oxygen oxidized OSP S_p, and n_0 is initial concentration of reactive sites. We will now consider the limiting cases of very fast reaction and very slow reaction.

Reaction is much faster than diffusion

Do (1982) has shown that for cases where reaction is much faster than diffusion within the particle, i.e., the Thiele modulus $\Phi_p=\left(R^2k_R\,n_0/D_p\right)^{1/2}\gg 1$, the shrinking core model is valid. In the shrinking core model the reaction progresses as a moving front, consuming the immobilized sites behind the front, and leaving an unreacted shrinking core ahead of the front. The pseudo-steady-state concentration at the particle's moving front and the rate of change of the core radius are thus given by Ferrari et al. (2009);

$$C_p(a) = \frac{C_m}{H}\left(1+\frac{k_p a^2}{D_p R}\left(\frac{R}{a}-1\right)\right)^{-1}, \tag{4.4}$$

$$\frac{\partial a}{\partial t} = -\frac{\hat{\nu}\, k_p}{n_0}\frac{C_m}{H}\left(1+\frac{k_p a^2}{D_p R}\left(\frac{R}{a}-1\right)\right)^{-1}, \tag{4.5}$$

where C_m is the oxygen concentration in the inert matrix, k_p is an effective surface rate constant, a is the radius of the reactive core and R is the radius of the OSP particle. The effective surface rate constant in the moving front regime is given by $k_p = \sqrt{D_p k_R n_0}$, as shown in Carranza et al. (2010). Sample calculations of the reactive length scale $L_{rxn} = \sqrt{D_p / k_R n_0} = D_p / k_p$, covering the range of values used in numerical calculations of Ferrari et al. (2009), are shown in table 4.1 (note that in Ferrari et al. the Damköhler number for the OSP particle is defined by $Da_{OSP} = R k_P / D_p = \Phi_p$). These indicate the validity of the shrinking core model for much of the practical range of physical parameters. However, as it will be discussed in the next sections, the specific form of equation 4.4 is only required for the derivation of the intermediate times regime, and variations of equation 4.4 can be easily included in the model.

Equation 4.5 can be expressed in terms of the concentration of reactive sites n, which is proportional to the particle volume according to the relationship $n/n_0 = V/V_0 = a^3/R^3$, where n_0 is the initial concentration of reactive sites, V_0 is the initial scavenger particle volume and V is the volume of the unreacted core. Thus, the scavenger site concentration equation and initial condition are given by

$$\frac{\partial n}{\partial t} = -\frac{\hat{v}\, k_p A C_p}{V_0} = -\hat{v}\,\frac{3k_p}{R}\,\frac{C_m}{H}\,\frac{\left(n/n_0\right)^{2/3}}{1+\Phi_p\left(\left(n/n_0\right)^{1/3}-\left(n/n_0\right)^{2/3}\right)}, \tag{4.6}$$

$$\text{I.C.:}\quad n(t=0) = n_0, \tag{4.7}$$

where $A = 4\pi a^2$ is the particle surface area at the moving front, $V_0 = 4\pi R^3/3$ is the initial volume of the particle and $\Phi_p = Rk_P/D_P$ is the Thiele modulus for the particle, expressed in terms of the effective reactive rate constant k_p. Equations similar to equation 4.6 can be derived for shapes other than spheres and are listed in table 4.2.

Table 4.1: Sample calculations for OSP particles and blend for range of parameters used in Ferrari et al. (2009).

	k_p (cm/s)	D_p (cm^2/s)	R (μm)	L_{rxn} (μm)	Φ_p (ND)	Φ_b (ND)
Base case	8x10^{-5}	2x10^{-9}	2.5	0.25	10	104
Highest k_p	1x10^{-3}	2x10^{-9}	2.5	0.02	125	367
Low k_p	1x10^{-6}	2x10^{-9}	2.5	20	0.1	12
High D_p	8x10^{-5}	2x10^{-8}	2.5	2.5	1	104
Low D_p	8x10^{-5}	2x10^{-10}	2.5	0.03	100	104
High R	8x10^{-5}	2x10^{-9}	5.0	0.25	20	73
Low R	8x10^{-5}	2x10^{-9}	0.5	0.25	2	231

$L_{rxn} = D_p/k_p$, $\Phi_p = Rk_P/D_P$, $\Phi_b = \sqrt{3\phi k_p L^2/D_m R H}$,

where D_m = 5.6x10^{-9} cm^2/s, H = 1 and L = 250 μm for all cases above

Table 4.2: Reactive sites material balance for various particle models*.

	Shrinking Core, $\Phi_p \gg 1$	**Homogeneous,** $\Phi_p \ll 1$
Sphere	$\tau = V_0/A_0 k_p$, $V_0/A_0 = R/3$	$\tau = 1/k_R\, n_0$
	$f\left(n/n_0\right) = \dfrac{\left(n/n_0\right)^{2/3}}{1+\Phi_p\left(\left(n/n_0\right)^{1/3} - \left(n/n_0\right)^{2/3}\right)}$	$f\left(n/n_0\right) = \dfrac{n}{n_0}$
Cylinder	$\tau = V_0/A_0 k_p$, $V_0/A_0 \cong R/2$	$\tau = 1/k_R\, n_0$
$h_0 >> R$	$f\left(n/n_0\right) = \dfrac{\left(n/n_0\right)^{1/2}}{1+\Phi_p\left(n/n_0\right)^{1/2}\ln\left(\left(n/n_0\right)^{-1/2}\right)}$	$f\left(n/n_0\right) = \dfrac{n}{n_0}$
Disk	$\tau = V_0/A_0 k_p$, $V_0/A_0 \cong h_0/2$	$\tau = 1/k_R\, n_0$
$h_0 << R$	$f\left(n/n_0\right) = \dfrac{1}{1+\Phi_p\left(1-n/n_0\right)}$	$f\left(n/n_0\right) = \dfrac{n}{n_0}$
$k_p = \sqrt{D_p\, k_R n_0}$, $\Phi_p = Rk_p/D_p = \sqrt{R^2 k_R\, n_0/D_p}$		

* Scavenger material balance is given by equation 4.12, $\partial n/\partial t = -f\left(n/n_0\right)\hat{\nu} C_m/\tau H$

Reaction is much slower than diffusion

When reaction is much slower than diffusion, i.e., $\Phi_p \ll 1$, then the concentration is uniform within the particle and the reactive sites are consumed uniformly over time (Levenspiel, 1999). Equations 4.1 and 4.2 and the initial conditions reduce to

$$C_p = \frac{C_m}{H}, \tag{4.8}$$

$$\frac{\partial n}{\partial t} = -\hat{\nu}\, k_R \frac{C_m}{H} n\ , \tag{4.9}$$

$$\text{I.C.:}\quad n\left(t=0\right) = n_0\,. \tag{4.10}$$

4.2.3 Transport in the film

Here a model of the transport in the film of the blend is developed based on the particle-scale reaction of oxygen with the scavengers. A schematic of the polymer blend of reactive particles imbedded in an inert matrix is illustrated in figure 4.1. For packaging applications the upstream side is exposed to an infinite source of oxygen at partial pressure p_{O_2} at time $t = 0$. This source is typically air and the downstream side has vanishing oxygen partial pressure. The oxygen concentration at the gas/polymer interface is assumed to obey Henry's law. The particles are assumed to be uniformly distributed, in large enough numbers and small enough compared to the film thickness that average effective properties can be used. The concentration profile over the film takes into account the oxygen consumption in each particle and the number density of particles in the film. The non-linear transport equations in the reactive blend, along with initial and boundary conditions, are given by

$$\frac{\partial C_m}{\partial t} = D_m \frac{\partial^2 C_m}{\partial x^2} + \frac{\phi}{\hat{v}} \frac{\partial n}{\partial t}, \tag{4.11}$$

$$\frac{\partial n}{\partial t} = -\frac{\hat{v}}{\tau} \frac{C_m}{H} f\left(n/n_0\right), \tag{4.12}$$

$$\text{I.C.:} \quad C_m\left(x, t=0\right) = 0, \quad n\left(x, t=0\right) = n_0, \tag{4.13}$$

$$\text{B.C.:} \quad C_{m,0} \equiv C_m\left(x=0, t\right) = S_m \, p_{O_2}, \quad C_{m,L} \equiv C_m\left(x=L, t\right) = 0. \tag{4.14}$$

where D_m is the oxygen diffusion coefficient of the inert matrix and ϕ is the volume fraction of OSP in polymer blend. The characteristic time τ and the generic function of

reactive sites concentration $f(n/n_0)$ depend on the reactive model chosen for the particle. For spherical particles in the limit of $\Phi_p \gg 1$, $\tau = R/3k_p$ and $f(n/n_0) = (n/n_0)^{2/3} \Big/ \left\{1 + \Phi_p \left[(n/n_0)^{1/3} - (n/n_0)^{2/3} \right]\right\}$, recovering equation 4.6. In the limit of $\Phi_p \ll 1$, $\tau = 1/k_R\, n_0$ and $f(n/n_0) = n/n_0$, recovering equation 4.9. Expressions for τ and $f(n/n_0)$ for the two different models of particle-scale and particle shapes are given in table 4.2. Note that equation 4.12 is the generic form of the material balance for reactive sites, which applies to both the homogeneous (slow reaction) and shrinking core (fast reaction) models of particles of any shape.

The oxygen flux and the total amount of oxygen permeated are quantities of interest derived from the solution of equations 4.11-414. The downstream flux J at time t is given by

$$J\Big|_{x=L} = -D_m \left.\frac{\partial C}{\partial x}\right|_{x=L}, \tag{4.15}$$

and the total oxygen permeated through the membrane Q_t at time t is given by

$$Q_t = \int_0^t J\Big|_{x=L} dt\,. \tag{4.16}$$

Numerical solutions of equations 4.11-4.14 reveal three regimes of interest for the downstream flux (figures 4.2-4.4), as has been shown by Ferrari et al. (2009). The early time regime is characterized by a fast rise of the flux, followed by a flux plateau. This quasi-steady plateau eventually gives way to a second regime of rising oxygen flux. The third regime occurs when all the reactive sites have been consumed, and the flux reaches

its final steady-state value. Note that the characteristic times for each regime is independent of Φ_p, as shown in figures 4.2-4.4.

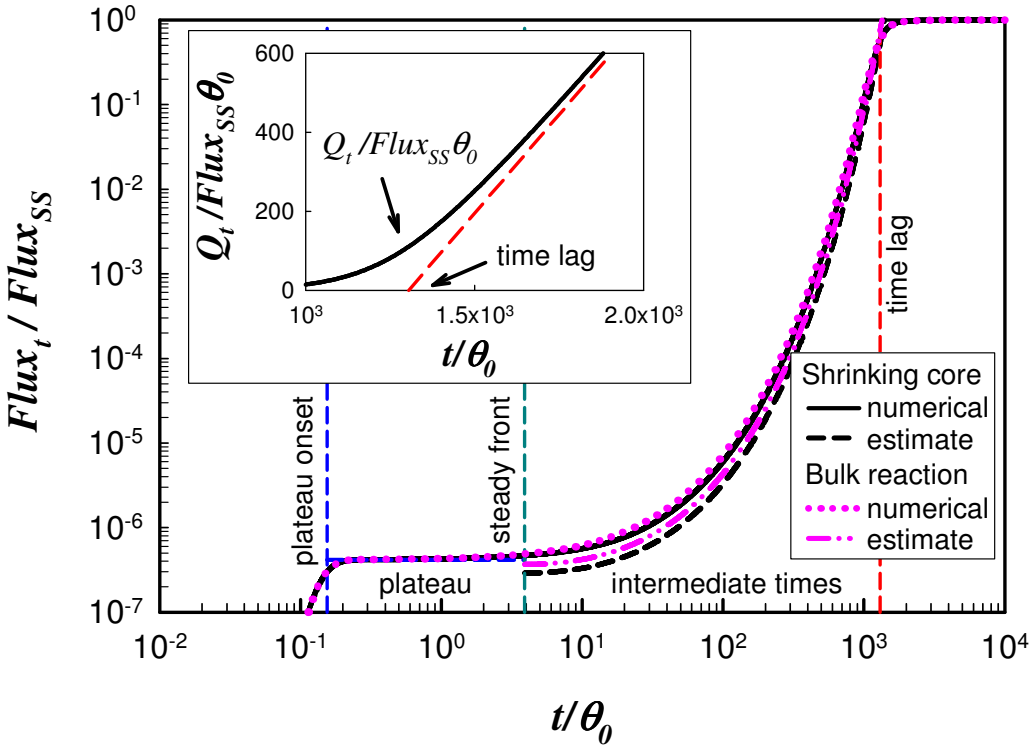

Figure 4.2: Comparison of numerical solution and analytical estimates for the three regimes relevant to analysis of dimensionless downstream oxygen flux for $\nu = 0.0023$, $\Phi_b = 18$ and $\Phi_p = 0.125$. Solutions based on shrinking core particle model (solid line = numerical solution, dashed line = prediction) and the bulk reaction particle model (dotted line = numerical solution, dash-dot = prediction) are compared. The initial flux plateau (horizontal dashed line) is the same for both models and matches closely the numerical solution. Inset shows the time lag as determined from the numerical solution, using the asymptote as $Q_{t\to\infty}$.

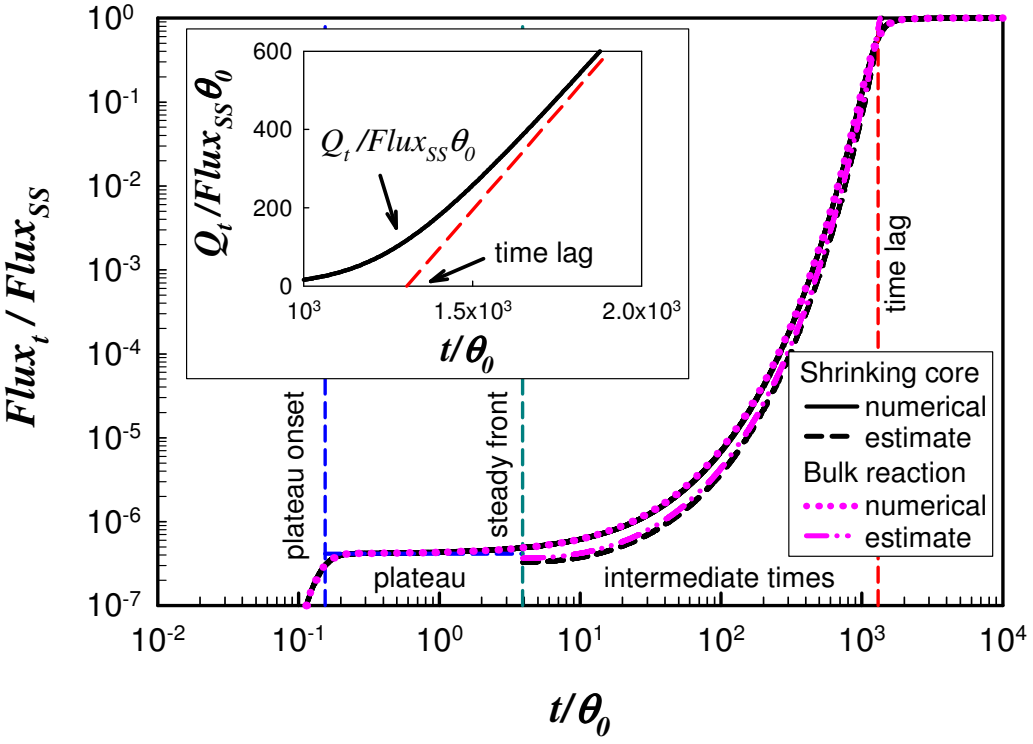

Figure 4.3: Comparison of numerical solution and analytical estimates for the three regimes relevant to analysis of dimensionless downstream oxygen flux for $\nu = 0.0023$, $\Phi_b = 18$ and $\Phi_p = 1.25$. Solutions based on shrinking core particle model (solid line = numerical solution, dashed line = prediction) and the bulk reaction particle model (dotted line = numerical solution, dash-dot = prediction) are compared. The initial flux plateau (horizontal dashed line) is the same for both models and matches closely the numerical solution. Inset shows the time lag as determined from the numerical solution, using the asymptote as $Q_{t\to\infty}$.

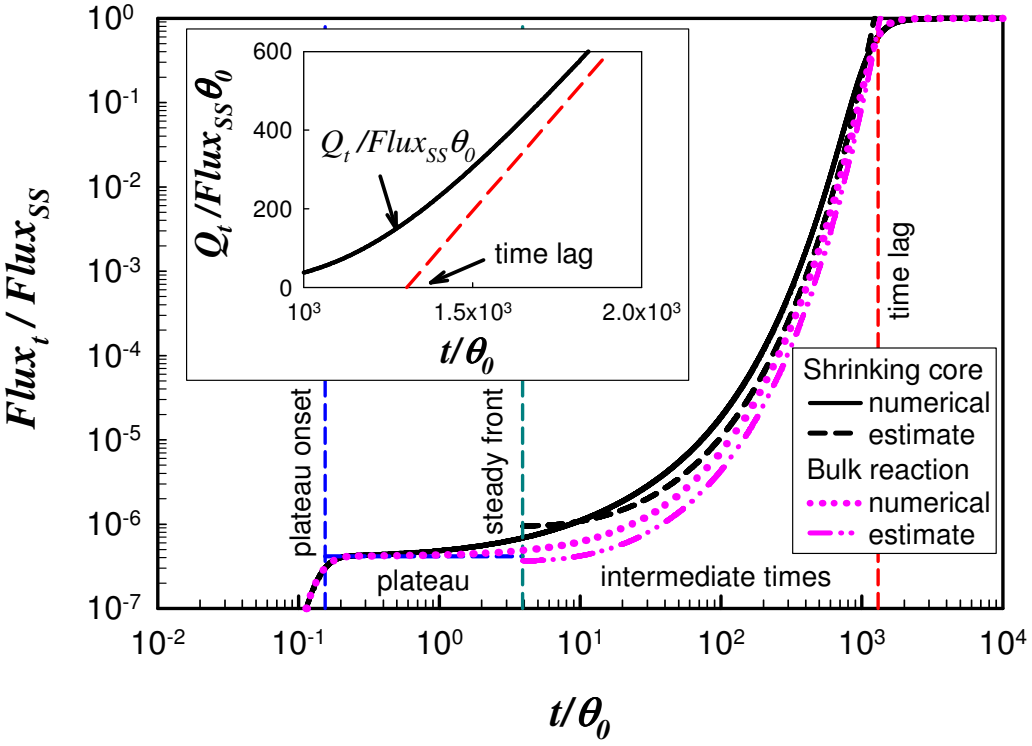

Figure 4.4: Comparison of numerical solution and analytical estimates for the three regimes relevant to analysis of dimensionless downstream oxygen flux for $\nu = 0.0023$, $\Phi_b = 18$ and $\Phi_p = 12.5$. Solutions based on shrinking core particle model (solid line = numerical solution, dashed line = prediction) and the bulk reaction particle model (dotted line = numerical solution, dash-dot = prediction) are compared. The initial flux plateau (horizontal dashed line) is the same for both models and matches closely the numerical solution. Inset shows the time lag as determined from the numerical solution, using the asymptote as $Q_{t\to\infty}$.

The regimes observed in the transient downstream flux can be mapped to the concentration profiles, as illustrated in figure 4.5. The early time regime occurs before significant consumption of reactive sites. Most sites are still available, except for the region very close to the upstream boundary. The uptake of oxygen in this regime can be approximated by a simpler first-order reaction, as will be discussed in the next section.

For intermediate times, the concentration profiles can be divided into three zones. The first zone is predominantly diffusive, characterized by a linear oxygen concentration profile, with all the reactive sites consumed. The second zone shows a non-linear decay in the oxygen concentration due to reaction, coupled with a gradual change in reactive sites concentration. In the third zone, most reactive sites are still available, and the oxygen concentration is vanishingly small, which is consistent with the downstream boundary condition. A moving front develops during this regime, leading to the analysis described in the Supplemental Material section (at the end of this chapter) to develop predictive equations for this regime. Note that this is a front moving through the film and not to be confused with the moving front within the reactive particle illustrated in figure 4.1. Finally, the third regime occurs when all the reactive sites have been consumed, and the concentration profile becomes linear over the whole film. This regime is characterized by the time lag, when the flux approaches its steady-state value.

The three regimes illustrated in figures 4.2- 4.5 are observed for reactive transport in reactive polymer blends as well as homogeneous reactive membranes. The analytical solutions for these three regimes are derived for polymer blends in the next sections, following the framework described in Carranza et al. (2010). Table 4.3 summarizes the approximate times for each time region in terms of the physical parameters of polymer blends for oxygen scavenging. Similar analysis could be extended to blends targeting other species, e.g. water, by modifying the scavenging behavior accordingly.

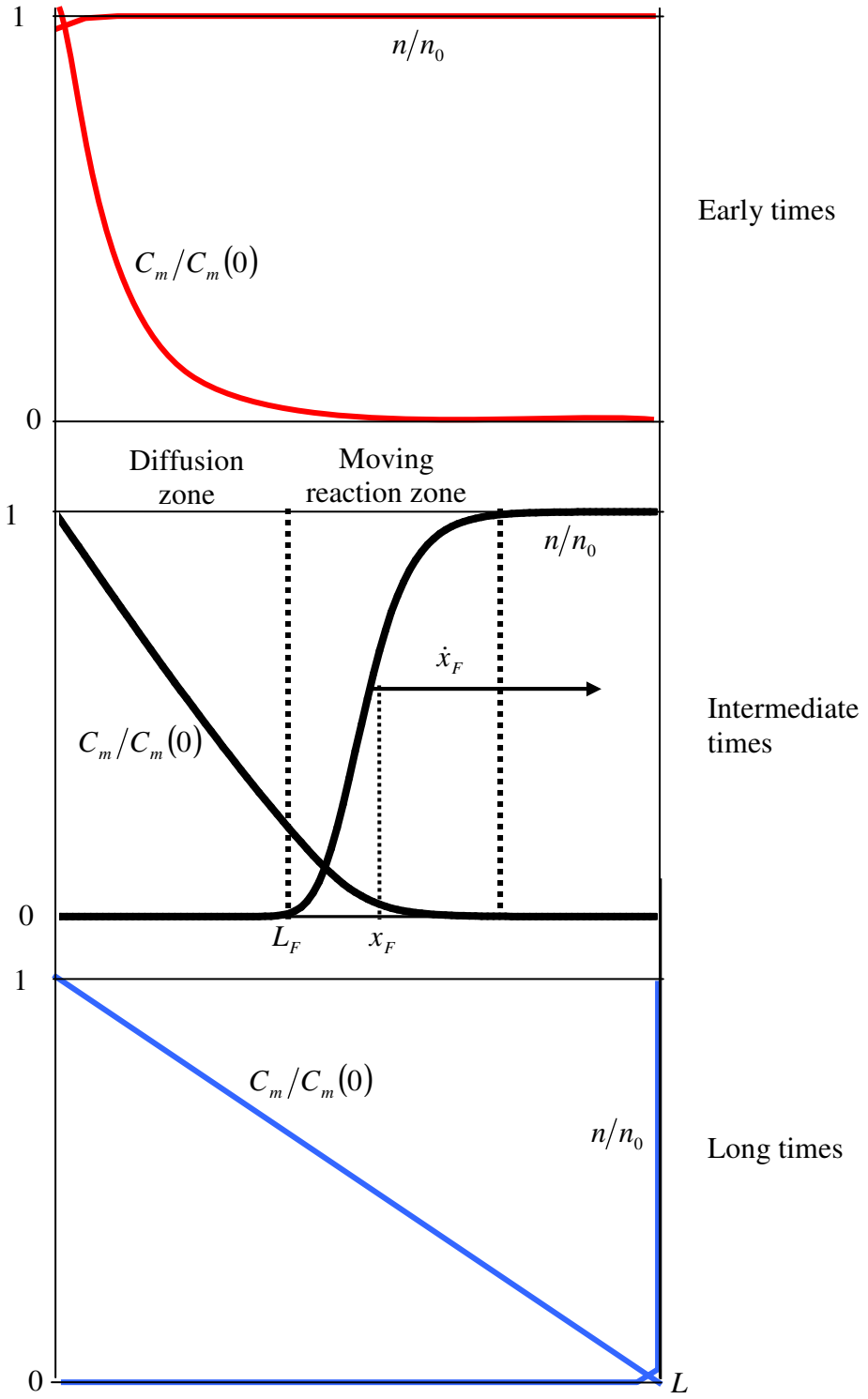

Figure 4.5: Concentration profiles for early, intermediate and long times.

Table 4.3: Analytical predictions of dimensionless flux for early, intermediate and long times for a reactive polymer blend.

Time interval	**Dimensional equations**
Early times*	$J\big\|_{x=L} = 2J_{SS}\Phi_b\, e^{-\Phi_b}$
$t_{onset} \le t \le t_{SF}$	$t_{onset} = \tau\left(\Phi_b - 1\right) H/2\phi$
Intermediate times	$J\big\|_{x=L} = bJ_{SS}\left(L/x_F\right)e^{-\Phi_b(1-x_F/L)},\ x_F = \sqrt{2\nu D_m t}$
$t_{SF} \le t \le \theta$	$t_{SF} = H\tau/2\nu\phi$
Long times	$J\big\|_{x=L} \to J_{SS} = C_{m,0}D_m/L$
$t > \theta$	$\theta = \theta_0(1+3/\nu)$
$\Phi_b = \sqrt{\phi L^2/D_m\tau H}$, $\Phi_p = \sqrt{R^2k_R\, n_0/D_p}$, $\nu = \hat{v}\, C_{m,0}/\phi n_0$, $\theta_0 = L^2/6D_m$	
$\tau = 1/k_R\, n_0$ for $\Phi_p \ll 1$, $\tau = V_0/A_0k_p$ for $\Phi_p \gg 1$	
* $J\big\|_{x=L} \cong 0$ for $t < t_{onset}$	

4.3 ANALYSIS OF EARLY TIMES TO ESTIMATE INITIAL LEAKAGE FLUX PLATEAU

At early times, most of the scavenger sites remain unreacted, except those very close to the upstream boundary, as illustrated in figure 4.5. Therefore, the concentration of reactive sites n can be approximated by the initial concentration of reactive sites n_0. The oxygen flux in the plateau region of interest is also quasi-steady, and thus, the oxygen transport equation and boundary conditions become

$$\frac{d^2C_m}{dx^2} - \frac{\phi}{\tau}\frac{C_m}{H} = 0, \tag{4.17}$$

$$\text{B.C.:}\quad C_{m,0} \equiv C_m\left(x=0,t\right) = S_m\ p_{O_2},\quad C_{m,L} \equiv C_m\left(x=L,t\right) = 0. \tag{4.18}$$

This equation, along with the boundary conditions can be easily solved to show that

$$C_m = -C_{m,0}\frac{\cosh(\alpha L)}{\sinh(\alpha L)}\sinh(\alpha x) + C_{m,0}\cosh(\alpha x), \tag{4.19}$$

where $\alpha = \sqrt{\phi/\tau H}$. Using equation 4.15 for the downstream flux with equation 4.19 for oxygen concentration gives the following expression for the flux:

$$J\big|_{x=L} = \alpha L J_{SS}/\sinh(\alpha L), \text{ or } J\big|_{x=L} \sim 2\alpha L J_{SS}\, e^{-\alpha L} \text{ for } \alpha L \gg 1, \tag{4.20}$$

where J_{SS} is the steady-state oxygen flux $Flux_{SS} = J_{SS} = C_{m,0}D_m/L$. Solovyov and Goldman (2005b) derived a similar equation for the flux to describe a system with a large excess of reactive sites, as part of their modified moving front model. Here this model is used to describe the flux in the early time regime.

This equation can be expressed in terms of the effective Thiele modulus for the film of the polymer blend $\Phi_b = \sqrt{\phi L^2/D_m H\tau}$, i.e. the ratio of the length scale of diffusion through the film and the length scale of reaction within the particle so that

$$Flux_{plat} = J\big|_{x=L} = 2J_{SS}\Phi_b\, e^{-\Phi_b}, \tag{4.21}$$

which is valid for $\Phi_b \gg 1$. This algebraic expression predicts the initial flux plateau using physical properties that can be measured experimentally. Note that in the limit of $\Phi_p \ll 1$, $\tau = 1/k_R n_0$ as shown in table 4.2, thus making equation 4.21 independent of particle shape or surface area. In the limit of $\Phi_p \gg 1$, $\tau = V_0/A_0 k_p$ in general again regardless of particle shape as shown in table 4.2, and thus $\Phi_b = \sqrt{\phi A_0 k_p L^2/V_0 D_m H}$. Therefore, the flux given by equation 4.21 is independent of particle shape and depends

only on the specific area A_0/V_0 in the limit of $\Phi_p \gg 1$. In systems where particle shape cannot be described by simple geometries, A_0/V_0 can be determined by analyzing images, e.g., by transmission electron microscopy, using the principles of stereology (Thomas and Goringe 1979; Russ and Dehoff 2000). Equation 4.21 is identical in functional form in the limit of fast and slow reactions within the particles. Indeed the existence of the quasi-steady plateau flux is independent of the details of the reaction within the particle because at early times all the scavenging sites are essentially accessible.

The initial plateau estimate of equation 4.21 was compared to the values obtained by numerical solutions of the polymer blend model equations and boundary conditions given by equations 4.11-4.14 for both fast and slow reactions. The prediction is in excellent agreement with the numerical solutions for all the cases computed, as illustrated in figures 4.2-4.4 and the parity plot of figure 4.6. The plateau flux decreases with increasing $\Phi_b = \sqrt{\phi L^2/D_m H \tau}$, as illustrated in figure 4.7. The plateau flux is proportional to the steady-state flux $J_{SS} = C_{m,0} D_m / L$, and consequently to the upstream oxygen concentration $C_{m,0}$. Increasing D_m increases J_{SS} and decreases Φ_b, leading to an increase in the initial flux plateau. Conversely, increasing L decreases J_{SS} and increases Φ_b, leading to a decrease in the initial flux plateau.

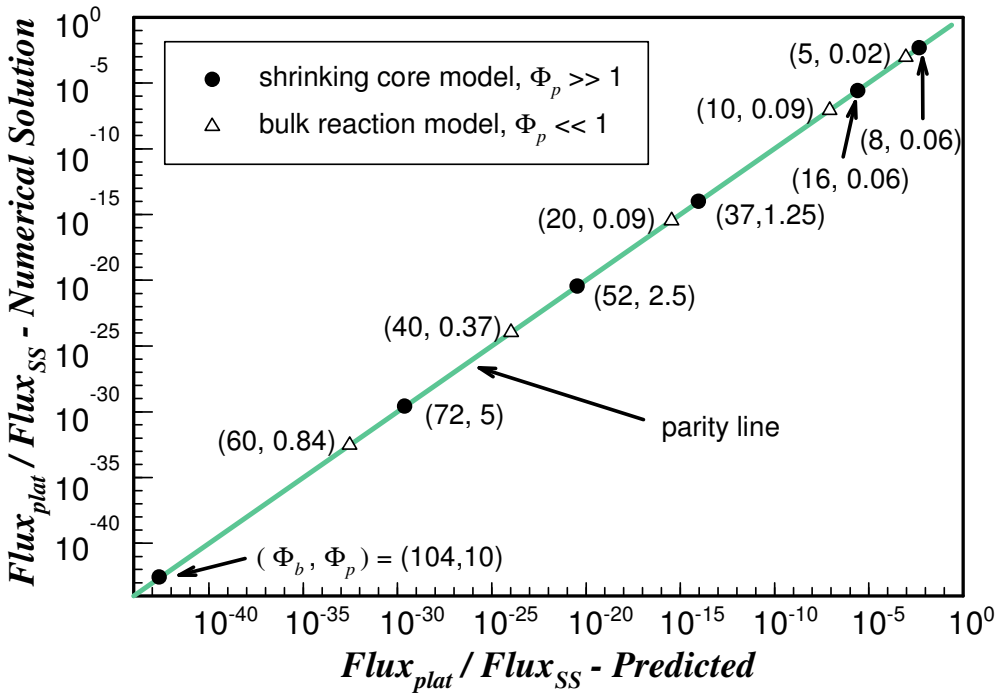

Figure 4.6: Parity chart for flux plateau comparing numerical solution and analytical prediction for various Φ_b and Φ_p. The values in parenthesis give Φ_b and Φ_p, respectively, for each data point.

The increase in the flux due to increasing $C_{m,0}$ or D_m is expected, since the former causes more oxygen to be available, while the later enables fast transport of oxygen through the film, which leads to greater leakage through the film. Likewise, the decrease due to higher L is also expected, since for thicker films, the diffusion time is longer, allowing the reaction to occur and, thus, reducing the amount of oxygen breakthrough at early times.

The onset of the initial plateau t_{onset} can be derived by recognizing that the transient can be modeled as an unsteady first-order reaction diffusion problem. This t_{onset}

is the time lag for an equivalent first-order reactive membrane, given by Carranza et al. (2010);

$$t_{onset} = \tau \frac{\Phi_b \coth(\Phi_b) - 1}{2\,\phi/H}, \text{ or } t_{onset} \cong \tau \frac{\Phi_b - 1}{2\,\phi/H} \text{ for } \Phi_b \gg 1. \tag{4.22}$$

Note that the second approximate expression for the onset time retains the constant 1 in the numerator because it is found to be a good approximation for Φ_b as low as 2 or 3.

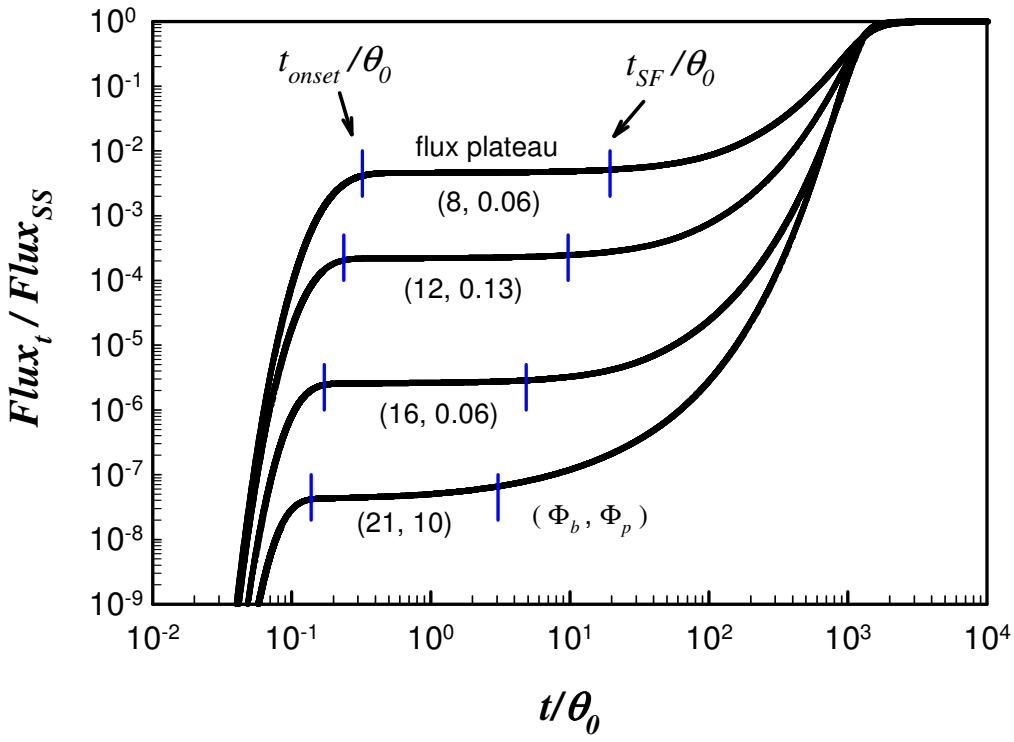

Figure 4.7: Dimensionless downstream oxygen flux for $\nu = 0.0023$ and various Φ_b and Φ_p. The values in parenthesis give Φ_b and Φ_p, respectively, for each case. The plateau flux increases with decreasing Φ_b, as predicted by equation 4.21. The initial plateau region is bound by the plateau onset t_{onset} and t_{SF}, as predicted by equations4.22 and 4.23, respectively.

The initial plateau regime eventually transitions to a fast rise in the downstream oxygen flux, in a transient regime described in the next section. The transition between these two regimes occurs at t_{SF}, the time a steady front has been established. Following the steps in Carranza et al. (2010), this time can be estimated by comparing the consumption of reactive sites within the front volume with the influx of oxygen into the front volume, and is given by

$$t_{SF} = \tau \frac{H}{2\nu\phi}, \tag{4.23}$$

where $\nu = \hat{\nu} C_{m,0} / \phi n_0$ is the ratio between dissolved oxygen and reactive capacity. When the onset of the initial plateau $t_{onset} = t_{SF}\, \nu \left(\Phi_b - 1\right)$ occurs before the steady front has been established, i.e., $0 < \nu \left(\Phi_b - 1\right) < 1$, there is a well defined initial plateau regime as the cases shown in figure 4.7, and the transient flux approximation described in the next section is valid.

4.4 TRANSIENT FLUX REGIME AT INTERMEDIATE TIMES

To determine the transient flux the specific shape of the particle and the assumed reaction model as embodied by $f\left(n/n_0\right)$ must be known. For spherical particles in the limit of $\Phi_p \gg 1$, the concentration equations are given by

$$\frac{\partial C_m}{\partial t} = D_m \frac{\partial^2 C_m}{\partial x^2} - \frac{3k_p\phi}{R} \frac{C_m}{H} \frac{\left(n/n_0\right)^{2/3}}{1 + \Phi_p \left[\left(n/n_0\right)^{1/3} - \left(n/n_0\right)^{2/3}\right]}, \tag{4.24}$$

$$\frac{\partial n}{\partial t} = -\hat{v}\,\frac{3k_p}{R}\,\frac{C_m}{H}\,\frac{\left(n/n_0\right)^{2/3}}{1+\Phi_p\left[\left(n/n_0\right)^{1/3}-\left(n/n_0\right)^{2/3}\right]}. \tag{4.25}$$

Solutions in the frame of reference of the moving reaction zone were developed, as shown in the Supplemental Material section at the end of this chapter, giving the algebraic expression for the downstream flux:

$$J\big|_{x=L} = bJ_{SS}\,\frac{\left(L/x_F\right)}{e^{\Phi_b(1-x_F/L)}}, \tag{4.26}$$

where $J_{SS} = C_{m,0}D_m/L$ is the steady-state oxygen flux and $x_F = \sqrt{2\nu D_m t}$ is the position of the moving front. Values of b in equation 4.26, which are listed in table 4.4 for spherical particles and various values of Φ_p, are computed by numerical solutions of the moving front ODEs, as discussed in the Supplemental Material section. Note that the functional form of equation 4.26 is valid for a wide range of models, with specific values of b computed for each different model. In the limit of $\Phi_p \ll 1$ the transient result for the homogenous film is recovered where b = 0.653 (Carranza et al. 2010). Figures 4.2-4.4 compare the numerical solution to the predicted values of the initial flux plateau (equation 4.21) and the intermediate transient flux (equation 4.26) using the shrinking core particle model (equations 4.24 and 4.25) and the bulk reaction particle model (equations 4.11 and 4.12 where $\tau = 1/k_R\,n_0$ and $f\left(n/n_0\right) = n/n_0$). The graphs show the results for $\Phi_p = 0.125$, $\Phi_p = 1.25$ and $\Phi_p = 12.5$, where $\nu = 0.0023$ and $\Phi_b = 18$ for all cases. Note that the results for the shrinking core particle model and the bulk reaction

particle model are nearly identical for $\Phi_p = 0.125$ and $\Phi_p = 1.25$, therefore both models can be used in this range of Φ_p.

Table 4.4: Values of b in equation 4.26 for flux estimate for blends of spherical particles with various Φ_p.

$\Phi_p = R\,k_P / D_P = \left(R^2 k_R\, n_0 / D_p\right)^{1/2}$	b
Homogeneous film	0.653
0.1	0.514
1	0.581
10	1.54
100	335

As indicated in table 4.3, the transient flux prediction of equation 4.26 is valid between the time a steady front has been established (t_{SF} given by equation 4.23) to the time before the front has reached the right boundary, i.e. when most of the reactive sites have been consumed. Note that for larger Φ_p (figure 4.4) the flux increase from the initial plateau flux starts before t_{SF}, resulting in a larger deviation from the predicted values.

4.5 STEADY-STATE ANALYSIS TO PREDICT TIME LAG

The time lag for the blend film modeled in this chapter can be predicted analytically by adapting the asymptotic analysis developed by Frisch (1957) for diffusion time lag, and more recently employed by Siegel and Cussler (2004) for prediction in

reactive membrane films. The reactive term in equation 4.11 for oxygen concentration can be expressed in terms of the change in reactive sites, given by equation 4.12, thus resulting in a single equation,

$$\frac{\partial C_m}{\partial t} = D_m \frac{\partial^2 C_m}{\partial x^2} + \frac{\phi}{\hat{v}} \frac{\partial n}{\partial t} . \tag{4.27}$$

Equation 4.27 is integrated from an arbitrary position x along the film to L:

$$\int_x^L \left(\frac{\partial C_m}{\partial t} - \frac{\phi}{\hat{v}} \frac{\partial n}{\partial t} \right) dy = D_m \left. \frac{\partial C_m}{\partial x} \right|_{x=L} - D_m \frac{\partial C_m}{\partial x} . \tag{4.28}$$

Integrating again in space, now from 0 to L, and using the downstream oxygen flux defined in equation 4.15 gives

$$\int_0^L \int_x^L \left(\frac{\partial C_m}{\partial t} - \frac{\phi}{\hat{v}} \frac{\partial n}{\partial t} \right) dy dx = -J\big|_{x=L} \int_0^L dx - D_m \int_0^L \frac{\partial C_m}{\partial x} dx . \tag{4.29}$$

Simplifying the double integral to a single integral, by reversal of the integration order, and evaluating the right hand side, equation 4.29 becomes

$$\int_0^L x \left(\frac{\partial C_m}{\partial t} - \frac{\phi}{\hat{v}} \frac{\partial n}{\partial t} \right) dx = -L\, J\big|_{x=L} + D_m C_{m,0} . \tag{4.30}$$

Integrating equation 4.30 from 0 to time t gives

$$\int_0^t \int_0^L x \left(\frac{\partial C_m}{\partial t} - \frac{\phi}{\hat{v}} \frac{\partial n}{\partial t} \right) dx dt = -L \int_0^t J\big|_{x=L}\, dt + D_m C_{m,0} \int_0^t dt . \tag{4.31}$$

For very long times, the film achieves steady state making the oxygen concentration profile linear and the concentration of reactive sites, n, approaches 0, except at the downstream boundary. Using the cumulative oxygen permeate defined in equation 4.16 and evaluating each term at steady state, equation 4.31 becomes

$$\frac{L^2}{6D_m}+\frac{\phi n_0 L^2}{2\hat{\nu}C_{m,0}D_m}=-\frac{LQ_t}{C_{m,0}D_m}+t\,. \tag{4.32}$$

The time lag is determined by finding the point where the steady state asymptote of the cumulative permeate crosses the time axis, i.e., by setting $Q_{t,ss}=0$ in equation 4.32 to get

$$\theta=\theta_0\left(1+3/\nu\right), \tag{4.33}$$

where $\theta_0=L^2/6D_m$ is the diffusion time lag of the inert matrix and $\nu=\hat{\nu}C_{m,0}/\phi n_0$ is the ratio between dissolved oxygen and reactive capacity. Since equation 4.33 was obtained based on the generic equations 4.11 and 4.12, it is valid irrespective of the shapes or sizes of the particles, and irrespective of the specific reaction mechanism within the particles. Note that the time lag depends only on the diffusion time scale through the inert matrix, and the ratio between dissolved oxygen and scavenging capacity of the blend.

4.6 FIGURES OF MERIT BASED ON TRANSIENT BEHAVIOR

The cumulative oxygen permeate Q_t is obtained by the integration of the downstream flux, per equation 4.16, and can be estimated analytically by adding the contributions from the initial plateau regime, see equation 4.21, and the transient regime, see equation 4.26. Thus, the oxygen permeate can be estimated by

$$Q_t=\int_{t_{onset}}^{t_{SF}} J\big|_{x=L}dt+\int_{t_{SF}}^{t} J\big|_{x=L}dt=\frac{2J_{SS}t_{SF}\Phi_b}{e^{\Phi_b}}\left[1+\nu\left(1-\Phi_b\right)+b\left(e^{\sqrt{t/t_{SF}}}-e\right)\right]. \tag{4.34}$$

For times below t_{SF}, the above equation reduces to the first integral, $2J_{SS}\Phi_b\,e^{-\Phi_b}\left[t+t_{SF}\nu\left(1-\Phi_b\right)\right]$, which is the initial flux plateau multiplied by $t-t_{onset}$.

The kill time t_K, i.e., the time when the oxygen permeate reaches a predefined max $Q_{\max}$, proposed as a transient parameter by Nuxoll and Cussler (2005), can be found by solving equation 4.34 for time, giving

$$t_k = t_{SF} \ln^2 \left[\frac{Q_{\max} e^{\Phi_b}}{2bJ_{SS}t_{SF}\Phi_b} - \frac{1+\nu\left(1-\Phi_b\right)}{b} + e \right]. \tag{4.35}$$

4.7 SUMMARY AND CONCLUSIONS

The transport equations for a mobile permeate in a blend of reactive particles in an inert matrix have been derived to describe reactive particles of any shape in the limits of fast reaction and slow reaction. The framework developed to derive analytical design formulae for homogeneous reactive membranes (Carranza et al. 2010) has been extended to these reactive polymer blends, illustrating how the approach can be adapted for models with very distinct reactive terms. Equations for flux and characteristic times for the three regimes identified in the numerical solutions have been derived for the polymer blend. It was found that the details of the reaction mechanism within the particles do not affect the functional form of the analytic models and only affect the values of known or easily determined constants in the predictive equations. The technique presented is broadly applicable and can be easily adapted to accommodate other particle-scale reaction models.

For the initial regime, when most reactive particles are still available, the initial plateau flux and plateau onset time t_{onset} can be determined without knowledge of particle shapes, using instead the average area to volume ratio of the reactive particles A_0/V_0, which can be determined by analyzing images using the principles of stereology.

Likewise, the characteristic time for the intermediate regime t_{SF}, which marks the end of the initial flux plateau, requires only knowledge of A_0/V_0. One of the critical conclusions of this chapter is the generality of equation 4.21 for the prediction of this flux. For many packaging applications, the initial plateau flux is the important design consideration because it characterizes the small but persistent leakage of oxygen through the barrier. Furthermore, the calculations for early times do not require the knowledge of the reaction details within the particle. The value of the downstream flux for intermediate times can be predicted analytically if the particle shape is known. The third regime, when most particles have been consumed, is characterized by the time lag θ and the steady-state flux, which are completely independent of particle shape, area to volume ratios, or details of reaction within each particle.

Traditionally, the time lag, which is independent of reaction rate, has been considered the figure of merit when designing reactive membranes, as it marks the exhaustion of the reactive particles. However, this study suggests that the value of the initial flux plateau, which accounts for both diffusion and reaction rates, along with its end time t_{SF} are additional parameters to consider when designing packaging materials. For applications where it may be preferable to design a barrier which will remain in the plateau region throughout the life of the product, the end of the useful life may be determined by the beginning of the transient region t_{SF} instead of time lag θ, and the value of the flux plateau can be used to determine the total permeate over the life of the product.

SUPPLEMENTAL MATERIAL – 4.A

Following Carranza et al. (2010), solutions in the frame of reference of the moving reaction zone were developed, with solutions of the form

$$n(x,t)/n_0 = \eta(\xi), \tag{4.A.1}$$

$$C(x,t) = C_{m,0}\sqrt{H\tau/t\phi}\, G(\xi), \tag{4.A.2}$$

$$\xi = \left[x - x_F(t)\right]\Big/\sqrt{D_m H\tau/\phi}, \tag{4.A.3}$$

where $\eta(\xi)$ represents the reactive site in the new frame of reference, $G(\xi)$ is the self-similar oxygen concentration field, $H\tau/\phi$ is the reactive time scale for the blend, $\sqrt{D_m H\tau/\phi}$ is the reactive length scale for the blend. The position of the moving front is given by

$$x_F = \sqrt{2\nu D_m t}, \tag{4.A.4}$$

where $\nu = \hat{\nu} C_{m,0}/\phi n_0$ is the ratio between dissolved oxygen and reactive capacity. The leading order equations for the polymer blend become

$$\frac{d^2\hat{G}}{d\xi^2} - \hat{G} f(\eta) = 0, \tag{4.A.5}$$

$$\frac{d\eta}{d\xi} - \hat{G} f(\eta) = 0, \tag{4.A.6}$$

$$\text{B.C.:}\quad \eta(\infty) = 1, \quad \hat{G}(\infty) = 0, \quad \left.\frac{d\hat{G}}{d\xi}\right|_{-\infty} = -1, \tag{4.A.7}$$

where $\hat{G} = \sqrt{2\nu}\, G$.

Provided that $f(\eta) \to 1$ as $\xi \to \infty$, the asymptotic solutions of these equations as $\xi \to \infty$ are given by

$$\hat{G} = be^{-\xi}, \quad \eta = 1 - be^{-\xi}. \tag{4.A.8}$$

Thus, substituting equation 4.A.8 in equation 4.A.2 for concentration in the moving front regime and using equation 4.15 for flux gives equation 4.26, the algebraic expression for the downstream flux. Note that equation 4.26 functional form is valid for any model with the asymptote $f(\eta) \to 1$ as $\xi \to \infty$, regardless of the details of $f(\eta)$. If $f(\eta)$ is known, the values of b may be computed by solving equations 4.A.5 and 4.A.6 by the shooting method using equation 4.A.8 as the initial conditions while varying b until the condition for matching the asymptotic solutions of the diffusion zone and the moving reaction zone is satisfied, i.e., $\hat{G}(\xi) = -\xi$ as $\xi \to -\infty$ (Carranza et al. 2010).

Nomenclature

a radius of the reactive core, cm

A area of scavenging core, cm^2

A_0 area of scavenging particle, cm^2

b constant for moving front flux prediction, dimensionless

C_m O_2 concentration in the film, mol_{O2}/cm^3

$C_{m,0}$ oxygen concentration at the polymer blend film upstream surface $C_{m,0} = p_{O_2} S_m$, mol_{O2}/cm^3

C_p oxygen concentration in the OSP particle, mol_{O2}/cm^3 OSP

D_m oxygen diffusion coefficient of the inert matrix, cm^2/s

D_p oxygen diffusion coefficient for the oxidized OSP, cm^2/s

$f(n/n_0)$ reactive sites consumption function for a particle, dimensionless

G variable for moving front analysis, dimensionless

$\hat{G} = \sqrt{2\nu}\, G$

H partition coefficient, $H = S_m / S_p$, dimensionless

J oxygen flux, mol/cm^2 s

k_p reaction rate constant for reactive particle, cm/s

k_R bulk reaction rate constant for reactive particle, cm^3 OSP/mol_{RS} s

L thickness of the film, cm

n concentration of reactive sites, mol_{RS}/cm^3

n_0 initial concentration of reactive sites, mol_{RS}/cm^3

p_{O_2} oxygen partial pressure, MPa

Q_t oxygen permeate, mol/cm^2

R radius of the OSP particle, cm

S_m solubility coefficient for oxygen in inert matrix, $cm^3(STP)/cm^3$ MPa

S_p solubility coefficient for oxygen in the scavenging polymer, $cm^3(STP)/cm^3$ MPa

t time, s

t_K kill time, s

t_{onset} onset time for the initial flux plateau, s

t_{SF} time when a steady moving front is established, s

V volume of reactive core, cm^3

V_0 volume of scavenging particle, cm^3

x position along film thickness, cm

x_F moving front position, cm

$\dot{x}_F$ moving front speed, cm/s

~ denotes dimensionless variables

Greek letters

β OSP capacity, $\beta = n_0/\hat{v}$, mol_{O2}/cm^3 OSP

θ time lag, s

θ_0 diffusion time lag of inert polymer, $\theta_0 = L^2/6D_m$, s

ϕ volume fraction of OSP in polymer blend, dimensionless

Φ_b effective Thiele modulus for the blend, $\Phi_b = \sqrt{\phi L^2/D_m \tau H}$, dimensionless

Φ_p Thiele modulus for the OSP particle, $\Phi_p = \sqrt{R^2 k_R n_0/D_p}$ or $\Phi_p = Rk_p/D_p$, dimensionless

η reactive sites expressed in terms of moving front coordinate, dimensionless

ν ratio between dissolved oxygen and reactive capacity, $\nu = \hat{\nu} C_{m,0}/\phi n_0$, dimensionless

$\hat{\nu}$ stoichiometric coefficient, mol_{RS} /mol_{O2}

τ time scale, $\tau = V_0/A_0 k_p$ or $\tau = 1/k_R n_0$, s

ξ moving front coordinate, dimensionless

Chapter 5: Multilayer Reactive Barrier Materials

5.1 INTRODUCTION

Homogeneous reactive barrier films were studied in Chapter 2; reactive polymer blends were studied in Chapters 3 and 4. Here composite membranes consisting of alternating inert and reactive polymer layers are studied. These three reactive barrier configurations are compared in Chapter 6 to aid in the selection of the most suitable configuration for a particular application.

As with previous chapters, the results here will be developed in the context of oxygen scavenging, but in fact they are generally applicable to any reactive permeate and barrier system. For layered systems, in addition to the early time flux plateau and the steady state regimes characterized by time lag described in Chapters 2-4, there are intermediate rises in the transient flux and permeate, corresponding to the number of reactive layers in the composite. Analytical estimates for the initial flux plateau and for the time lag are presented for multilayer films.

5.2 MODEL DESCRIPTION

Consider a film of thickness L consisting of N_M inert matrix layers and N_R reactive (scavenging) layers arranged in an alternating pattern, with a total of $N = N_M + N_R$ layers, as illustrated in figure 5.1. The index i represents each adjacent pair of inert matrix and reactive layers, where the position of the inert matrix layer is given by $x_{2i-2} < x < x_{2i-1}, \quad i = 1, 2, 3..., N_R + 1$ and the position of the reactive layer is

given by $x_{2i-1} < x < x_{2i}, \quad i = 1, 2, 3..., N_R$. The constant thickness of each reactive layer is given by $L_R = x_{2i} - x_{2i-1}$ and the constant thickness of each inert layer is given by $L_M = x_{2i-1} - x_{2i-2}$.

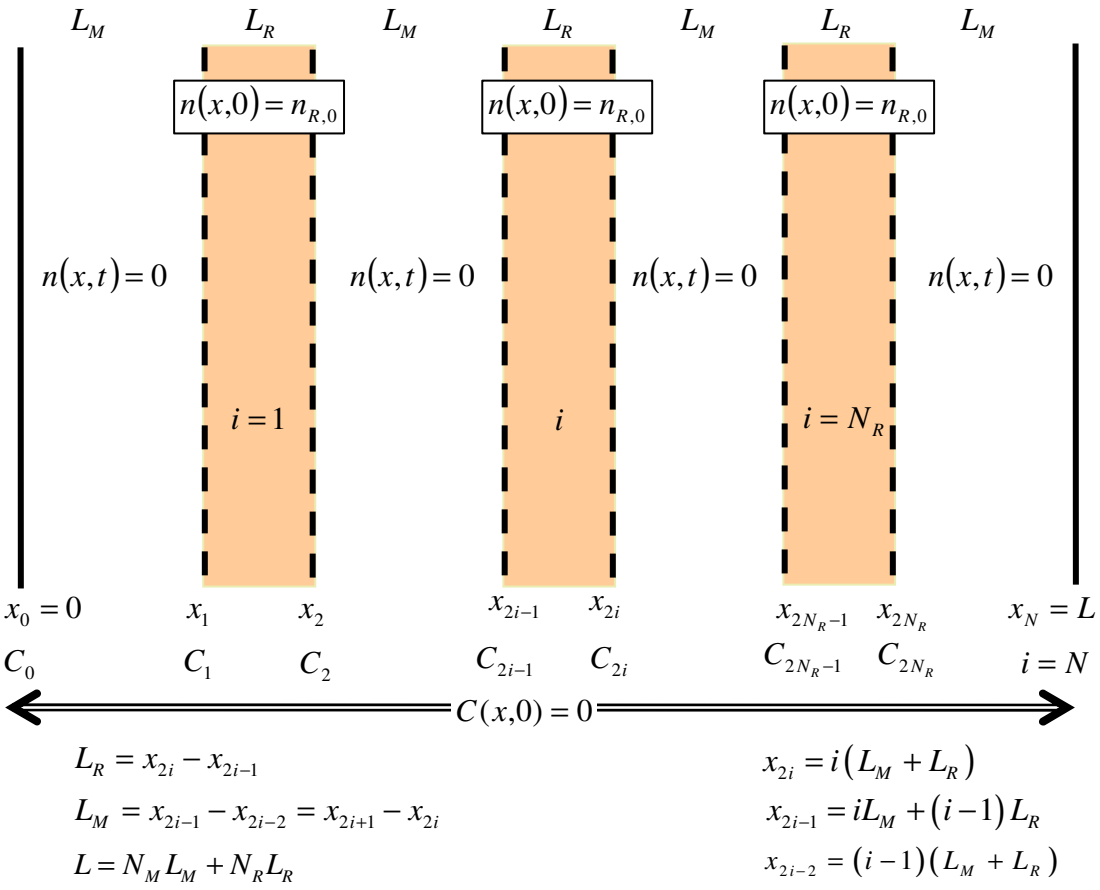

Figure 5.1: Layered polymer schematic. There are N_M inert matrix layers of thickness L_M alternating with N_R reactive layers of thickness L_R. Reactive sites are only present in reactive layers (initial concentration $n_{R,0}$).

The equations here are described assuming the first layer is always inert and the total number of layers is odd, i.e., $N_M = N_R + 1$. The analysis is extended in the

Supplemental Material section (see end of this chapter) to even number of layers ($N_M = N_R$) and to films where the first layer is reactive ($N_R = N_M + 1$). The one-dimensional transient transport in the layered film can be described by the material balances for oxygen and reactive sites over the whole film. The concentration of reactive sites n at the inert matrix layers is zero at all times, and the initial concentration of reactive sites is given by $n_{R,0}$ for all reactive layers,

$$n(x,t) = 0\,,\ x_{2i-2} < x < x_{2i-1},\quad i = 1,2,3...,N_R + 1\,, \tag{5.1}$$

$$n(x,0) = n_{R,0}\,,\ x_{2i-1} < x < x_{2i},\quad i = 1,2,3...,N_R\,. \tag{5.2}$$

For packaging applications, the upstream boundary is typically exposed to air and the downstream boundary is exposed to vanishingly small oxygen partial pressure. Initially, all reactive sites in the reactive layers are available and the whole film (inert and reactive layers) is devoid of oxygen. The film material balances with the initial and boundary conditions are given by

$$\frac{\partial C(x,t)}{\partial t} = \frac{\partial}{\partial x}\left[D(x)\frac{\partial C(x,t)}{\partial x} \right] - k_R\, C(x)\, n(x,t)\,, \tag{5.3}$$

$$\frac{\partial n(x,t)}{\partial t} = -\hat{v}\, k_R\, C(x,t)\, n(x,t)\,, \tag{5.4}$$

$$\text{I.C.:}\quad C(x,0) = 0,\quad n(x,0) = n_{R,0} N_R L_R / L\,, \tag{5.5}$$

$$\text{B.C.:}\quad C(0,t) = C_0,\quad C(L,t) = 0\,, \tag{5.6}$$

where x is the position along the thickness of the film, t is time, D is the oxygen diffusion coefficient, k_R is the reaction rate constant, n is the concentration of reactive

sites in the film, and $\hat{\nu}$ is the stoichiometric coefficient for the scavenging reaction. The diffusion coefficient for each layer is assumed to be constant, where $D(x) = D_R$ is the diffusion coefficient for the reactive layers, and $D(x) = D_M$ is the diffusion coefficient for the inert matrix layers. At the interfaces between reactive and inert matrix layers the flux and the oxygen partial pressure are continuous, but the oxygen concentration on the reactive and inert sides obey the equilibrium partitioning relation given by $p_i = C_{M,i}/S_M = C_{R,i}/S_R$, where S_M is the solubility coefficient for oxygen in the inert matrix and S_R is the solubility coefficient for oxygen in the in the reactive layer.

The oxygen flux at the downstream boundary and the total amount of oxygen permeated are quantities of interest derived from the solution of equations 5.3-5.6. The downstream flux J at time t is given by

$$J\big|_{x=L} = -\left(D\frac{\partial C}{\partial x} \right)\Bigg|_{x=L}, \tag{5.7}$$

and the total oxygen permeated through the membrane Q_t at time t is given by

$$Q_t = \int_0^t J\big|_{x=L}\, dt\,. \tag{5.8}$$

5.3 ANALYSIS

5.3.1 Analysis of early times to estimate initial leakage flux plateau

At early times, most reactive sites are still available, and a quasi-steady-state region is observed for the downstream oxygen flux, called the flux plateau. Approximate

analytical solutions to predict the initial flux plateau for homogeneous reactive membranes were derived in Chapter 2. Here, similar analysis is utilized for each reactive layer and combined with transport in the inert matrix layers to derive a system of equations for the layered film.

Inert matrix layer equations

At early times, the transport equations for the inert matrix layers reduce to steady state one-dimensional diffusion. The boundary conditions for each layer are given by the concentration at the upstream and downstream interfaces,

$$D_M \frac{d^2 C_M}{dx^2} = 0\,,\ x_{2i-2} < x < x_{2i-1},\quad i = 1,2,3...,N_R+1\,, \tag{5.9}$$

$$\text{B.C.:}\ \ C_M\left(x_{2i-2}\right) \equiv C_{M,2i-2}\,,\ C_M\left(x_{2i-1}\right) \equiv C_{M,2i-1}\,, \tag{5.10}$$

where C_M is the oxygen concentration within the inert matrix layer. The concentration profile and oxygen flux at each inert layer are thus given by

$$C_M\left(x\right) = \frac{C_{M,2i-1} - C_{M,2i-2}}{L_M} x + \frac{C_{M,2i-2}\, x_{2i-1} - C_{M,2i-1}\, x_{2i-2}}{L_M}\,, \tag{5.11}$$

$$J\big|_x = -D_M \frac{dC_M}{dx} = -D_M \frac{C_{M,2i-1} - C_{M,2i-2}}{L_M}\,. \tag{5.12}$$

Reactive layer equations

At early times, a quasi-steady state regime is observed, and most reactive sites are still available within the reactive layers,

$$n\left(x\right) \approx n_{R,0}\,,\ x_{2i-1} < x < x_{2i},\quad i = 1,2,3...,N_R\,. \tag{5.13}$$

The transport equations reduce to an equivalent steady-state first order reaction equation, and the boundary conditions for each layer are given by the concentration at the upstream and downstream interfaces,

$$\frac{d^2 C_R}{dx^2} - \alpha^2 C_R = 0\,, \tag{5.14}$$

$$\text{B.C.:}\;\; C_R\left(x_{2r-1}\right) = C_{R,2r-1}\,,\; C_R\left(x_{2r}\right) = C_{R,2r}\,, \tag{5.15}$$

where C_R is the oxygen concentration within the reactive layer and $\alpha = \sqrt{k_R\, n_{R,0} / D_R}$. The concentration profile at each inert layer is thus given by

$$\begin{aligned} C_R(x) = &\frac{C_{R,2i}\cosh\left(\alpha x_{2i-1}\right) - C_{R,2i-1}\cosh\left(\alpha x_{2i}\right)}{\sinh\left(\alpha L_R\right)}\sinh\left(\alpha x\right) \\ &+ \frac{C_{R,2i-1}\sinh\left(\alpha x_{2r}\right) - C_{R,2i}\sinh\left(\alpha x_{2i-1}\right)}{\sinh\left(\alpha L_R\right)}\cosh\left(\alpha x\right) \end{aligned}\,, \tag{5.16}$$

and the oxygen flux is given by

$$J\big|_x = \frac{-\alpha D_R}{\sinh\left(\alpha L_R\right)}\left\{C_{R,2i}\cosh\left[\alpha\left(x - x_{2i-1}\right)\right] - C_{R,2i-1}\cosh\left[\alpha\left(x - x_{2i}\right)\right]\right\}. \tag{5.17}$$

Note that unlike the inert matrix layers, which have uniform oxygen flux within the layer, for reactive layers the flux is a function of position. Evaluating the flux at the upstream and downstream boundaries of each layer gives

$$J\big|_{x_{2i-1}} = \frac{-\alpha D_R\left[C_{R,2i} - C_{R,2i-1}\cosh\left(\alpha L_R\right)\right]}{\sinh\left(\alpha L_R\right)}, \tag{5.18}$$

$$J\big|_{x_{2i}} = \frac{-\alpha D_R\left[C_{R,2i}\cosh\left(\alpha L_R\right) - C_{R,2i-1}\right]}{\sinh\left(\alpha L_R\right)}, \tag{5.19}$$

Reactive layer equations

At the interfaces between reactive and inert matrix layers, the flux and oxygen partial pressure are continuous, but the oxygen concentration on the reactive and inert sides obey the partition relation $p_i = C_{M,i}/S_M = C_{R,i}/S_R$, where S_M is the solubility coefficient for oxygen in the inert matrix and S_R is the solubility coefficient for oxygen in the in the reactive layer. The flux evaluated at the upstream layer boundary x_{2i-1} of a reactive layer i must equal the flux from the inert layer bound by $x_{2i-2} < x < x_{2i-1}$,

$$J\big|_{x_{2i-1}} = \underbrace{\frac{-\alpha D_R S_R \left[p_{2i} - p_{2i-1}\cosh(\alpha L_R)\right]}{\sinh(\alpha L_R)}}_{reactive} = \underbrace{\frac{-D_M S_M}{L_M}\left(p_{2i-1} - p_{2i-2}\right)}_{inert}. \tag{5.20}$$

Likewise, the flux evaluated at the downstream boundary x_{2i} of the same layer must equal the flux into the inert matrix layer bound by $x_{2i} < x < x_{2i+1}$,

$$J\big|_{x_{2i}} = \underbrace{\frac{-\alpha D_R S_R \left[p_{2i}\cosh(\alpha L_R) - p_{2i-1}\right]}{\sinh(\alpha L_R)}}_{reactive} = \underbrace{\frac{-D_M S_M}{L_M}\left(p_{2i+1} - p_{2i}\right)}_{inert}. \tag{5.21}$$

Rearranging equations 5.20 and 5.21 gives the two repeating partial pressure equations that define the layered system

$$-a\, p_{2i-2} + b\, p_{2i-1} - c\, p_{2i} = 0, \tag{5.22}$$

$$-c\, p_{2i-1} + b\, p_{2i} - a\, p_{2i+1} = 0, \tag{5.23}$$

where $a = S_M D_M / L_M$, $b = S_M D_M / L_M + \alpha S_R D_R \coth(\alpha L_R)$ and $c = \alpha D_R S_R / \sinh(\alpha L_R)$. Writing equations 5.22 and 5.23 for $i = 1$ to $i = N_R$ gives the complete system in matrix form,

$$\begin{bmatrix} b & -c & 0 & \cdots & 0 & 0 & 0 \\ -c & b & -a & \cdots & 0 & 0 & 0 \\ 0 & -a & b & \cdots & 0 & 0 & 0 \\ 0 & 0 & -c & \cdots & 0 & 0 & 0 \\ \vdots & \vdots & \vdots & \ddots & \vdots & \vdots & \vdots \\ 0 & 0 & 0 & \cdots & -a & b & -c \\ 0 & 0 & 0 & \cdots & 0 & -c & b \end{bmatrix} \begin{bmatrix} p_1 \\ p_2 \\ p_3 \\ p_4 \\ \vdots \\ p_{2N_R-1} \\ p_{2N_R} \end{bmatrix} = \begin{bmatrix} a\, p_{O_2} \\ 0 \\ 0 \\ 0 \\ \vdots \\ 0 \\ a\, p_N = 0 \end{bmatrix}. \tag{5.24}$$

Recall that the oxygen partial pressure at the downstream boundary is 0 for this problem, i.e., $p_N = p_L = 0$. Since the last layer is inert, the downstream oxygen flux for early times is given by

$$J\big|_L = \frac{-D_M}{L_M}\left(C_{M,N} - C_{M,2N_R}\right) = \frac{D_M C_{M,2N_R}}{L_M} = \frac{S_M D_M}{L_M}\, p_{2N_R}. \tag{5.25}$$

Note that only the oxygen partial pressure at x_{2N_R} is required for the calculation of the downstream flux. While equations 5.22 and 5.23 for partial pressure were derived based on a layered film with the first and last layers inert, the same pattern applies for any configuration of alternating layers, and the downstream flux can be estimated using the proper form of the flux for either reactive or inert matrix layers, as discussed in the Supplemental Material section at the end of this chapter.

The linear system defined by equation 5.24 was solved analytically using Mathematica for various N_M and N_R, giving expressions for predicting the downstream flux at early times. The full analytical solution includes a denominator consisting of multiple exponential terms and pre-factors. However, in the limit of $\Phi_R \gg 1$, where $\Phi_R = \sqrt{\left(L_R N_R\right)^2 k_R\, n_{R,0} / D_R}$ is the Thiele modulus for the reactive layers, a pattern has

been determined based on the denominator's leading order exponential term e^{Φ_R} and its pre-factor, giving the generic prediction for the initial flux plateau,

$$J\big|_{x=L} = \frac{2^{N_R} H^{N_M-1} D_M{}^{N_M} \alpha D_R S_M p_{O_2} e^{-\Phi_R}}{\left(H D_M + \alpha D_R L_M\right)^{N_M-N_R+1} \left(2H D_M + \alpha D_R L_M\right)^{N_R-1}}, \tag{5.26}$$

where $\alpha = \sqrt{k_R n_{R,0}/D_R}$ and $H = S_M/S_R$ is the oxygen partition coefficient between inert and reactive layers. In order to evaluate the flux dependence on the number of layers for an equivalent loading of scavenger material, the individual layer thickness can be expressed in terms of the volume fraction of reactive polymer, ϕ, and the total thickness of the film, L, making $L_R = \phi L/N_R$ and $L_M = (1-\phi)L/N_M$. The leading order estimate for the downstream flux plateau for early times thus becomes

$$J_{pl} = \frac{2^{N_R} \Delta D_M S_M p_{O_2} \Phi_R e^{-\Phi_R}}{H\phi L\left(1+\gamma/N_M\right)^{N_M-N_R+1} \left(2+\gamma/N_M\right)^{N_R-1}}, \tag{5.27}$$

where $\gamma = \Phi_R \Delta(1-\phi)/\phi H$, $\Delta = D_R/D_M$ and $\Phi_R = \sqrt{(\phi L)^2 k_R n_{R,0}/D_R}$. While equation 5.27 for the downstream flux was derived assuming the first layer of the film is inert matrix, this analytical expression is valid for any odd or even number of layers, either starting with inert matrix or with reactive layer, and by entering the proper number of reactive and inert layers (N_R, N_M) as discussed in the Supplemental Material section at the end of this chapter.

Figure 5.2 shows the initial flux plateau predictions versus the total number of layers for films with the first layer inert for various Δ and k_R, as indicated in charts. Solid lines represent the estimate based on the full analytical solution of equation 5.24;

symbols represent the leading order solution, given by equation 5.27. For all cases shown, the predictions were evaluated for a multilayer membrane of total thickness L=0.025 cm, reactive polymer volume fraction ϕ=0.1, with PET as the inert matrix polymer (i.e., D_M =4.84×10^{-4} cm^2/day, $C_0 = S_M p_{O_2}$ =0.92 μmol$_{O2}$/cm^3) and assuming the partition coefficient H=1. The rate constant is k_R=0.42 cm^3/μmol$_{RS}$ for the cases shown in figure 5.2a, k_R=3.7 cm^3/μmol$_{RS}$ day for figure 5.2b and k_R=10.4 cm^3/μmol$_{RS}$ day for figure 5.2c. For small k_R (figure 5.2a) the leading order prediction is in excellent agreement with the flux plateau prediction based on the full analytical solution of equation 5.24 for Δ=0.17 and 0.36 but becomes poor for large Δ=3. For larger k_R (figures 5.2b and 5.2c) both solutions give the same values. This is not surprising, since the leading order prediction assumes that $\Phi_R \gg 1$ to discard lower order exponential terms, but if the rate constant is k_R=0.42 cm^3/μmol$_{RS}$ and Δ=1 and 3 the values of Φ_R are 6.5 and 3.8, respectively. Note that for all cases, the leading order prediction of equation 5.27 is in excellent agreement with the prediction based on the full solution of 5.24 if the total number of layers is small. Figure 5.3 shows the flux estimates for the same cases shown in figure 5.2, except that the flux plateau is normalized by the flux plateau for layer configuration 010 (0 represents inert matrix layer, 1 represents reactive layer). While the absolute value of the initial flux plateau decreases with Δ by orders of magnitude, as seen in figure 5.2, larger values of Δ lead to greater reduction in the initial flux plateau by increasing the number of layers, as shown in figure 5.3.

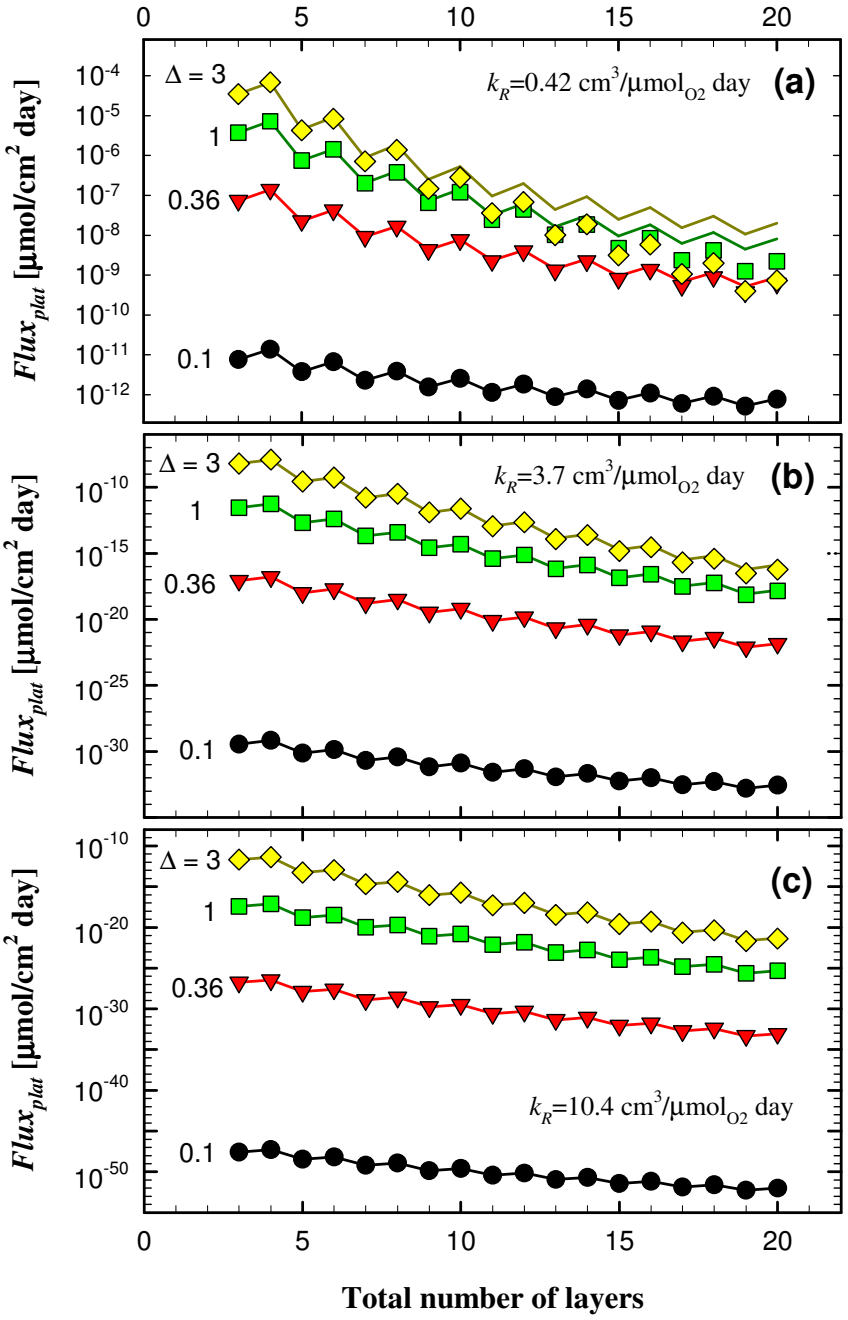

Figure 5.2: Flux plateau estimate versus total number of layers. Symbols: leading order estimate. Solid lines: estimate based on full solution of equation 5.24. The reaction rate constant k_R is 0.42, 3.7 and 10.4 cm^3/μmol$_{RS}$day for (a), (b) and (c) respectively. For all cases L = 0.025 cm, C_0 = 0.92 μmol$_{O2}$/cm^3, D_M = 4.84×10^{-4} cm^2/day, H = 1, with Δ varying as indicated in each chart.

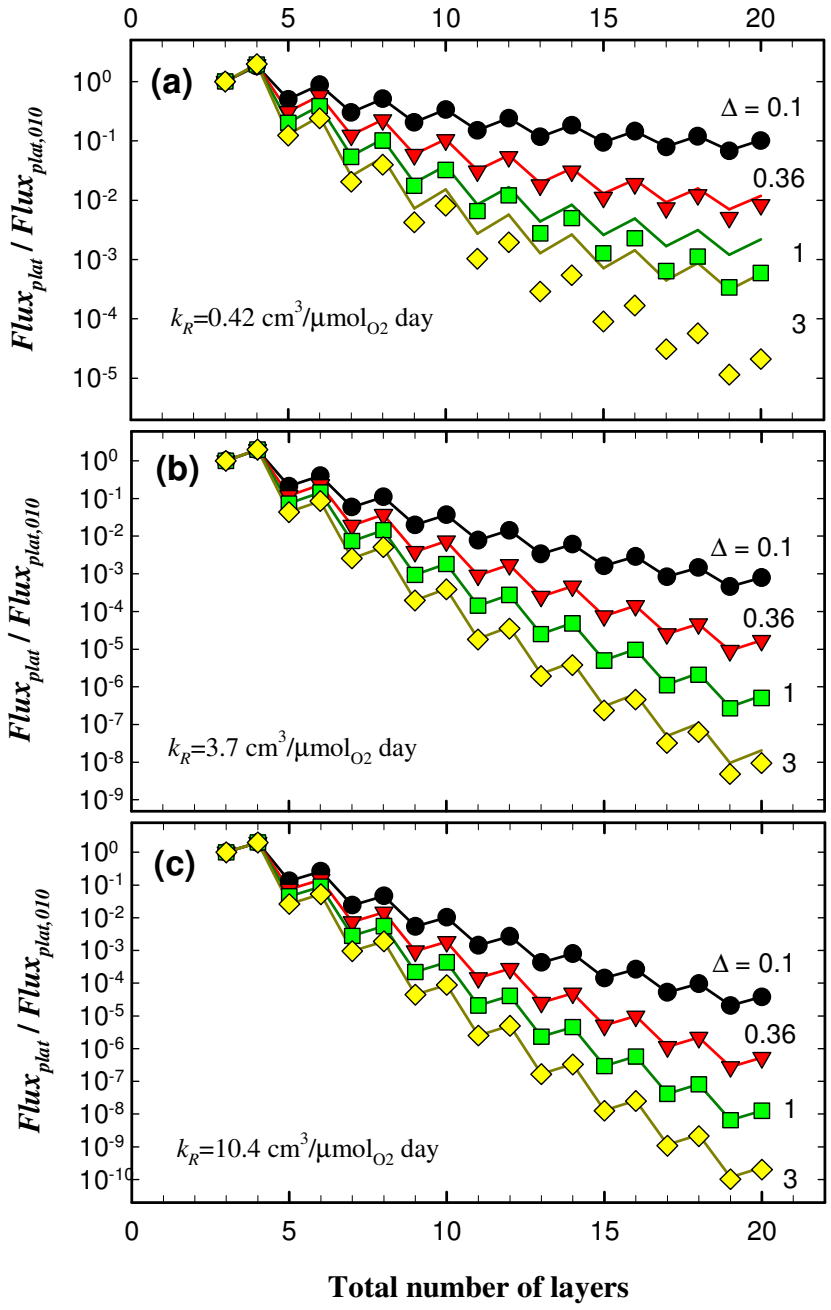

Figure 5.3: Flux plateau normalized by flux plateau for configuration 010 versus total number of layers. Symbols: leading order estimate. Solid lines: estimate based on full solution of equation 5.24. The reaction rate constant k_R is 0.42, 3.7 and 10.4 cm^3/μmol$_{RS}$day for (a), (b) and (c) respectively. For all cases shown L = 0.025 cm, C_0 = 0.92 μmol$_{O2}$/cm^3, D_M = 4.84×10^{-4} cm^2/day, H = 1, with Δ varying as indicated in each chart.

Figure 5.4 explores the effect of varying H when $\Delta=1$ for the same layer configuration and rate constants used in figure 5.2 (i.e., k_R=0.42, 3.7 and 10.4 $cm^3/\mu mol_{RS}$ day for figures 5.4a, b and c, respectively). Solid lines represent the estimate based on the full analytical solution of equation 5.24; symbols represent the leading order solution, given by equation 5.27. The leading order prediction is in excellent agreement with the flux plateau prediction based on the full analytical solution of equation 5.24 for most cases, except for a combination of small k_R (figures 5.4a), small H and large total number of layers. Decreasing H magnifies the effect of total number of layers in the flux plateau, as illustrated in figure 5.4.

The effects of Δ, H, and k_R, may be explained by inspection of equation 5.27 and its parameter groups $\Phi_R = \sqrt{(\phi L)^2 k_R n_{R,0}/D_R}$ and $\gamma = \Phi_R \Delta(1-\phi)/\phi H$. Decreasing Δ causes Φ_R to increase, thus reducing the initial flux plateau. However, decreasing Δ also causes γ to decrease, thus reducing the effect of the number of layers on the initial flux plateau. Decreasing H causes γ to increase, thus magnifying the effect of number of layers on the initial flux plateau. Finally, increasing k_R increases both Φ_R and γ, thus decreasing the initial flux plateau and magnifying the effect of number of layers on the plateau value.

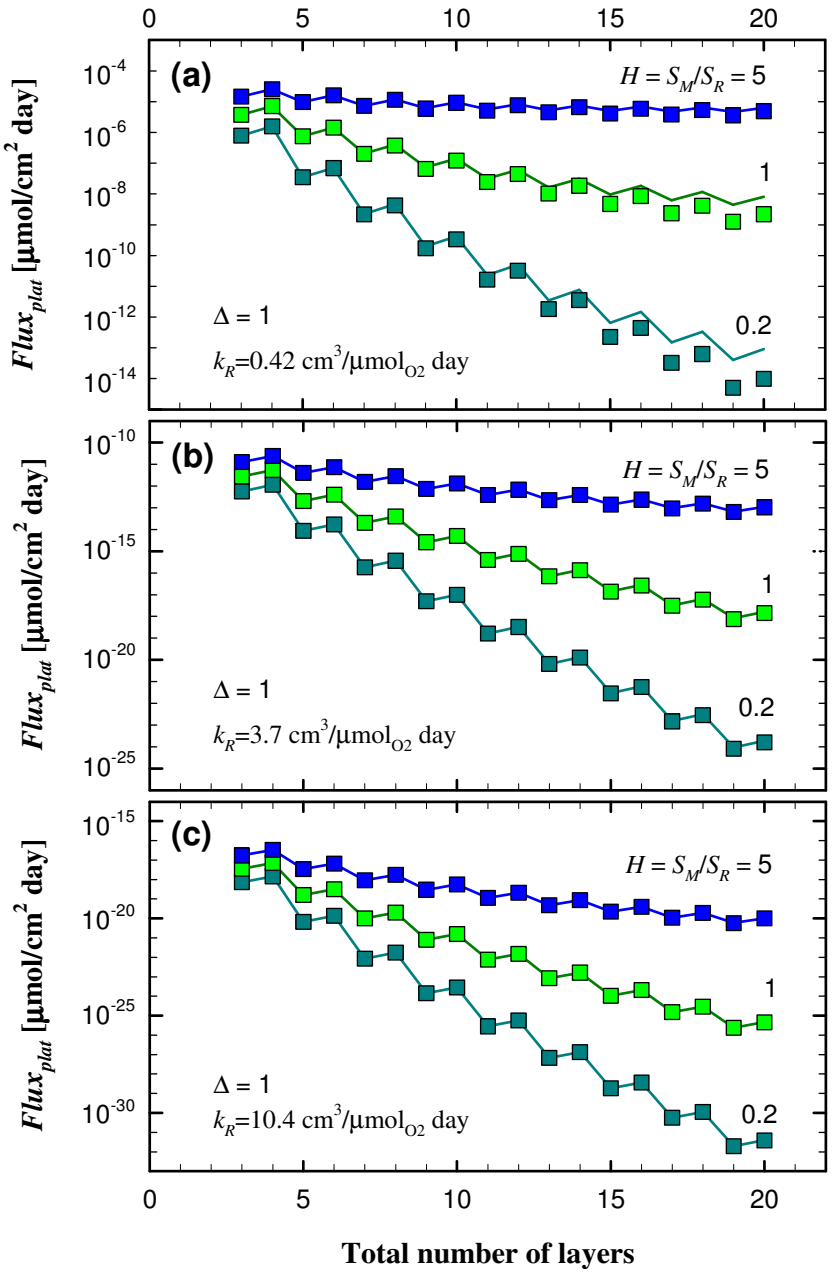

Figure 5.4: Flux plateau estimate versus total number of layers. Symbols: leading order estimate. Solid lines: estimate based on full solution of equation 5.24. The reaction rate constant k_R is 0.42, 3.7 and 10.4 cm^3/ μmol$_{RS}$day for (a), (b) and (c) respectively. For all cases L = 0.025 cm, C_0 = 0.92 μmol$_{O2}$/cm^3, D_M = 4.84×10^{-4} cm^2/day, Δ = 1, with H varying as indicated in each chart.

As illustrated in figures 5.2-5.4 and discussed above, when all other parameters are kept the same, increasing the number of layers causes the initial flux plateau to decrease. While parameters such as Δ, H, and k_R may magnify or diminish the effect of number of layers, the trend is valid for all cases. The physical interpretation of this observation lies on the effective increase of length of the reactive region when the number of layers is increased. Looking at layer sequence 010, where 0 represents inert matrix layer and 1 represents a reactive layer, all reaction takes place in the continuous region of thickness $L_R = \phi L$. On the other hand, a film with layer sequence 01010 has an inert matrix layer of thickness $L_M = (1-\phi)L/3$ between the two reactive layers, slowing down oxygen transport and thus increasing contact time between oxygen and scavenging sites at the second reactive layer. For a film with N_M inert matrix layers (where the first and last layers are inert), the reaction region is increased to $L - 2L_M = L - 2(1-\phi)/N_M$, thus the larger the number of layers, the longer the oxygen diffusion path between reactive layers, causing the initial flux plateau to decrease. Note that this comparison is only meaningful for similar type of configurations: i.e., a film with configuration 010 must be compared to films with configuration 01010, 0101010, and so on. Likewise, a film with configuration 01 must be compared to films with configuration 0101, 010101, etc.

5.3.2 Steady state analysis to determine time lag

Here, the technique used to estimate the time lag for a homogeneous reactive membrane discussed in Chapter 2 is adapted for the time lag analysis for multiple layers.

To obtain an analytical expression, all layers are set to have same diffusion coefficient and the same solubility coefficient, i.e., $D_R = D_M$ and $S_R = S_M$. Combining the oxygen material balance and the reactive sites material balance for the entire film (equations 5.3-5.4) gives

$$\frac{\partial C}{\partial t} - \frac{1}{\hat{\nu}} \frac{\partial n}{\partial t} = D_M \frac{\partial^2 C}{\partial x^2}. \tag{5.28}$$

Integration of equation 5.28 in space from arbitrary x to L, followed by integration over the entire thickness of the film gives

$$\int_0^L \int_x^L \left(\frac{\partial C}{\partial t} - \frac{1}{\hat{\nu}} \frac{\partial n}{\partial t} \right) dy dx = D_M \left. \frac{\partial C}{\partial x} \right|_L \int_0^L dx - D_M \int_0^L \frac{\partial C}{\partial x} dx. \tag{5.29}$$

Using reversal of the integration order to evaluate the double integral, equation 5.29 above becomes

$$\int_0^L x \frac{\partial C}{\partial t} dx - \frac{1}{\hat{\nu}} \int_0^L x \frac{\partial n}{\partial t} dx = L D_M \left. \frac{\partial C}{\partial x} \right|_L + D_M C_0, \tag{5.30}$$

where C_0 is the oxygen concentration at the upstream boundary. Equation 5.30 is integrated from 0 to an arbitrary time t, giving

$$\int_0^t \int_0^L x \frac{\partial C}{\partial t} dx dt - \frac{1}{\hat{\nu}} \int_0^t \int_0^L x \frac{\partial n}{\partial t} dx dt = L \int_0^t D_M \left. \frac{\partial C}{\partial x} \right|_L dt + D_M C_0 \int_0^t dt. \tag{5.31}$$

Using the oxygen permeate Q_t for time t as defined by equation 5.8, evaluating the integrals and looking at the limits for very long times gives the asymptotic expression for the steady state oxygen permeate

$$Q_{t\to\infty} = \frac{D_M C_0}{L} t - \frac{1}{L}\int_0^L x C_{SS} dx - \frac{1}{\hat{v} L}\int_0^L x n_{t=0} dx, \tag{5.32}$$

where $n_{t=0}$ is the initial concentration of reactive sites along the entire film and C_{SS} is the linear steady-state oxygen concentration profile, given by $C_{SS} = C_0\left(1 - x/L\right)$. The time lag θ is calculated by finding the time when equation 5.32 crosses the time axis, i.e., when $Q_{t\to\infty} = 0$, giving

$$\theta_{\Delta=1,H=1} = \frac{L^2}{6D_M} + \frac{1}{D_M C_0 \hat{v}}\int_0^L x n_{t=0} dx. \tag{5.33}$$

The steady-state analysis used to derive equation 5.33 is valid for either a homogeneous or a layered film with any layer configuration, as long as the diffusion coefficients and the solubility coefficients are the same for all layers. To complete the calculation of time lag, the details of the layer configuration must be defined, as discussed next.

Concentration of reactive sites

For the inert matrix layers, the concentration of reactive sites is always 0, so only the reactive layers need to be computed. Assuming the first layer is inert matrix, the integral term containing the initial concentration of reactive sites is given by

$$\int_0^L x n_{t=0} dx = \sum_{i=1}^{N_R} \int_{(i-1)L_R + rL_M}^{i(L_M + L_R)} x n_{R,0} dx = \frac{n_{R,0}}{2} N_R L_R \left[\left(N_R + 1\right) L_M + N_R L_R\right], \tag{5.34}$$

where $n_{R,0}$ is the initial concentration of reactive sites in each reactive layer. The summation can be evaluated, giving the closed form result for the integral.

Time lag calculation

The time lag prediction for a multilayer system where the first layer is inert is given by substituting equation 5.34 into the generic expression for time lag given by equation 5.33. The time lag prediction for a multilayer system with odd total number of layers, θ_{odd}, is given by

$$\frac{\theta_{odd,H=1,\Delta=1}}{\theta_0} = \frac{3}{\nu} + 1, \tag{5.35}$$

and for an even total number of layers θ_{even} becomes,

$$\frac{\theta_{even,H=1,\Delta=1}}{\theta_0} = \frac{3}{\nu}\frac{\left(1-\phi+N_M\right)}{N_M} + 1, \tag{5.36}$$

where $\nu = S_M p_{O_2} \hat{v} / \phi n_{R,0}$ and $\theta_0 = L^2/6D_M$ is the diffusion time lag of the film, i.e. the time lag of the film without any reactive particles. Comparing equations 5.35 and 5.36, note that θ_{even} is a function of the number of layers (expressed by the number of inert layers N_M), while θ_{odd} is not. If all physical parameters remain the same, except the number or layers, the maximum value of θ_{even} is achieved for a single pair of inert and reactive layers, i.e., $N_M = 1$. As the number of layers increases, the value of θ_{even} decreases. For very large N_M the dependence vanishes, making $\theta_{even} = \theta_{odd}$. Analogous expressions for multilayer systems where the first layer is reactive are given in the Supplemental Material section at the end of this chapter.

Prediction of time lag when the diffusion coefficient is not the same for all layers

Equations 5.35 and 5.36 were derived following a well established asymptotic analysis for determination of time lag. However, the method does not easily apply to a layered system where the diffusion coefficient is different for reactive and inert layers. Systematic analysis of the numeric solution of equations 5.3-5.6 (figure 5.5) resulted in the development of an equation analogous to 5.35 for odd total layers, but that is applicable when $\Delta \neq 1$ and $H \neq 1$. Figure 5.5 shows the time lag of the reactive multilayer film versus the time lag $\theta_{0,eff} = L^2/6D_{eff}$ for an inert film of effective diffusion coefficient $D_{eff} = \Delta D_M / \left[H\phi + \Delta(1-\phi) \right]$. The symbols represent the time lag calculated by numerical solution varying the volume fraction ϕ and the ratio between the diffusion coefficients of the reactive and inert layers Δ. The data was arranged in terms of the parameter group $\nu = S_M p_{O_2} \hat{v} / \phi n_{R,0}$. Symbols represent time lag calculated by numerical solution, while the solid lines represent $3\theta_{0,eff}/\nu$, indicating the time lag for odd total number of layers for $\Delta \neq 1$ and $H \neq 1$ can be predicted by

$$\frac{\theta_{odd}}{\theta_{0,eff}} = \frac{3}{\nu} + 1, \tag{5.37}$$

Note that when $\Delta = 1$ and $H = 1$, equation 5.37 reverts back to equation 5.35, enabling its use for both cases. Unfortunately, this approach does not extend to even total layers.

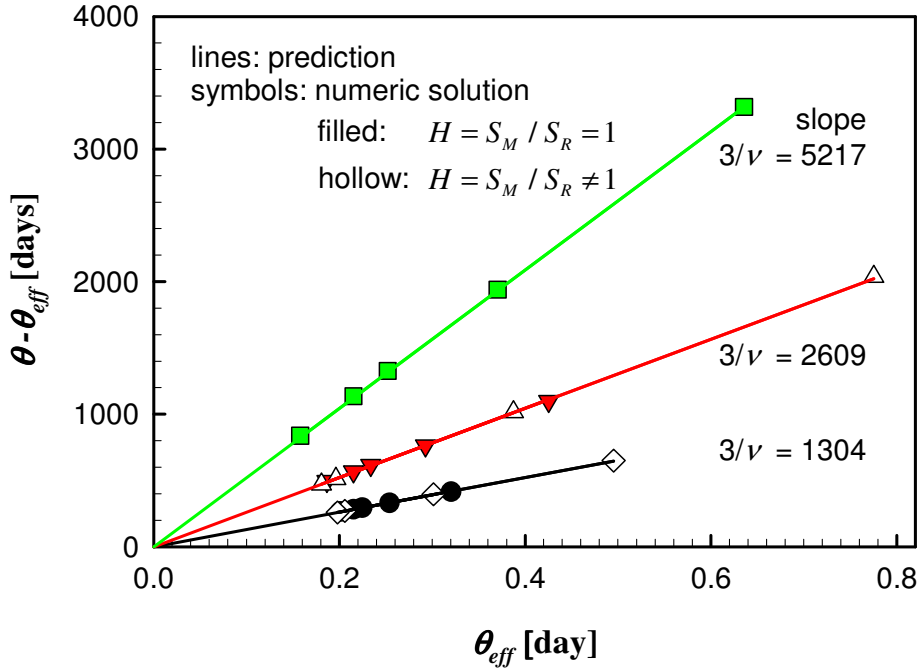

Figure 5.5: Time lag for the reactive film, θ, versus the time lag for an equivalent inert layer film, $\theta_{0,eff}$. Symbols represent time lag obtained by numerical solution for a film with three layers, with inert first and last layers. Parameter values are given in Table 5.1, except that ϕ, Δ and H varied, resulting in ν and $\theta_{0,eff}$ indicated in chart.

Steady-state downstream flux

The steady-state flux is given by $J_{SS} = P\left(p_{O_2,0} - p_{O_2,L}\right)/L$, where P is the effective permeability of the composite, which is obtained by the well known additive relation between the resistance to flux in each layer (Crank 1975),

$$\frac{L}{P} = \sum_{i=1}^{N} \frac{L_i}{P_i} = N_R \frac{L_R}{P_R} + N_M \frac{L_M}{P_M}, \tag{5.38}$$

where $P_M = S_M D_M$ and $P_R = S_R D_R = S_M D_M \Delta / H$. Since for the reactive membrane problem studied in this chapter the downstream pressure $p_{O_2,L}$ is vanishingly small, using $L_R = \phi L / N_R$ for reactive layer thickness and $L_M = (1-\phi) L / N_M$ for inert layer thickness, the steady-state flux is given by

$$J_{SS} = \frac{P p_{O_2}}{L} = \frac{\Delta D_M S_M p_{O_2}}{L\left[\phi H + \Delta(1-\phi)\right]}. \tag{5.39}$$

The steady-state flux given by equation 5.39 is valid for any layer configuration and values of $\Delta = D_R / D_M$ and $H = S_M / S_R$.

5.4 EXAMPLE CALCULATIONS

Equations 5.3-5.6 were solved numerically using an explicit finite difference method. The equations were discretized using a two-point forward difference for the time derivatives and a three-point central difference for the spatial derivatives, and enforcing the equilibrium and boundary conditions at each interface (see Supplemental Material section at the end of this chapter). Table 5.1 lists the parameters used for the base case calculations. Variations from these parameters are indicated with results, when appropriate. The downstream oxygen flux defined by equation 5.7 and the cumulative permeate, defined by equation 5.8 are plotted versus time for various cases. The results are organized in two categories: (1) effects of layer configuration and (2) effects of physical parameters on barrier properties, as discussed in the next sections.

Table 5.1: List of parameters for the multilayer base case calculations. All values except for the rate constant k_R match the values used as the base case for the polymer blend calculations in Chapter 3. The values in parenthesis are given in the units used in Chapter 3. Note that the scavenging capacity used in Chapter 3 is defined by $\beta \equiv n_{R,0}/\hat{\nu}$.

Symbol	Name	Value
L	Total film thickness	0.025 cm (250 μm)
ϕ	Volume fraction of reactive layers in film	0.1
$n_{R,0}$	Initial concentration of reactive sites in reactive layers	8000 μmol$_{RS}$/cm^3 (8x10^{-3} mol$_{RS}$/cm^3)
$\hat{\nu}$	Stoichiometric coefficient	2 μmol$_{RS}$/ μmol$_{O2}$
S_M	Oxygen solubility coefficient for the inert matrix layers	4.38 μmol$_{O2}$/cm^3 atm (0.098 cm^3(STP)/cm^3 atm)
D_M	Oxygen diffusion coefficient for the inert matrix layers	4.84x10^{-4} cm^2/day (5.6x10^{-9} cm^2/sec)
S_R	Oxygen solubility coefficient for the reactive layers	4.38x10^{-6}/cm^3 atm (0.098 cm^3(STP)/cm^3 atm)
D_R	Oxygen diffusion coefficient for the reactive layers	1.73x10^{-4} cm^2/day (2x10^{-9} cm^2/sec)
k_R	Reaction rate coefficient	0.42 cm^3/ μmol$_{RS}$ day

5.4.2 Effect of layer configuration on transient barrier performance

When compared to homogeneous and blend films, multilayer films offer additional design flexibility in the selection of the layer configuration (e.g., total number, sequence, etc.). This section focuses on the discussion of the effects of layer configuration on barrier performance when all other design parameters remain constant. Figure 5.6 illustrates the effects of total number of layers for films where the first layer is inert and the total number of layers is odd. This is a likely configuration for packaging

application, as the scavenging material may be encapsulated between mechanically stable layers. Figure 5.6a and 5.6b show the transient downstream flux and the cumulative oxygen permeate both plotted on log-log scales versus time. Inert layers are represented by 0 in the layer configuration labels, and reactive layers are represented by 1. Unlike homogeneous and blend films, that showed an initial flux plateau followed by a smooth rise to steady state, the multilayer films show additional inflexion points between the initial plateau and steady state. These intermediate inflexion points seem to result from the exhaustion of reactive sites within each layer, as the number of inflexions coincides with the number of reactive layers. The vertical dashed lines in figure 5.6 represent the time lag calculated from the numerical solutions, which is the same for all three cases as predicted by equations 5.35 and 5.37. The transient flux and consequently the oxygen permeate however are quite dependent on the number of layers, with the initial flux plateau being one order of magnitude lower for a film with a total of seven layers (0101010) compared to a film of three layers (010). This reduction of flux plateau can be predicted by equation 5.27, as illustrated in figures 5.2-5.4. At intermediate times, there are cross-over points in the flux chart, giving the three-layer film the lowest flux, until eventually all cases merge into the same steady state values. Figure 5.6b shows the oxygen permeate on the same time scale for easy comparison, showing a much less pronounce difference after the crossover point. Note that the cross-over time is ~100 days, and time lag is ~300 days, thus the choice of additional layers may be advantageous when very low oxygen exposure is preferable at the early portion of the product life, particularly since the exposure at intermediate times is comparable.

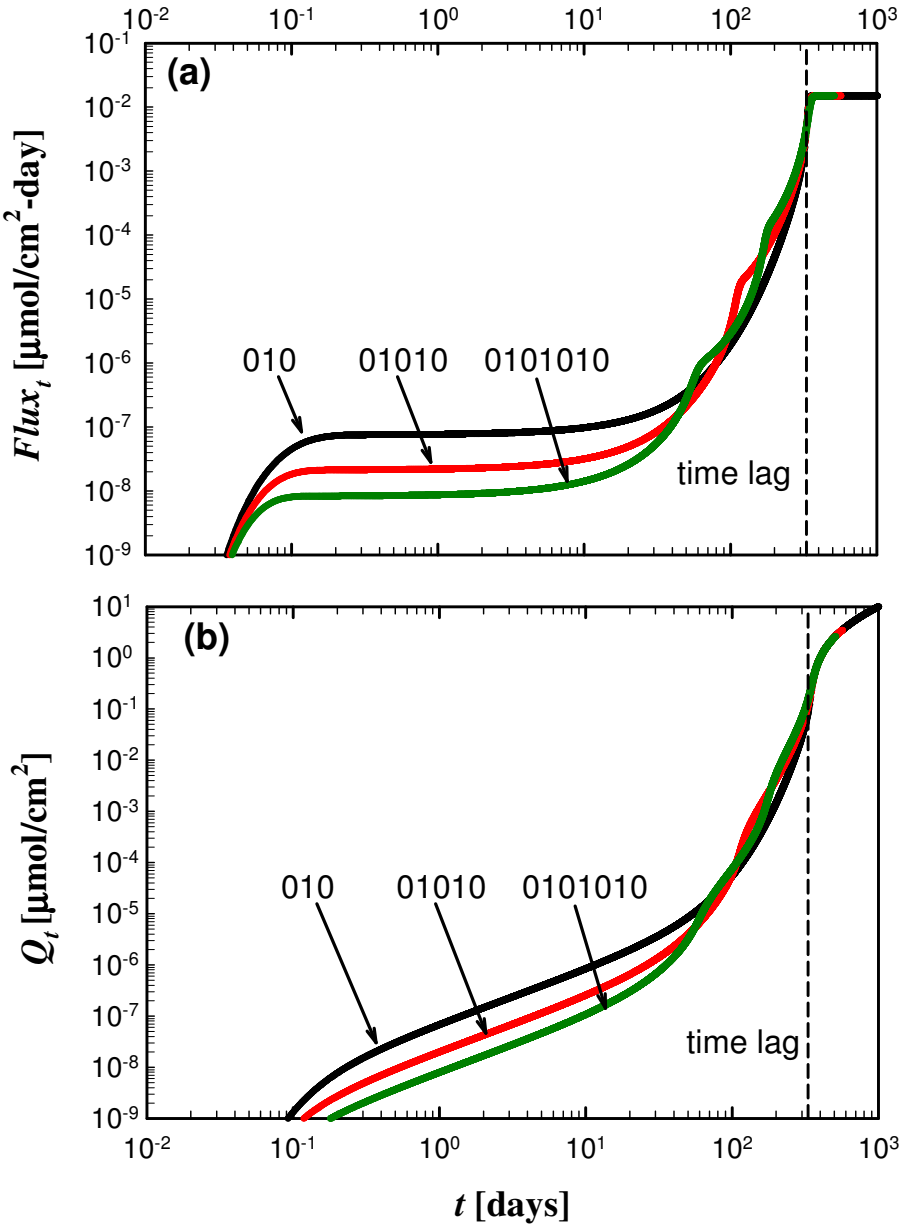

Figure 5.6: (a) Downstream flux and (b) oxygen permeate versus time in log-log scale. Layer sequence for each case indicated in chart, where 0 represents an inert layer, and 1 represents a reactive layer. All configurations shown have odd total number of layers. The dashed vertical line indicates time lag θ calculated from the numerical solution. All cases shown use the parameter values given in table 5.1.

Figure 5.7a shows the transient downstream flux versus time and figure 5.7b shows the cumulative oxygen permeate versus time, both on log-log scales, for even total number of layers. As with the previous charts, inert layers are represented by 0 in the layer configuration labels, and reactive layers are represented by 1. When the total number of layers is even, both the order and the number of layers affect time lag, as predicted by equations 5.36 and 5.A.7 (see the Supplemental Material section at the end of this chapter). The time lag is the maximum for the configuration 01 (i.e., first layer inert, second layer reactive) and the minimum for configuration 10. As the number of layers increase, the order of the layers becomes less important, and eventually films with first layer inert or reactive will have the same time lag. The value of the initial flux plateau is only affected by the total number of layers, but as can be seen in the figure 5.7a, the plateau duration is much longer for films where the first layer is inert. Similarly to the configurations discussed in figure 5.6, there is a crossover point where the initially lower flux and permeate (5.7b) for the 0101 configuration becomes large enough to surpass the 01 film. For the films with the first layer reactive, this crossover point is not observed, making 1010 configuration better than 10 configuration at all times.

Figure 5.8a compares the downstream flux for films with configuration 010 and 101. While the time lag and the steady-state flux are the same for both films, the 101 configuration consistently has higher flux than 010. Figure 5.8b compares configuration 010 to 01 and 0101. Both 01 and 0101 have larger time lag than 010 (desirable). However the flux for 0101 is higher than for 010 until very close to steady state. For applications that tolerate higher flux early on, the extended time lag of 01 may be attractive.

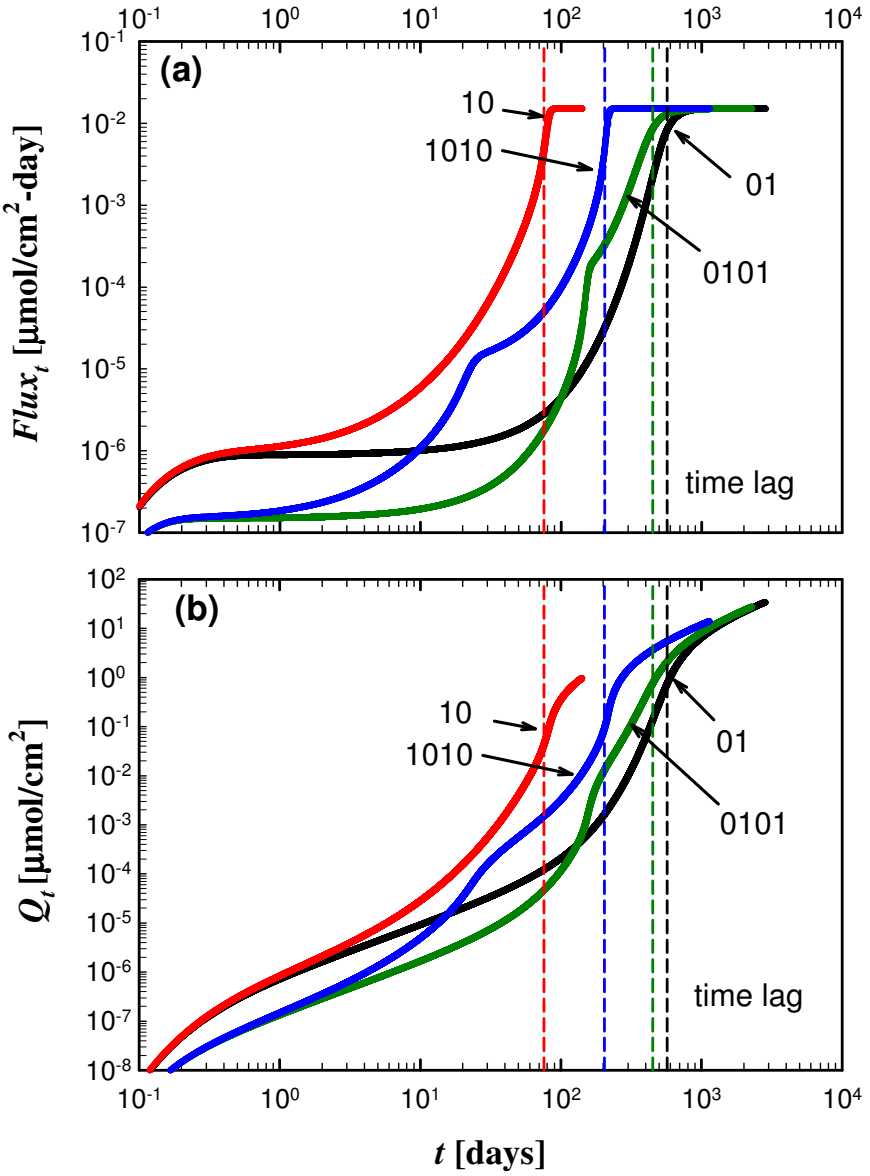

Figure 5.7: (a) Downstream flux and (b) oxygen permeate versus time in log-log scale. Layer sequence for each case indicated in chart, where 0 represents an inert layer, and 1 represents a reactive layer. All configurations shown have even total number of layers. The dashed vertical line indicates time lag θ calculated from the numerical solution. All cases shown use the parameter values given in table 5.1.

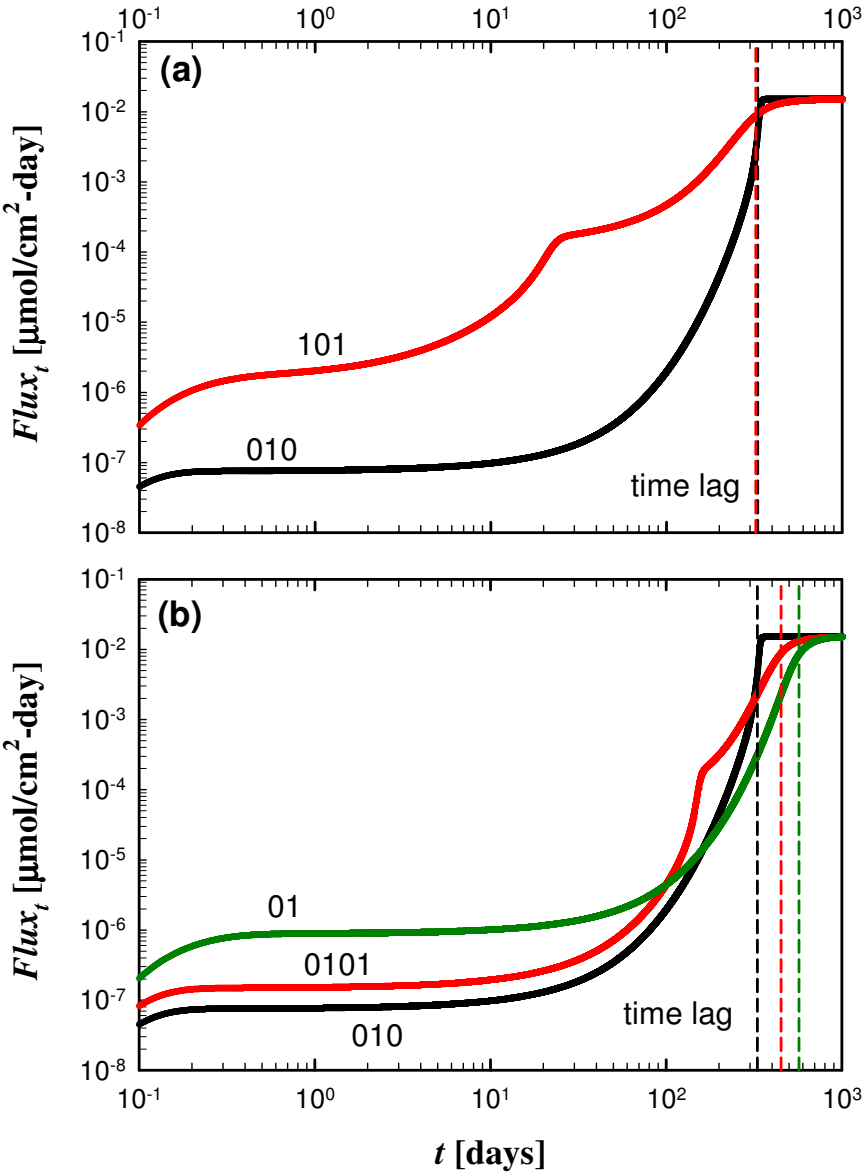

Figure 5.8: Downstream flux versus time for various layer configurations. Layer sequences for each case are indicated in chart, where 0 represents an inert layer, and 1 represents a reactive layer. The dashed vertical lines represent time lag θ calculated from the numerical solution by extrapolating the asymptote $Q_{t\to\infty}$ to the time axis. All cases shown use the parameter values given in table 5.1.

Table 5.2 summarizes the layer configurations discussed in figures 5.6-5.8, along with key results. N_M is the number of inert matrix layers, each of thickness L_M. Similarly, N_R is the number of reactive layers, each of thickness L_R. There are many trade-offs in the selection of the ideal layer configuration, as there are no combinations that give both the largest time lag and the smallest flux plateau. The differences in the transient behavior make some choices better for early times in the useful life of the barrier, and others for later times. One key example is shown in figure 5.8b, where 0101 underperforms 010, even though the time lag for 0101 is 120 days longer than for 010.

Table 5.2: Comparison of time lag θ and initial flux plateau J_{pl} obtained from the numerical solutions for several layer configurations. Layer sequence for each case indicated in table, where 0 represents an inert layer, and 1 represents a reactive layer. All cases use the parameter values given in table 5.1

Layer sequence	N_M --	N_R --	L_M (μm)	L_R (μm)	θ (day)	J_{pl} (μmol/cm^{2}day)
01	1	1	225	25	570	$1x10^{-6}$
10	1	1	225	25	76	$1x10^{-6}$
010	2	1	112.5	25	331	$7.3x10^{-8}$
101	1	2	225	12.5	323	$1.5x10^{-6}$
0101	2	2	112.5	12.5	450	$1.5x10^{-7}$
1010	2	2	112.5	12.5	204	$1.5x10^{-7}$
01010	3	2	75	12.5	331	$2.1x10^{-8}$
0101010	4	3	56.25	8.33	331	$8.2x10^{-9}$

In general, however, layer configurations where the first layer is inert outperform configurations where the first layer is reactive. Furthermore, if very low initial flux is desirable at the expense of shorter life times, configurations with odd total number of layers are preferable, and increasing the number of layers further reduces the plateau. On the other hand, if the goal is very long duration and moderate initial flux is tolerated, then configuration 01 would be the choice.

5.4.3 Effect of physical parameters on barrier properties

The previous section focused on the discussion of the effects of layer configuration on the barrier properties. This section focuses on the effects of physical parameters. Unless noted, the results in this section are given for layer configuration 010, i.e., a reactive layer between two inert matrix layers. The parameters values given in table 5.1 are used as the base case, and variations are indicated with each result. Figure 5.9a shows the downstream flux versus time on a log-log scale for varying $\Delta = D_R / D_M$ as indicated in chart. Figure 5.9b shows the oxygen permeate versus time on a linear scale for the same films shown in figure 5.9a. Reducing Δ modestly reduces the steady-state flux, but it reduces the initial flux plateau by orders of magnitude. This can be predicted by inspecting equation 5.27 for the initial flux plateau and the results shown in figures 5.2-5.4. As illustrated in figure 5.9b, reducing Δ increases time lag with a highly non-linear dependence, as evidenced by the large increase caused by changing Δ from 0.36 to 0.17 compared to the modest increase caused by changing Δ from 3 to 1.

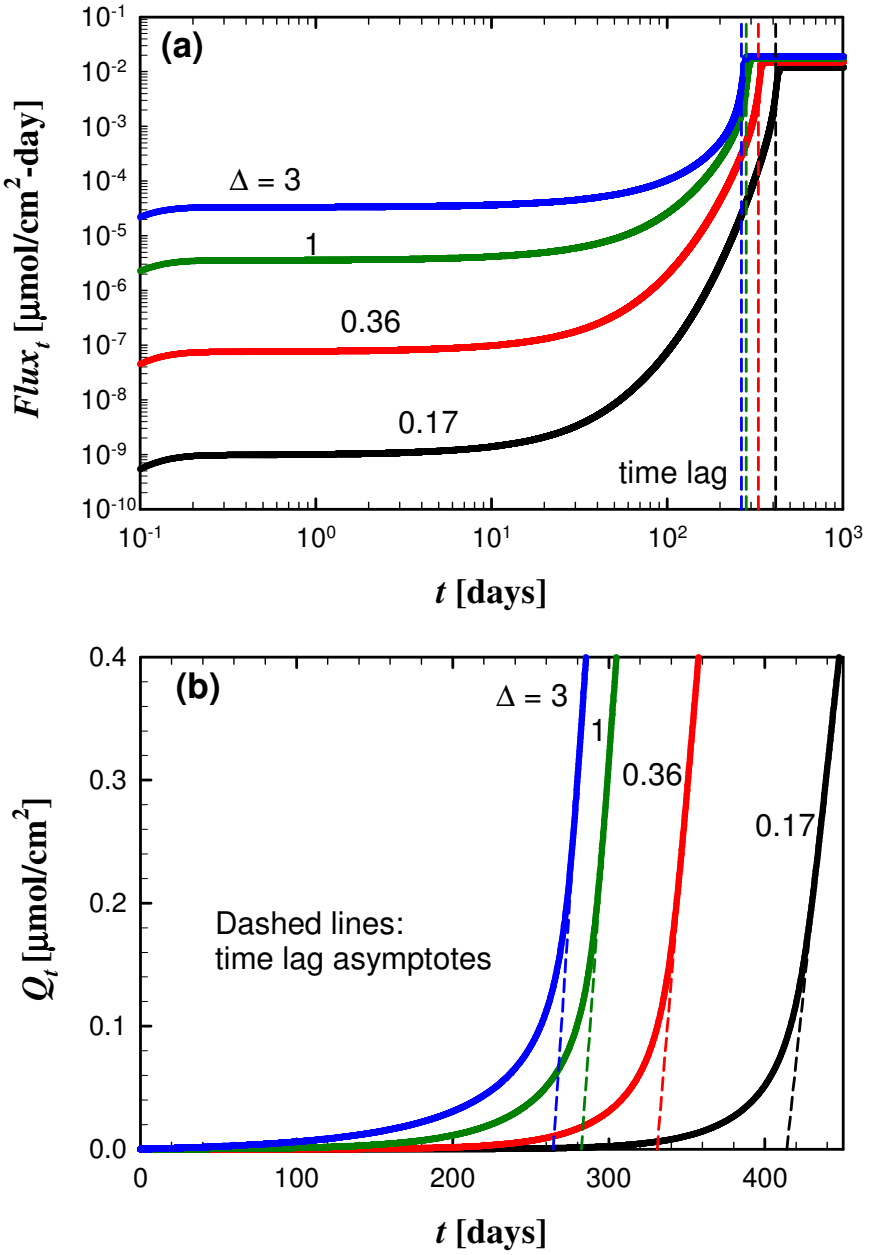

Figure 5.9: (a) Downstream flux versus time on a log-log scale and (b) permeate versus time on a linear scale for a film with three layers, with the first and last inert, varying Δ as indicated in charts. All other parameter values are given in table 5.1. The dashed lines indicate the time lag θ calculated from the numerical solution by extrapolating the asymptote $Q_{t\to\infty}$ to the time axis.

Figure 5.10 compares (a) the initial flux plateau and (b) the time lag in log scale for various combinations of Δ and volume fraction ϕ, as noted in the charts. The values were obtained by numerical solution of equations 5.3-5.6, but generally agree with the analytical predictions, as will be discussed in the next section. Increasing the volume fraction ϕ significantly magnifies the favorable effects on barrier performance (i.e., decreasing flux plateau and increasing time lag) caused by decreasing Δ. While D_M is dictated by the choice of matrix polymer (here the value corresponds to poly(ethylene terephthalate)), the value given in table 5.1 as the base case for D_R is an estimate based on initial experimental results, thus some degree of variability is expected. As the results of figures 5.9 and 5.10 show, the barrier performance of a multilayer system is significantly dependent on Δ, particularly if $\Delta < 1$, making an accurate determination of D_R critically important. The effect of Δ on time lag and initial flux plateau are both related to the effect of Δ on the diffusion time scale. Decreasing Δ increases the diffusion time scale, increasing the exposure of oxygen to the reactive sites, leading to more complete reaction and reducing the initial flux plateau. Time lag is proportional to diffusion time scale, therefore decreasing Δ increases time lag.

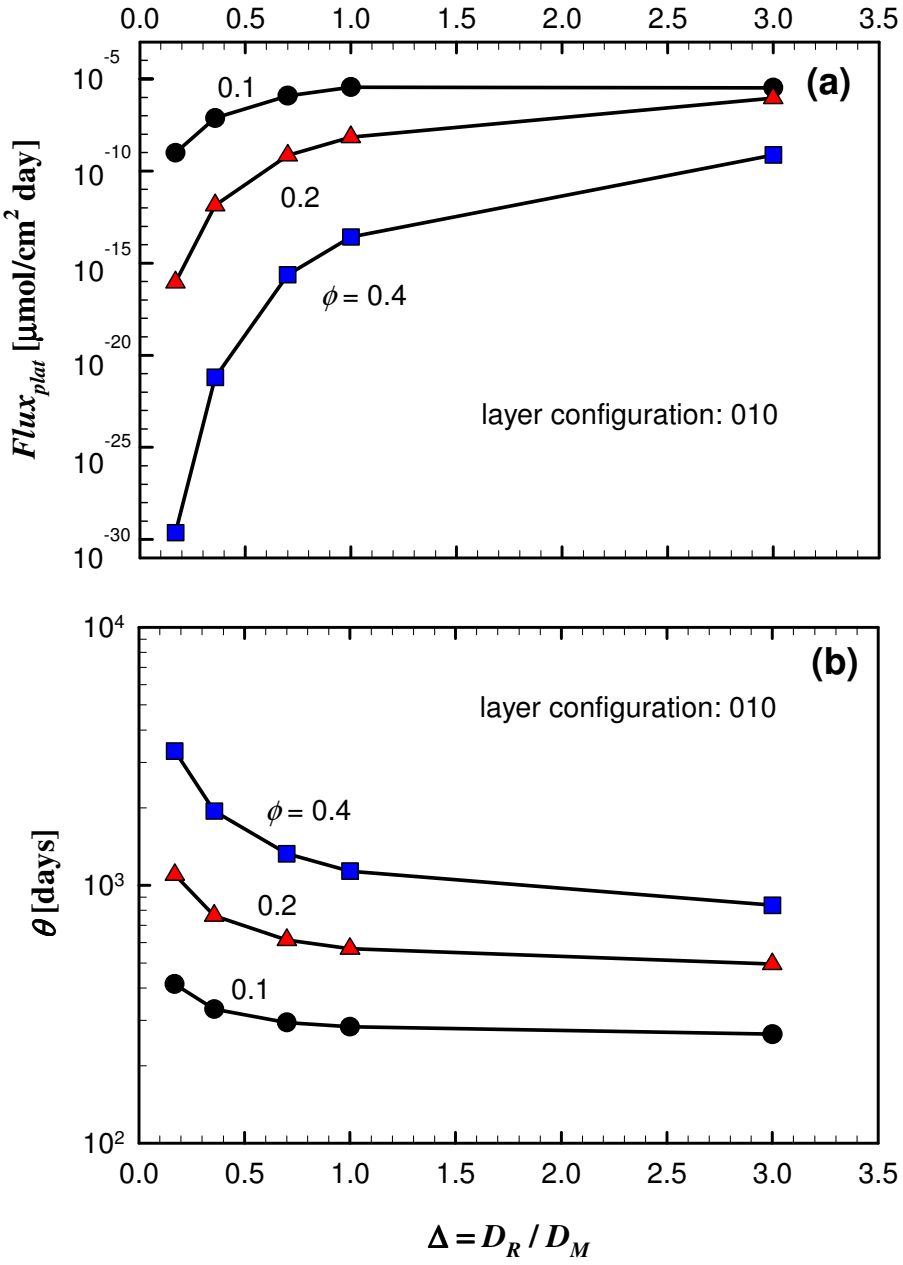

Figure 5.10: Effect of Δ and volume fraction ϕ on (a) initial downstream flux plateau and (b) time lag for a film with three layers. All other parameter values are given in table 5.1. The values for flux plateau and time lag were obtained from numerical solution of equations 5.3-5.6.

Figure 5.11 shows the downstream flux versus time on a log-log scale for varying $H = S_M / S_R$ as indicated in chart, with $\Delta = 1$ for figure 5.11a and $\Delta = 0.357$ for figure 5.11b. All other parameter values are given in table 5.1. Decreasing H decreases the initial flux plateau, which is a desirable trend, even though it causes the steady-state flux to increase. However, decreasing H also decreases time lag, which is undesirable. Decreasing Δ from 1 (figure 5.11a) to 0.357 (figure 5.11b) reduces the effect of H on the initial flux plateau and increases its effect on time lag and steady-state flux. While the effect of H on the initial flux plateau seems contradictory as it is opposite the effect of H on the steady-state flux, it makes physical sense, as the higher oxygen solubility within the reactive layers increases the amount of oxygen available to react with the scavenging sites.

Figure 5.12 compares the effect of H on (a) the initial flux plateau and (b) the time lag in log scale for three layer configurations with Δ=1 and 0.357, as shown in the charts. The values were obtained by numerical solution of equations 5.3-5.6, but generally agree with the analytical predictions, as will be discussed in the next section. As shown in figure 5.12a, reducing Δ reduces the effect of H and of the number of layers in the initial flux plateau. This trend agrees with the predictions of equation 5.27 for the initial flux plateau and the results shown in figures 5.2-5.4. Figure 5.12b shows that time lag has a linear dependence on H, as predicted by equation 5.37. Since the time lag does not depend on the number of layers when the total number is odd, only one curve is shown for each value of Δ.

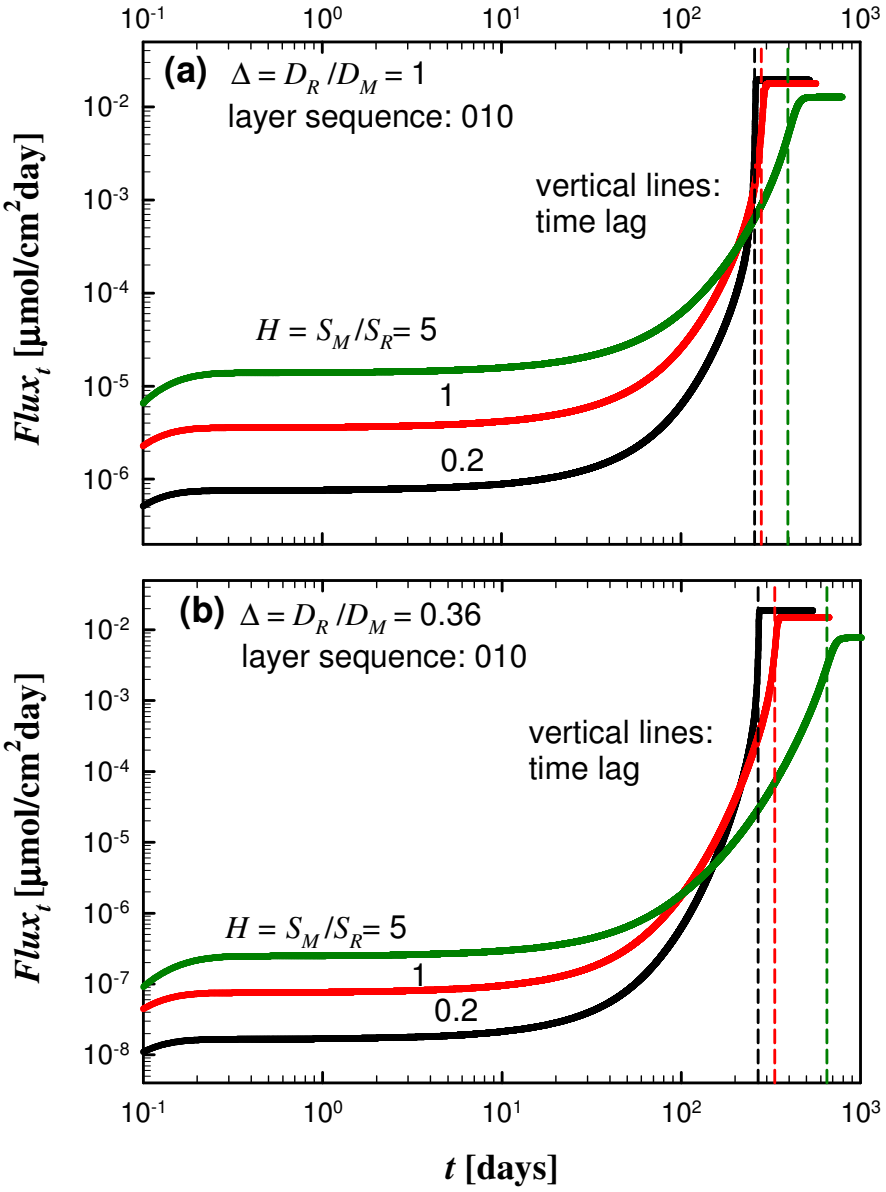

Figure 5.11: Downstream flux versus time for a film with three layers, with the first and last inert, varying H as indicated in charts. (a) $\Delta = 1$, (b) $\Delta = 0.357$. All other parameter values are given in Table 5.1. The vertical dashed lines indicate the time lag θ calculated from the numerical solution by extrapolating the asymptote $Q_{t\to\infty}$ to the time axis.

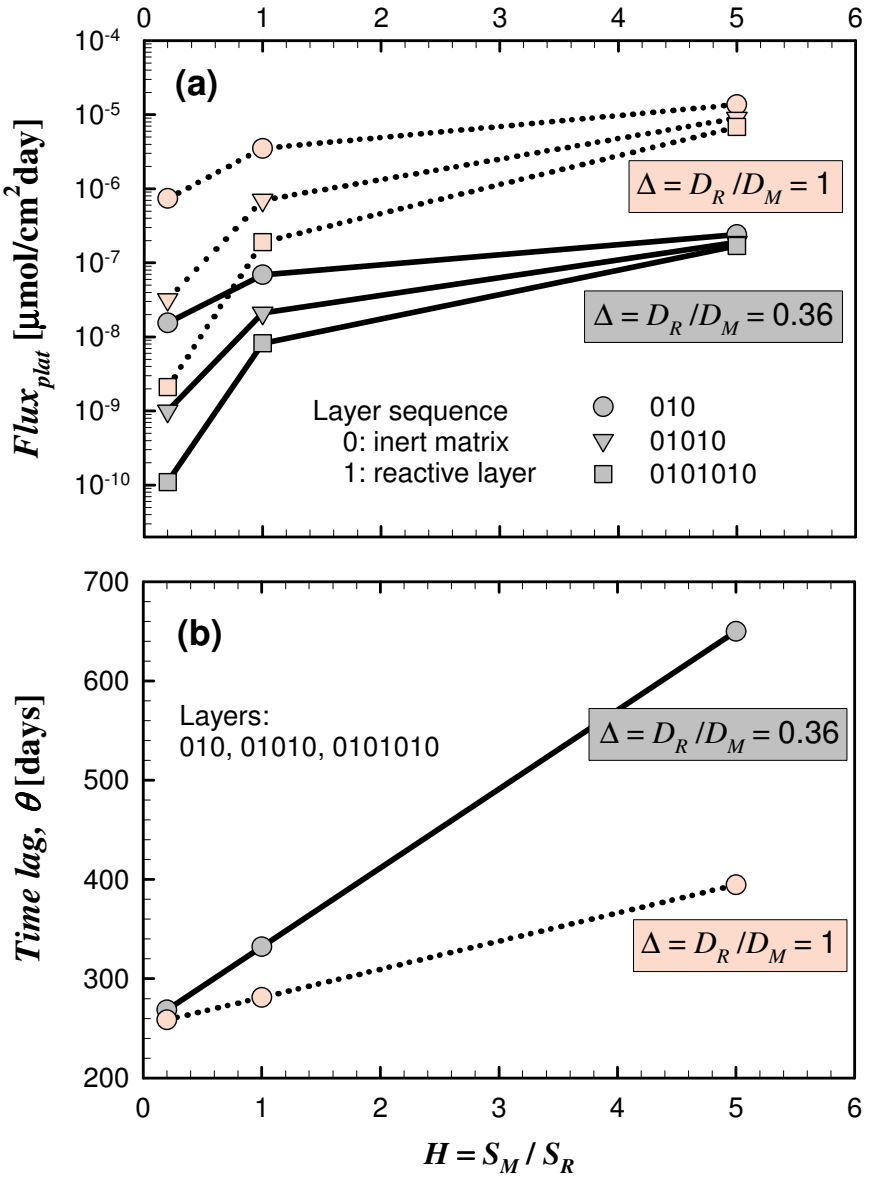

Figure 5.12: Effect of H and Δ on (a) initial downstream flux plateau and (b) time lag for films with layer configurations 010, 01010, 0101010, where 0 represents an inert matrix layer and 1 represents a reactive layer. All other parameter values are given in table 5.1. The values for flux plateau and time lag were obtained from numerical solution of equations 5.3-5.6.

5.5 COMPARISON OF ANALYTICAL PREDICTIONS AND NUMERICAL SOLUTION

Figure 5.10 compares the early-times downstream flux plateau obtained by numerical solution of equations 5.2-5.4, and the flux plateau calculated by the leading order estimate of equation 5.27. Three layer configurations are compared, as indicated in the chart, using parameters from table 5.1, except for the various combinations of ϕ, Δ and H used in the computations. The predictions agreed very well with the numerical solutions.

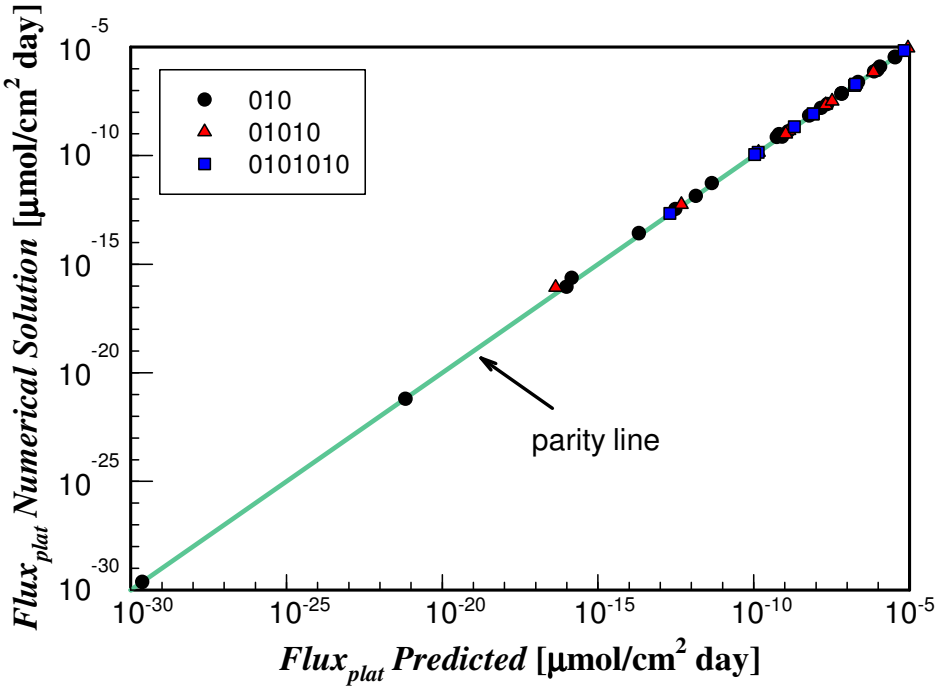

Figure 5.13: Parity chart for flux plateau comparing numerical solution and analytical prediction for three layer configurations. Layer sequence for each case indicated in chart, where 0 represents an inert matrix layer, and 1 represents a reactive layer. For all layer sequences, all permutations of H = 0.2, 1 and 5 with Δ = 0.357 and 1 (keeping ϕ = 0.1) are plotted. For the 010 layer sequence, all permutations of ϕ = 0.1, 0.2 and 0.4, with Δ = 0.17, 0.357, 0.7, 1 and 3 (keeping H = 1) are plotted. All other parameter values are given in table 5.1.

Figure 5.11 compares the time lag calculated by numerical solution with the time lag calculated by analytical prediction. All cases shown are for a film of configuration 010 using the parameter values from table 5.1, except for ϕ, Δ and H. All permutations of H = 0.2, 1 and 5 with Δ = 0.357 and 1 (keeping ϕ = 0.1) and all permutations of ϕ = 0.1, 0.2 and 0.4, with Δ = 0.17, 0.357, 0.7, 1 and 3 (keeping H = 1) are plotted. Since Δ and H were not unity for all cases, equation 5.37 was used. As shown in the graph, the analytical prediction is in excellent agreement with the numerical solution for all points calculated.

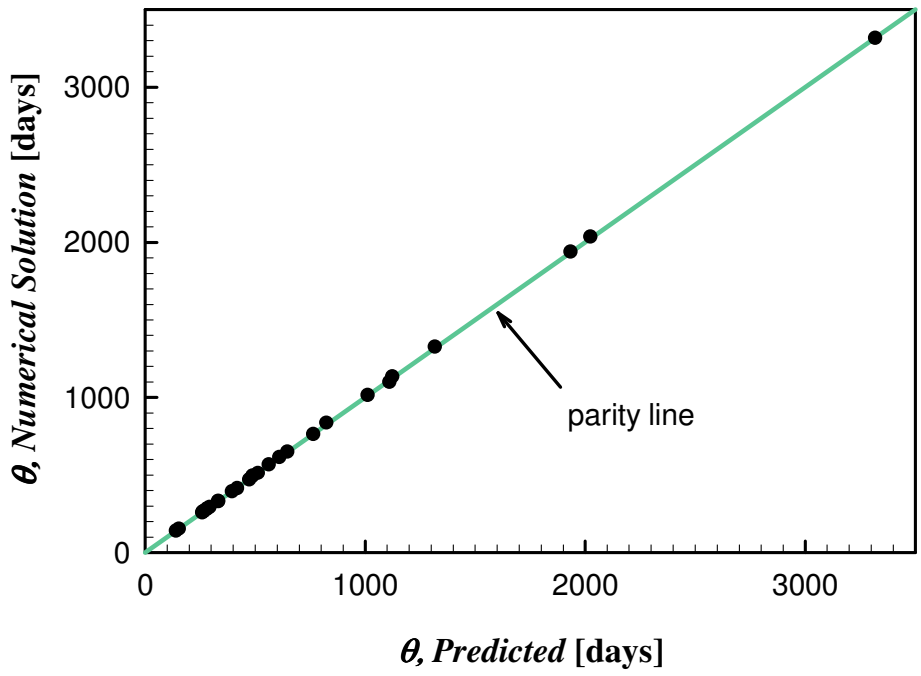

Figure 5.14: Parity chart for time lag θ comparing numerical solution and analytical prediction for a film with three layers, where the first and last layers are inert matrix. All permutations of H = 0.2, 1 and 5 with Δ = 0.357 and 1 (keeping ϕ = 0.1) and all permutations of ϕ = 0.1, 0.2 and 0.4, with Δ = 0.17, 0.357, 0.7, 1 and 3 (keeping H = 1) are plotted. All other parameter values are given in table 5.1.

5.6 SUMMARY AND CONCLUSIONS

A model has been developed to describe a multilayer composite with alternating inert matrix and reactive layers. Similarly to homogeneous films and polymer blends, multilayer films presented an initial flux plateau. However, rather than a smooth transition between the early times flux and the steady-state regime, intermediate inflexion points in the transient flux were observed, which coincided with the number of reactive layers in the film. Analytical predictions of the initial flux plateau and of time lag have been derived. Numerical solutions were computed for various layer configurations, to understand the changes in barrier properties do to configuration changes, such as number of layers and sequence. There are many nuances in the selection of the ideal system, as no configuration gave both the highest time lag and the lowest initial flux plateau. In general, however, systems where the first layer is inert outperform systems where the first layer is reactive. Numerical solutions were also computed for a base parameter set, and from many variations from it. In particular, ϕ, Δ and H were greatly explored. The results presented here will be compared in Chapter 6 with the results presented in Chapters 3 and 4 for polymer blends.

SUPPLEMENTAL MATERIAL - 5.A

The early time analysis to estimate flux plateau and the steady-state analysis to estimate time lag are extended here for layered systems with the first layer reactive, with odd or even total number of layers.

Early times analysis to estimate flux plateau

For the multilayer reactive film with the layer configuration shown in figure 5.1 where the first layer is inert matrix, the oxygen concentrations at the boundaries of the reactive layer in the i^{th} pair are defined by equations 5.22 and 5.23 for early times for the estimation of the initial flux plateau. When the total number of layers is odd, the system of equations to determine the early time concentrations is given by equation 5.22 with $i=1$ and the last equation is given by equation 5.23 with $i = N_R$. As the last layer is inert matrix, the downstream flux is calculated by substituting p_{2N_R} in equation 5.25 as discussed in the early times analysis section. When the total number of layers is even, the last equation is given by equation 5.22 with $i = N_R$. The oxygen partial pressure at the downstream boundary is $p_N = p_L = 0$ and the last layer is reactive, therefore the downstream flux is calculated by substituting p_{2N_R-1} in the downstream flux equation for the reactive layer given by

$$J\big|_L = \frac{\alpha D_R S_R}{\sinh(\alpha L_R)} p_{2N_R-1}, \tag{5.A.1}$$

where $\alpha = \sqrt{k_R n_{R,0}/D_R}$.

When the first layer is reactive, the indices for the boundary concentrations are shifted to match the layer configuration. The two repeating concentration equations that define this system are given by

$$-a\,p_{2i-3} + b\,p_{2i-2} - c\,p_{2i-1} = 0\,, \tag{5.A.2}$$

$$-c\,p_{2i-2} + b\,p_{2i-1} - a\,p_{2i} = 0\,, \tag{5.A.3}$$

where $a = S_M D_M / L_M$, $b = S_M D_M / L_M + \alpha S_R D_R \coth(\alpha L_R)$ and $c = \alpha D_R S_R / \sinh(\alpha L_R)$. Following the convention that the layer pair i consists of an inert matrix and a reactive layer in that order, the first pair in this configuration not have an inert matrix layer, therefore the first equation of the system is given by equation 5.A.3 with i=1. The complete system in matrix form is given by

$$\begin{bmatrix} b & -a & 0 & \cdots & 0 & 0 & 0 \\ -a & b & -c & \cdots & 0 & 0 & 0 \\ 0 & -c & b & \cdots & 0 & 0 & 0 \\ 0 & 0 & -a & \cdots & 0 & 0 & 0 \\ \vdots & \vdots & \vdots & \ddots & \vdots & \vdots & \vdots \\ 0 & 0 & 0 & \cdots & -c & b & -a \\ 0 & 0 & 0 & \cdots & 0 & -a & b \end{bmatrix} \begin{bmatrix} p_1 \\ p_2 \\ p_3 \\ p_4 \\ \vdots \\ p_{2N_R-3} \\ p_{2N_R-2} \end{bmatrix} = \begin{bmatrix} c\,p_{O_2} \\ 0 \\ 0 \\ 0 \\ \vdots \\ 0 \\ c\,p_N = 0 \end{bmatrix}. \tag{5.A.4}$$

If the total number of layers is odd, the last equation is given by equation 5.A.2 with $i = N_R$, and the downstream flux is given by

$$J\big|_L = \frac{\alpha D_R S_R}{\sinh(\alpha L_R)}\, p_{2N_R-2}\,. \tag{5.A.5}$$

If the total number of layers is even, the last equation is given by equation 5.A.3 with $i = N_R$, and the downstream flux is given by

$$J\big|_L = \frac{D_M S_M}{L_M} p_{2N_R-1}, \tag{5.A.6}$$

While the description above may suggest different forms of the downstream flux for different layer configurations, when the solutions for the concentrations at the boundaries are coupled with the respective flux equations, a universal expression given by equation 5.27 arises. For odd total number of layers, the number of reactive layers N_R and inert layers N_M determine the starting layer, i.e., if first layer is inert $N_M = N_R + 1$, otherwise $N_R = N_M + 1$. For even number of layers, the value of the downstream flux plateau is identical for a given total number of layers, regardless of order.

Steady-state analysis to estimate time lag

For the inert matrix layers, the concentration of reactive sites is always 0, so only the reactive layers need to be computed. Equation 5.34 gives the reactive sites term when the first layer is inert matrix. If the first layer is reactive, the integral term containing the initial concentration of reactive sites is given by

$$\int_0^L x\, n_{t=0} dx = \sum_{i=1}^{N_R} \int_{(i-1)(L_M+L_R)}^{(i-1)L_M+iL_R} x\, n_{R,0} dx = \frac{n_{R,0}}{2} N_R L_R \left[\left(N_R - 1\right) L_M + N_R L_R \right], \tag{5.A.7}$$

where $n_{R,0}$ is the initial concentration of reactive sites in each reactive layer. Substituting equation 5.A.6 in the general time lag equation 5.33 and expressing the individual layer thickness in terms of the volume fraction of reactive polymer, ϕ, and the total thickness of the film, L [$L_R = \phi L / N_R$ and $L_M = \left(1-\phi\right) L / N_M$], the time lag prediction for a

multilayer system with odd total number of layers where the first layer is reactive is given by equation 5.35. Therefore, time lag is not affected by number of layers or their order, if the total number of layers is odd. However, for even total number of layers, both ordering and number of layers are relevant. The time lag for a multilayer film which first layer is reactive and with even total number of layers ($N_R = N_M$) is given by

$$\frac{\theta_{even,1^{st}\,Reactive}}{\theta_0} = 1 + \frac{3}{\nu}\left(\frac{\phi - 1 + N_M}{N_M}\right). \tag{5.A.8}$$

If all physical parameters remain the same, except the number or layers, the minimum value of $\theta_{even,1^{st}\,Reactive}$ is achieved for a single pair of reactive and inert layers (i.e., $N_M = 1$). As the number of layers increase, the value of $\theta_{even,1^{st}\,Reactive}$ increases, until for $N_M \gg 1$ the dependence will eventually vanish, making equation 5.35 valid for all layer configurations for a large number of layers.

SUPPLEMENTAL MATERIAL - 5.B

Equations 5.3-5.6 were discretized layer by layer, using a two-point forward difference for the time derivatives and a three-point central difference for the spatial derivatives, except at the interfaces between layers. For reactive layers, the discretized equations are given by

$$\frac{S_R p_j^{m+1} - S_R p_j^m}{\Delta t} = \frac{S_R D_R \left(p_{j+1}^m - 2 p_j^m + p_{j-1}^m \right)}{\left(\Delta x \right)^2} - k_R S_R p_j^m n_j^m , \tag{5.B.1}$$

$$\frac{n_j^{m+1} - n_j^m}{\Delta t} = -\hat{v} k_R S_R p_j^m n_j^m , \tag{5.B.2}$$

$$C_j^{m+1} = S_M p_j^{m+1} , \tag{5.B.3}$$

where Δt is the time step, Δx is distance between two grid points in space, m is the index for time, and j is the index for the space grid. For the inert layers, there is no reaction, simplifying the discretized equations

$$\frac{S_M p_j^{m+1} - S_M p_j^m}{\Delta t} = \frac{S_M D_M \left(p_{j+1}^m - 2 p_j^m + p_{j-1}^m \right)}{\left(\Delta x \right)^2} , \tag{5.B.4}$$

$$n_j^{m+1} = n_j^m , \tag{5.B.5}$$

$$C_j^{m+1} = S_M p_j^{m+1} , \tag{5.B.6}$$

At the interfaces, the concentration of reactive sites is the average between the values at either side of the interface. The partial pressure is calculated by enforcing the flux continuity, using three-point backward and forward differences as appropriate. The convention for the oxygen concentration is to always use the solubility value of the

upstream layer. Thus, the discretized equations for the interface between an inert matrix upstream and a reactive layer downstream are given by

$$-D_M S_M \frac{3p_j^{m+1} - 4p_{j-1}^{m+1} + p_{j-2}^{m+1}}{2\Delta x} = -D_R S_R \frac{-3p_j^{m+1} + 4p_{j+1}^{m+1} - p_{j+2}^{m+1}}{2\Delta x}, \tag{5.B.7}$$

$$n_j^{m+1} = 0.5\left(n_{j-1}^{m+1} + n_{j+1}^{m+1}\right), \tag{5.B.8}$$

$$C_j^{m+1} = S_M p_j^{m+1}. \tag{5.B.9}$$

Likewise, the discretized equations for the interface between a reactive layer upstream and an inert matrix layer downstream are given by

$$-D_R S_R \frac{3p_j^{m+1} - 4p_{j-1}^{m+1} + p_{j-2}^{m+1}}{2\Delta x} = -D_M S_M \frac{-3p_j^{m+1} + 4p_{j+1}^{m+1} - p_{j+2}^{m+1}}{2\Delta x}, \tag{5.B.10}$$

$$n_j^{m+1} = 0.5\left(n_{j-1}^{m+1} + n_{j+1}^{m+1}\right), \tag{5.B.11}$$

$$C_j^{m+1} = S_R p_j^{m+1}. \tag{5.B.12}$$

Nomenclature

a , b , c	coefficients in concentration equations
C_0	oxygen concentration at the film's upstream boundary, μmol$_{O2}$/cm^3
C_M , C_R	O_2 concentration for inert matrix and reactive layers, respectively, μmol$_{O2}$/cm^3
D_M , D_R	oxygen diffusion coefficient for inert matrix and reactive layers, respectively, cm^2/day
H	partition coefficient, $H = S_M / S_R$, dimensionless
J	oxygen flux, μmol/cm^2 day
k_R	reaction rate constant for reactive layers, cm^3 OSP/μmol$_{RS}$ day
L	thickness of the film, cm
n	concentration of reactive sites, μmol$_{RS}$/cm^3
$n_{R,0}$	initial concentration of reactive sites in reactive layers, μmol$_{RS}$/cm^3
p_{O_2}	oxygen partial pressure, psia
Q_t	oxygen permeate, μmol/cm^2
S_M , S_R	oxygen solubility coefficient for inert matrix and reactive layers, respectively, μmol/cm^3 atm
t	time, s
x	position in film, cm

Greek letters

Δ ratio between the oxygen diffusion coefficients for the reactive and inert matrix layers, $\Delta = D_R / D_M$, dimensionless

θ time lag, day

θ_0 diffusion time lag of inert polymer, $\theta_0 = L^2 / 6D_M$, day

ϕ volume fraction of OSP in multilayer composite, dimensionless

Φ_R Thiele modulus for the reactive layers, $\Phi_R = \sqrt{\left(N_R L_R\right)^2 k_R \, n_{R,0} / D_R}$, dimensionless

ν ratio between dissolved oxygen and reactive capacity, $\nu = \hat{\nu} C_0 / \phi \, n_{R,0}$, dimensionless

$\hat{\nu}$ stoichiometric coefficient, $\mu\text{mol}_{\text{RS}} / \mu\text{mol}_{\text{O2}}$

Chapter 6: Comparative Study of Reactive Barrier Structures

6.1 INTRODUCTION

This chapter compares three reactive barrier configurations, namely homogeneous films, polymer blends and multilayer composite, illustrated in figure 6.1, to aid in the selection of the most suitable configuration for a particular application.

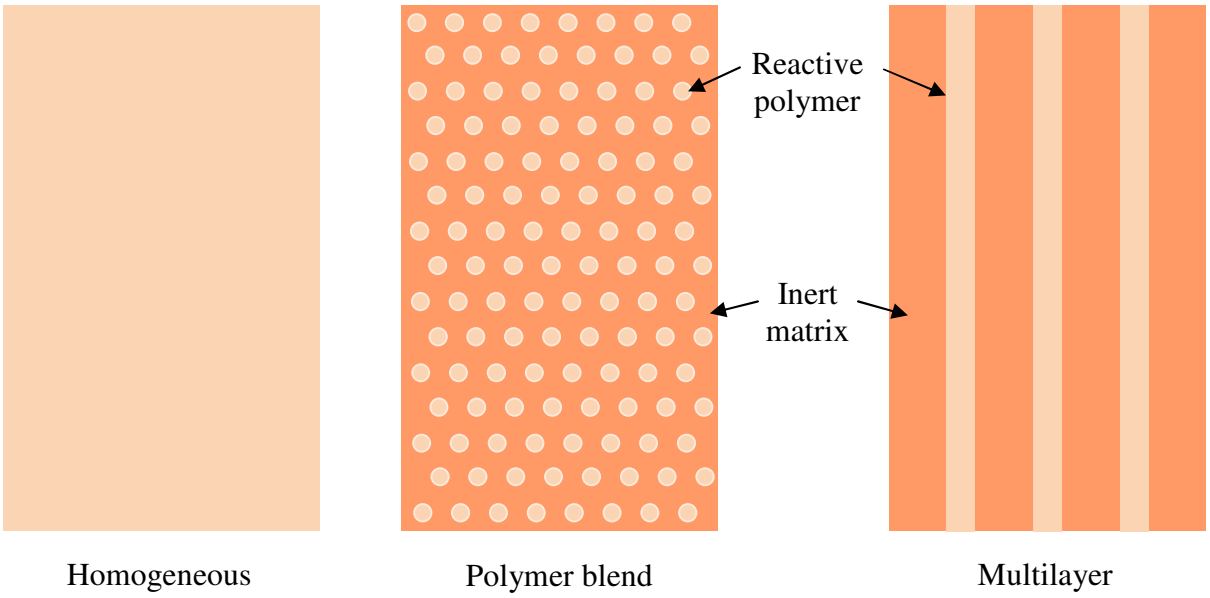

Figure 6.1: Schematic illustration of the three types of reactive barrier films being studied.

The homogeneous model represents a pure film of a reactive polymer where the immobile reactive sites are confined to the molecular structure of the polymer and a single polymer phase is present. The homogeneous model can also be used to approximate polymer blends, or films where inorganic reactive particles have been

uniformly dispersed within the film. The polymer blend consists of reactive polymer particles uniformly dispersed within an inert polymer matrix. Finally, the multilayer film consists of multiple alternating inert matrix and reactive polymer layers.

6.2 MODEL COMPARISON

Table 6.1 summarizes the one-dimensional models developed in previous chapters for the homogeneous film, the polymer blend and the multilayer film. All models are based on the material balances for the mobile species [of concentration $C(x,t)$ for homogeneous and multilayer films, and $C_m(x,t)$ for blends] and immobilized reactive sites [of concentration $n(x,t)$]. The rate of change in the concentration of mobile species is balanced with diffusive and reactive contributions. On the other hand, since the reactive species are immobilized, the rate of change in concentration is due to reaction only. For polymer blends, the details of the reaction model within the particles are incorporated in the composite model. For comparison purposes, this chapter focuses on the model for spherical particles. For the multilayer films, the general model is similar to the homogeneous film. However, the diffusion coefficient $D(x)$ is allowed to be different for inert [$D(x) = D_M$] or reactive layers [$D(x) = D_R$], and the initial concentration of reactive sites for each layer is set accordingly, i.e., $n(x,0) = 0$ for inert layers and $n(x,0) = n_{R,0}$ for reactive layers.

Table 6.1: Summary of model equations for homogeneous, polymer blend and multilayer films in dimensional terms.

Homogeneous	**Polymer blend**	**Multilayer film**
$\frac{\partial C}{\partial t} = D\frac{\partial^2 C}{\partial x^2} - k_R\, C\, n$	$\frac{\partial C_m}{\partial t} = D_m \frac{\partial^2 C_m}{\partial x^2} - \frac{3k_p\phi}{R}\frac{C_m}{H} f$	$\frac{\partial C}{\partial t} = \frac{\partial}{\partial x}\left(D\frac{\partial C}{\partial x}\right) - k_R\, C\, n$
$\frac{\partial n}{\partial t} = -\hat{v}\, k_R\, C\, n$	$\frac{\partial n}{\partial t} = -\frac{3k_p\hat{v}}{R}\frac{C_m}{H} f$	$\frac{\partial n}{\partial t} = -\hat{v}\, k_R\, C\, n$
	$f = \frac{n^{2/3}/n_{p,0}^{\,2/3}}{1+\Phi_p\left(1-\frac{n^{1/3}}{n_{p,0}^{\,1/3}}\right)\frac{n^{1/3}}{n_{p,0}^{\,1/3}}}$,	Inert layers: $D = D_M$, $n(x,t) = 0$
	$H = \frac{S_m}{S_p}$, $\Phi_p = \sqrt{\frac{R^2 k_R\, n_{p,0}}{D_p}}$	Reactive layers: $D = D_R$, $n(x,0) = n_{R,0}$
I.C.:	I.C.:	I.C.:
$C(x,0) = 0$,	$C_m(x,0) = 0$,	$C(x,0) = 0$,
$n(x,0) = n_0$	$n(x,0) = n_{p,0}$	$n(x,0) = \phi\, n_{R,0}$
B.C.:	B.C.:	B.C.:
$C(0,t) = C_0$,	$C_{m,0} \equiv C_m(0,t) = S_m\ p_{O_2}$,	$C(0,t) = C_0$,
$C(L,t) = 0$	$C_{m,L} \equiv C_m(L,t) = 0$	$C(L,t) = 0$

The oxygen flux and the total amount of oxygen permeated are quantities of interest derived from the solution of the model equations given in table 6.1. The downstream flux J at time t is given by

$$J\big|_{x=L} = -\left(D\frac{\partial C}{\partial x}\right)\Big|_{x=L}, \tag{6.1}$$

where D is replaced with the proper constant or variable coefficient, according to table 6.1. The total oxygen permeated through the membrane Q_t at time t is given by

$$Q_t = \int_0^t J\big|_{x=L}\, dt\,. \tag{6.2}$$

It should be noted that in the blend model, the physical effects of the particles on the oxygen diffusion process have been ignored. In the extreme case of $\Delta \ll 1$, the particles might be considered impermeable in which case Maxwell's equation (Maxwell 1872) would predict the relationship between the steady-state permeability of the blend, P_{blend}, to that of the matrix, P_m

$$\frac{P_{blend}}{P_m} = \frac{1-\phi}{1-\phi/2}, \tag{6.3}$$

which for ϕ = 0.1 and 0.2 amount to a reduction of 5.5% and 11% respectively for the blend. On the other hand, for the layer films the physical effects are built in the model, and since layers provide resistance to transport in series, the difference in permeability for each layer significantly affects the end results, as will be discussed in the following sections. As discussed in Chapter 5, the effective steady-state permeability of the multilayer composite, $P_{multilayer}$, is obtained by the well known additive relation between the resistance to flux in each layer (Crank 1975)

$$\frac{L}{P_{multilayer}} = \sum_{i=1}^{N} \frac{L_i}{P_i} = \frac{\phi L}{P_R} + \frac{(1-\phi)L}{P_M}, \tag{6.4}$$

where $P_M = S_M D_M$ and $P_R = S_R D_R = S_M D_M \Delta / H$; and the steady-state flux for a multilayer film exposed to p_{O_2} at the upstream boundary, and with vanishing oxygen partial pressure at the downstream boundary is given by

$$J_{SS} = \frac{P p_{O_2}}{L} = \frac{\Delta D_M S_M p_{O_2}}{L\left[\phi H + \Delta(1-\phi)\right]}. \tag{6.5}$$

Table 6.2 lists all parameters and values used in the comparison. It is important to make a distinction between using the homogeneous reactive membrane model to approximate a polymer blend film versus modeling a homogeneous film made of the reactive polymer. As shown in Carranza et al. (2010), in the moving front regime the effective surface reaction rate k_p can be calculated in terms of the bulk reaction rate k_R, i.e., $k_p = \sqrt{D_p k_R n_{p,0}}$. The diffusion coefficient of the reactive particles should be used for reactive layers, i.e. $D_R = D_p$, and the diffusion coefficient of the blend matrix should be used for the inert matrix layers, i.e., $D_M = D_m$. This approach makes the comparison between the polymer blend and multilayer films possible, as the equivalent bulk rate constant can be used for the reactive layers of the multilayer composite, which will be discussed next. On the other hand, to use the homogeneous reactive membrane model to approximate a polymer blend film with equivalent barrier properties, the value of the diffusion coefficient for the inert matrix in the polymer blend was used in the homogeneous model, i.e., $D = D_m$; the initial concentration of reactive sites for the homogeneous model was based on the volume fraction and initial concentration of sites within the particle , i.e., $n_0 = \phi n_{p,0}$; and the bulk reaction rate for the homogeneous film was selected by matching the homogeneous reactive time scale $\tau_{rxn,H} = 1/k_R n_0$ to the effective reactive time scale for the blend, $\tau_{rxn,b} = HR/3\phi k_p$. This matching approach is useful to estimate the initial flux plateau and time lag of a multilayer system where the reactive layers are blended polymers, without the need to develop a rather complex model.

Table 6.2: List of parameters for comparison between homogeneous, blend and multilayer film. All values except for the rate constant k_R match the values used as the base case for the polymer blend calculations in Chapter 3. The values in parenthesis are given in the units used in Chapter 3.

Name	**Symbol**	**Value**
Total film thickness	L	0.025 cm (250 μm)
Volume fraction of reactive layers or particles	ϕ	0.1
Initial concentration of reactive sites in reactive layers or particles	$n_{R,0}$ for reactive layers $n_{p,0}$ for reactive particles	8000 μmol$_{RS}$/cm^3 (8x10^{-3} mol$_{RS}$/cm^3)
Initial concentration of reactive sites in homogeneous film	$n_0 = \phi n_{p,0}$ to match content of blend	800 μmol$_{RS}$/cm^3 (8x10^{-4} mol$_{RS}$/cm^3)
Stoichiometric coefficient	$\hat{\nu}$	2 μmol$_{RS}$/ μmol$_{O2}$
Oxygen solubility coefficient for the inert matrix layers or inert matrix in blend	S_M for inert matrix layer S_m for inert matrix in polymer blend	4.38 μmol$_{O2}$/cm^3 atm (0.098 cm^3(STP)/cm^3 atm)
Oxygen diffusion coefficient for the inert matrix layers or inert matrix in blend	D_M for inert matrix layer D_m for inert matrix in polymer blend	4.84x10^{-4} cm^2/day (5.6x10^{-9} cm^2/sec)
Oxygen solubility coefficient for the reactive layers or particles	S_R for reactive layers S_p for reactive particles	4.38 μmol$_{O2}$/cm^3 atm (0.098 cm^3(STP)/cm^3 atm)
Oxygen diffusion coefficient for the reactive layers or particles	D_R for reactive layers D_p for reactive particles	1.73x10^{-4} cm^2/day (2x10^{-9} cm^2/sec)
Bulk reaction rate constant for reactive layers	k_R	0.42 cm^3/ μmol$_{RS}$ day
Surface reaction rate constant for particles	$k_p = \sqrt{D_p k_R n_{p,0}}$ to match the rate for multilayer film	0.76 cm/day (8.8x10^{-6}cm/s)
Bulk reaction rate constant for homogeneous film	$k_R = 1/n_0 \tau_{rxn,b}$ to match blend's effective time scale	1.14 cm^3/ μmol$_{RS}$ day

6.3 PERFORMANCE COMPARISON

Figure 6.2 compares the transient flux for the homogeneous and polymer blend model. As discussed in Chapters 2-4, three regimes can be observed in the transient downstream flux for reactive homogeneous membranes and polymer blends. For early times, there is a quasi-steady-state flux plateau, followed by an intermediate region when the downstream flux increases until it eventually transitions to the steady-state values, characterized by the time-lag.

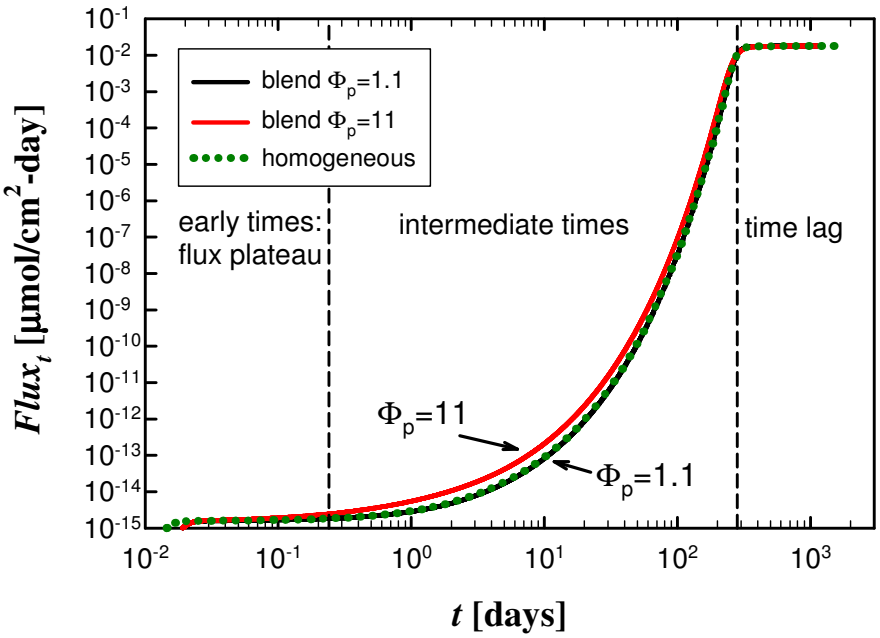

Figure 6.2: Oxygen downstream flux versus time for blend films with $\Phi_p = R\,k_P / D_P$ = 0.4 and 11 (solid lines), and a homogeneous film (dotted line). All parameter values are given in table 6.2, except D_P = 1.73x10^{-5} cm^2/day for the case of Φ_P=11. The vertical dashed lines indicate the beginning of the intermediate times regime (t_{SF}) and time lag (θ).

In general, if parameters are chosen so that reactive capacity, reactive time scale and diffusion are matched, the results for homogeneous and blend films are very similar,

matching the downstream flux at early times, the downstream flux at steady state, and the value of time lag, as illustrated in figure 6.2. The key difference is a small deviation during intermediate times, which becomes more pronounced for larger values of Φ_p. Note that the only way to vary Φ_p in the polymer blend without affecting any other parameter groups is by changing the diffusion coefficient of the reactive particle, D_p, which is not represented in any way in the homogeneous film.

Table 6.3: Summary of analytical prediction equations for homogeneous, polymer blend and multilayer reactive films.

Configuration	**Initial flux plateau**	**Time lag**
Homogeneous	$J_{pl} = 2J_{SS}\Phi_H\, e^{-\Phi_H}$, $J_{SS} = C_0 D/L$, $\Phi_H = \sqrt{k_R\, n_0 L^2/D}$	$\theta = \theta_0(1+3/\nu)$, $\theta_0 = L^2/6D$, $\nu = \hat{\nu}\, C_0/n_0$
Polymer blend, spherical particles	$J_{pl} = 2J_{SS}\Phi_b\, e^{-\Phi_b}$, $J_{SS} = C_{m,0} D_m/L$, $\Phi_b = \sqrt{3\phi\, k_p L^2/D_m R H}$, $H = S_m/S_p$	$\theta = \theta_0(1+3/\nu)$, $\theta_0 = L^2/6D_m$, $\nu = \hat{\nu}\, C_{m,0}/\phi\, n_{p,0}$
Multilayer, first and last inert*	$J_{pl} = \dfrac{2^{N_R}\Delta D_M S_M\, p_{O_2}\Phi_R e^{-\Phi_R}}{H\phi L(1+\gamma/N_M)^{N_M-N_R+1}(2+\gamma/N_M)^{N_R-1}}$, $\Phi_R = \sqrt{(\phi L)^2\, k_R\, n_{R,0}/D_R}$, $\Delta = D_R/D_M$, $\gamma = \Phi_R\Delta(1-\phi)/\phi H$, $H = S_M/S_R$	$\theta = \theta_{0,eff}(1+3/\nu)$, $\theta_{0,eff} = L^2/6D_{eff}$, $\nu = \hat{\nu} S_M\, p_{O_2}/\phi\, n_{R,0}$, $D_{eff} = \dfrac{\Delta D_M}{H\phi+\Delta(1-\phi)}$

*The flux plateau estimate shown is valid for all layer configurations discussed in Chapter 5. However, the time lag prediction shown is only valid for odd total layers. See time lag prediction equations for other layer configurations in Chapter 5.

Table 6.4: Intermediate times ($t_{SF} < t < \theta$) prediction for homogeneous and blend films.

Homogeneous	**Polymer blend**
$J\big\|_{x=L} = b\,J_{SS}\left(L/x_F\right)e^{-\Phi_H(1-x_F/L)}$, $t_{SF} = \tau_{rxn,H}/2\nu$, $\theta = \theta_0(1+3/\nu)$	$J\big\|_{x=L} = bJ_{SS}\left(L/x_F\right)e^{-\Phi_b(1-x_F/L)}$ $t_{SF} = \tau_{rxn,b}/2\nu$, $\theta = \theta_0(1+3/\nu)$
$J_{SS} = C_0 D/L$, $\Phi_H = \sqrt{k_R\, n_0 L^2/D}$, $x_F = \sqrt{2\nu\, Dt}$, $\nu = \hat{\nu}\, C_0/n_0$, $\tau_{rxn,H} = 1/k_R n_0$, $b = 0.653$	$J_{SS} = C_{m,0} D_m/L$, $\Phi_b = \sqrt{3\phi\, k_p L^2/D_m R\, H}$, $x_F = \sqrt{2\nu\, D_m t}$, $\nu = \hat{\nu}\, C_{m,0}/\phi\, n_{p,0}$, $H = S_m/S_p$, $\tau_{rxn,b} = HR/3\phi k_p$, b depends on $\Phi_p = R\,k_P/D_P$

Figure 6.3 compares the transient behavior of a reactive polymer blend to multilayer composites of configuration 010 and 01010, as indicated in charts. In the layer sequence, 0 indicates an inert layer and 1 indicates a reactive layer. Similarly to homogeneous films and polymer blends, multilayer films presented an initial flux plateau. However, rather than a smooth transition between the early times flux and the steady-state regime, intermediate inflexion points in the transient flux were observed, coinciding with the number of reactive layers in the film. As discussed in Chapter 5, layering improves the early times performance of the barrier film, in some cases by a few orders of magnitude. However, at intermediate times the influence of layering all but vanishes. The time lag for the multilayer films is longer than for blends whenever $\Delta < 1$, as it is the case for figure 6.3. However, since the initial flux plateau is so much lower for the blend than the multilayer films, in this particular case the blend will outperform the layered films for most of its useful life.

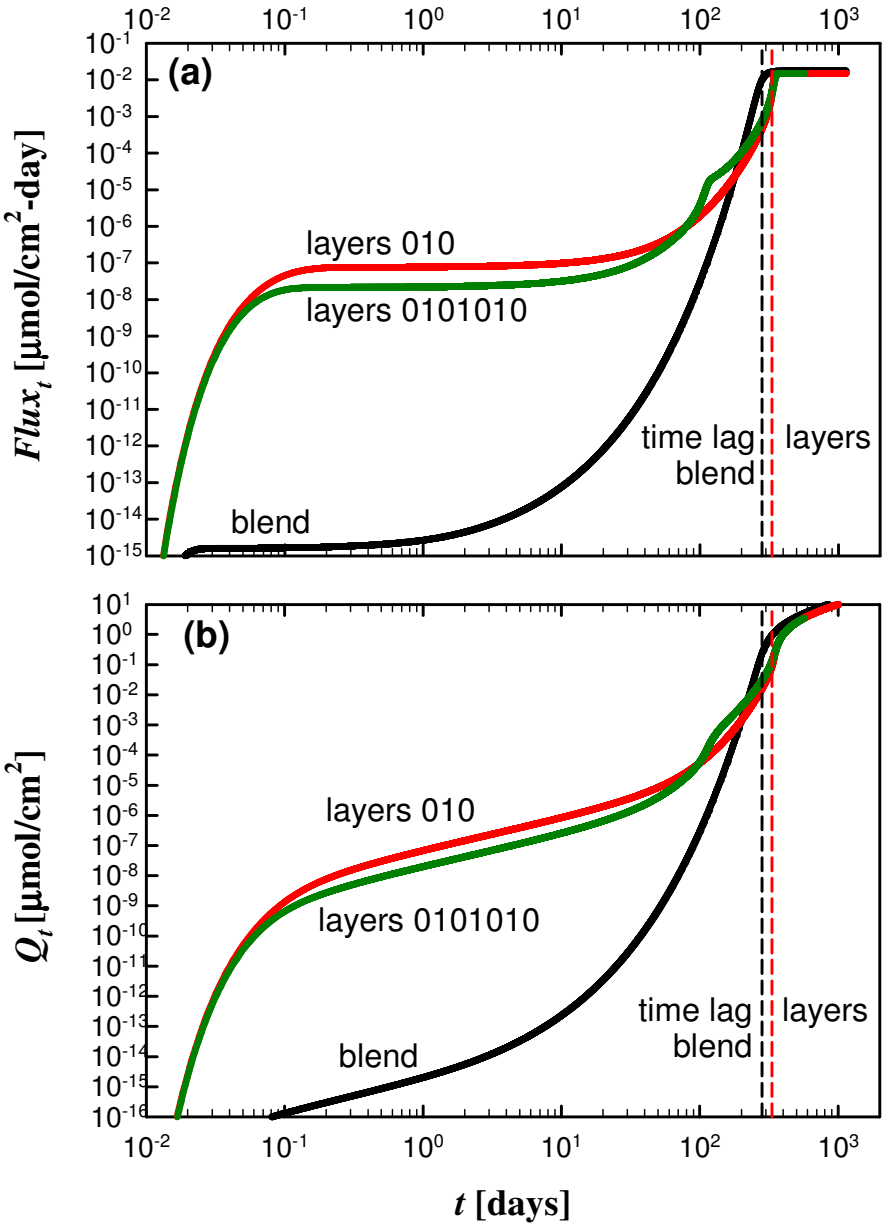

Figure 6.3: (a) Downstream flux and (b) oxygen permeate versus time in log-log scale. A polymer blend is compared to multilayer films of configuration 010 and 01010, where 0 represents an inert layer, and 1 represents a reactive layer. The vertical dashed lines indicate time lag θ for each case. All parameter values are given in table 6.2. Note that $\Delta = D_p / D_m = D_R / D_M = 0.357$.

Figure 6.4 uses the analytical expressions developed in Chapters 4 and 5 for blends and multilayer films, summarized in table 6.3, to compute initial flux plateau (figure 6.4a) and time lag (figure 6.4b) when Δ is varied. Only configuration 010 is presented in this comparison, which reduces the initial flux plateau prediction to

$$J_{pl} = \frac{2\Delta D_M S_M p_{O_2} \Phi_R e^{-\Phi_R}}{H\phi L\left(1+\gamma/2\right)^2}. \tag{6.6}$$

The multilayer flux plateau is evaluated for two bulk reaction rates (k_R=0.42 and 4.2 $cm^3/\mu mol_{RS}$ day, as indicated). The surface reaction rate for the blend is given by $k_p = \sqrt{k_R D_p n_{p,0}}$, to match each data point. All other parameter values are the same for the blend and multilayer films and are given in Table 6.2. Note that since time lag is independent of reaction rate, for the blend the time lag is the same for all cases, and for the multilayer film, only one value is required for each Δ. Note that the blend model neglects the small contribution of the blend particles to the effective permeability of the blend. In the worse case, considering the particles to be impermeable, equation 6.3 would apply, giving ~5% reduction in permeability for ϕ=0.1. On the other hand, the effect of Δ on the initial flux plateau and time lag for a multilayer film can be quite significant. For time lag, it is a simple relation that incorporates the effective diffusion coefficient for the multilayer composite. If Δ=1, the multilayer film and blend have the same time lag, otherwise, lowering Δ increases the time lag for the multilayer film, as illustrated in figure 6.4b.

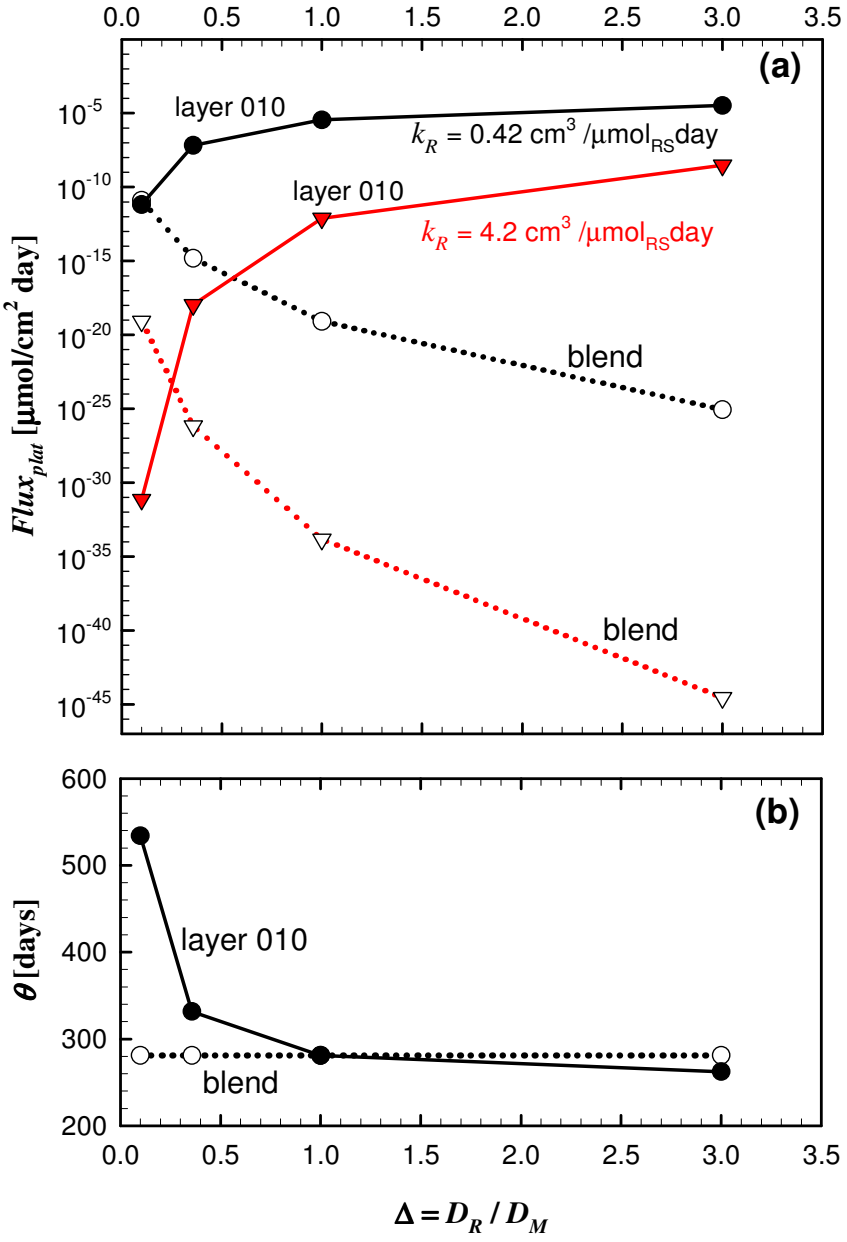

Figure 6.4: Comparison of (a) downstream flux plateau in log scale and (b) time lag θ in linear scale as a function of Δ, for a film with three layers versus a polymer blend (analytical predictions). For (a) the multilayer plateau is evaluated for two bulk reaction rates (k_R = 0.42 and 4.2 cm^3/μmol$_{RS}$ day, as indicated). The surface reaction rate for the blend is given by $k_p = \sqrt{k_R D_p n_{p,0}}$, to match each data point. All other parameter values are the same for the blend and multilayer films and are given in Table 6.2. Note that since time lag is independent of reaction rate, only one value is required for each Δ.

The initial flux plateau, which is shown in figure 6.4a on a log scale, is extremely dependent on Δ for both blends and multilayer films, and its effect is magnified by increasing the bulk rate constant k_R. For multilayer films, decreasing Δ decreases the flux plateau (by orders of magnitude), while for polymer blends, the opposite is observed. The opposite effect can be explained by looking at the flux plateau equation for the blend, $J_{pl} = 2J_{SS}\Phi_b e^{-\Phi_b}$, where $\Phi_b = \sqrt{3\phi k_p L^2 / D_m R H}$, and the effective surface rate given by $k_p = \sqrt{k_R D_p n_{p,0}}$. When all other parameters are keep the same, decreasing $\Delta = D_p / D_m$ decreases the surface reaction, thus causing the initial flux plateau to increase. This behavior can also be explained physically: if the diffusion coefficient for the reactive particle D_p is much smaller than the diffusion coefficient for the inert matrix D_m, then there will be a greater resistance for oxygen to diffuse into the particles and reach the all the reactive sites. For multilayer films, on the other hand, since the reactive and inert matrix layers are in series, slower diffusion enables oxygen to react with the immobilized sites before moving through the film. While for time lag there is a clear separation between blends and multilayer at $\Delta = 1$, consideration of the initial flux plateau requires looking at other parameters, such as the reaction rate. As illustrated in figure 6.4a, layers are favored by $\Delta \ll 1$, but higher reaction rates shift the trade point towards $\Delta = 1$.

Figure 6.5 shows the effect of the partition coefficient $H = S_M / S_R$ on the downstream flux (6.5a) and time lag (6.5b) for two values of the bulk rate constant k_R, as in figure 6.4. Here Δ is kept constant at 0.357.

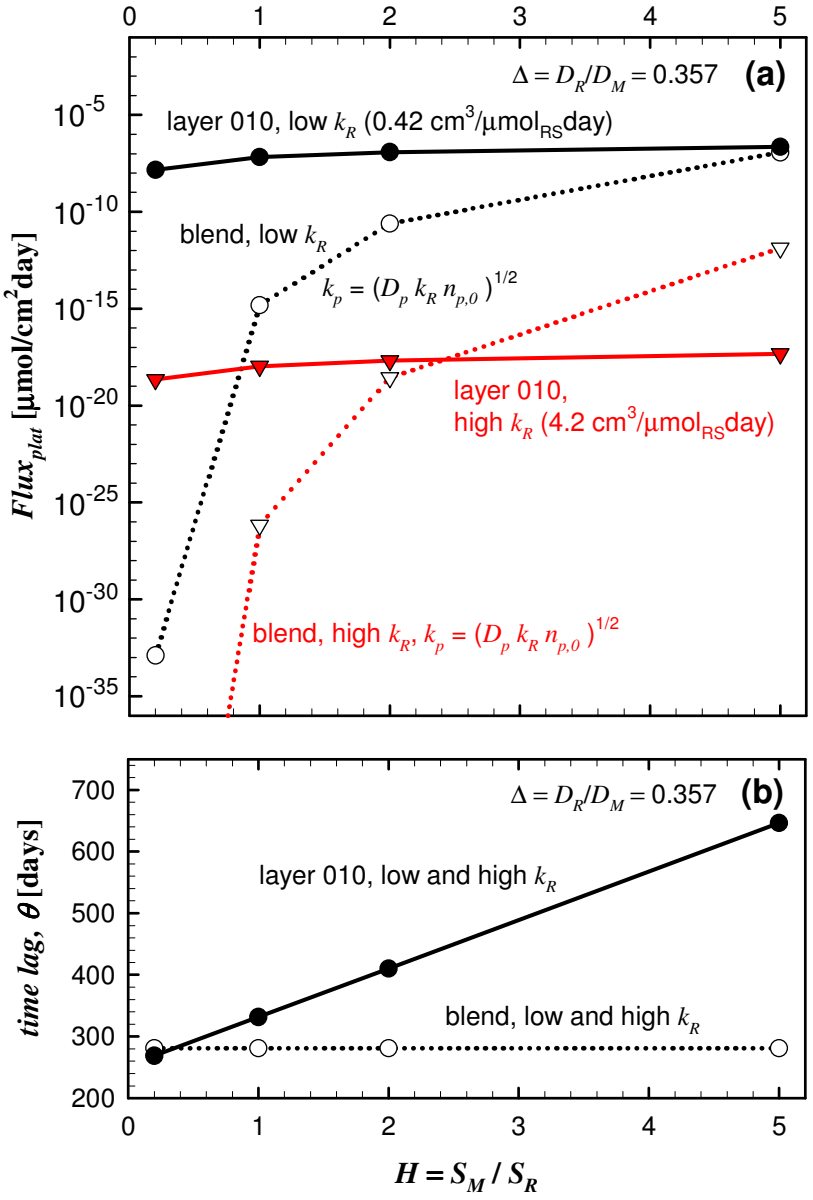

Figure 6.5: Comparison of (a) downstream flux plateau in log scale and (b) time lag θ in linear scale as a function of H, for a film with three layers versus a polymer blend (analytical predictions). For (a) the multilayer plateau is evaluated for two bulk reaction rates (k_R=0.42 and 4.2 $cm^3/\mu mol_{RS}$ day, as indicated). The surface reaction rate for the blend is given by $k_p = \sqrt{k_R D_p n_{p,0}}$, to match each data point. All other parameter values are the same for the blend and multilayer films and are given in Table 6.2. Note that since time lag is independent of reaction rate, only one value is required for each H.

For multilayer films, varying H from 0.2 to 5 causes the initial flux plateau to increase approximately one order of magnitude, while for polymer blends the increase is of many orders of magnitude, as illustrated in figure 6.5a. The time lag for a polymer blend is independent of H while for the multilayer film, it has a linear dependence, increasing as H increases (see time lag equations in table 6.3).

In summary, reactive polymers with small bulk reaction rates, large diffusion and solubility coefficients (relative to the inert matrix) favor polymer blends, while reactive polymers with large bulk reaction rates and slow diffusion rates and lower solubility coefficients favor multilayer configurations. To identify the parameter values for the limiting cases where blend outperforms multilayer or vice-versa, the analytical predictions summarized in table 6.3 can be used, without the need to numerically solve non-linear partial differential equations for each case.

6.4 SUMMARY AND CONCLUSIONS

Models developed in previous chapters for reactive barriers consisting of homogeneous films, polymer blends and multilayer composites were summarized and compared in this chapter. Differences and similarities were highlighted, to enable comparison of the different barrier configurations. The barrier performance of reactive polymer blends and multilayer films was compared, discussing the scenarios when it is more advantageous to use blends or multilayer films.

The selection between polymer blends and multilayer films depends on the properties of both the inert matrix and the reactive polymer. When the diffusion and/or solubility coefficients of the reactive material are greater than the diffusion and/or

solubility coefficients of the inert matrix, polymer blends are the most suitable choice, both in terms of time lag and initial flux plateau. On the other hand, multilayer films are more suitable for reactive materials with small diffusion and solubility coefficients relative to the matrix, particularly for higher bulk reaction rates. The analytical predictions developed in Chapters 4 and 5 can be used to perform parametric studies for other parameter spaces, enabling the selection of the most suitable configuration for a particular application, obviating the need to numerically solve the partial differential equations for each case.

Nomenclature

C	oxygen concentration in the homogeneous film, $\mu mol_{O2}/cm^3$
C_m , C_p	oxygen concentration in the polymer blend and reactive particle, respectively, $\mu mol_{O2}/cm^3$
C_M , C_R	O_2 concentration for inert matrix and reactive layers, respectively, $\mu mol_{O2}/cm^3$
D_m , D_p	oxygen diffusion coefficient of the blend inert matrix and the reactive particles, respectively, cm^2/s
D_M , D_R	oxygen diffusion coefficient for inert matrix and reactive layers, respectively, cm^2/day
H	partition coefficient, $H = S_m / S_p$ for polymer blend, $H = S_M / S_R$ for multilayer films, dimensionless
J	oxygen flux, $\mu mol/cm^2$ day
k_p	reaction rate constant for reactive particle, cm/day
k_R	reaction rate constant for homogeneous films or reactive layers, cm^3 OSP/μmol_{RS} day
L	thickness of the film, cm
n	concentration of reactive sites, $\mu mol_{RS}/cm^3$
$n_{R,0}$	initial concentration of reactive sites in reactive layers, $\mu mol_{RS}/cm^3$
p_{O_2}	oxygen partial pressure, psia
Q_t	oxygen permeate, $\mu mol/cm^2$

R radius of the OSP particle, cm

S_m, S_p solubility coefficient for oxygen in the blend inert matrix and scavenging polymer particles, μmol/cm^3 atm

S_M, S_R oxygen solubility coefficient for inert matrix and reactive layers, respectively, μmol/cm^3 atm

t time, day

x position along film thickness, cm

x_F moving front position, cm

Greek letters

β OSP capacity, $\beta = n_0/\hat{v}$, mol$_{O2}$/cm^3 OSP

θ time lag, day

θ_0 diffusion time lag of inert polymer, $\theta_0 = L^2/6D$, for homogeneous films, $\theta_0 = L^2/6D_m$ for blends, and $\theta_0 = L^2/6D_{eff}$ for multilayer films, day

ϕ volume fraction of reactive polymer in polymer blend and in multilayer films, dimensionless

Φ_b effective Thiele modulus for the blend, $\Phi_b = \sqrt{3\phi k_p L^2/D_m R H}$, dimensionless

Φ_H Thiele modulus for homogeneous film, $\Phi_H = \sqrt{L^2 k_R n_0/D}$, dimensionless

Φ_p Thiele modulus for the OSP particle, $\Phi_p = Rk_p/D_p$, dimensionless

Φ_R Thiele modulus for reactive layers, $\Phi_R = \sqrt{(\phi L)^2 k_R n_{R,0}/D_R}$, dimensionless

ν ratio between dissolved oxygen and reactive capacity, $\nu = \hat{\nu} C_0 / n_0$ for homogeneous films, $\nu = \hat{\nu} C_{m,0} / \phi n_{p,0}$ for blends, and $\nu = \hat{\nu} S_0 p_{O_2} / \phi n_{R,0}$ for multilayer films, dimensionless

$\hat{\nu}$ stoichiometric coefficient, $\mu\text{mol}_{\text{RS}} / \mu\text{mol}_{\text{O2}}$

$\tau_{rxn,b}$ reactive time scale for polymer blend, $\tau_{rxn,b} = R / 3k_p$, day

$\tau_{rxn,H}$ reactive time scale for homogeneous film, $\tau_{rxn,H} = 1 / k_R n_0$, day

Chapter 7: Parameter Extraction from Experimental Data

7.1 INTRODUCTION

As discussed in the previous chapters, reactive barriers may consist of homogeneous films or composites such as polymer blends or multilayer films. To predict the behavior of any configuration, it is critical to know the physical parameters of the reactive polymer, such as reactive capacity, reaction rate, diffusion coefficient and solubility. This chapter focuses on analyzing experimental data for polybutadiene based oxygen scavenging polymers.

While packaging applications have conditions compatible to permeation experiments, for reactive polymers where initial flux may be too small to measure in typical experimental settings, transient sorption experiments, where the mass uptake of oxygen is monitored over time, maybe the most viable option (Czichos et al. 2006). This chapter focuses on analyzing the data from transient oxygen mass uptake experiments, proposes a model to describe the behavior observed and develops analytical equations to extract the relevant physical parameters from the sorption experiments.

7.2 EXPERIMENTAL DATA

7.2.1 Reactive films

The reactive polymers of interest consist of styrene-butadiene-styrene (SBS) block copolymers, illustrated in figure 7.1, currently being investigated by the Polymer and Membrane groups at the University of Texas at Austin. In particular, this chapter

focuses on copolymer D1102 manufactured by Kraton, since it is currently the focus of study for incorporation into composite barriers due to its processing and reactive properties. Furthermore, this copolymer has been treated with varying concentrations of cobalt neodecanoate catalyst (referred as cobalt from this point forward) to explore the effect of cobalt concentration on scavenging reaction rates.

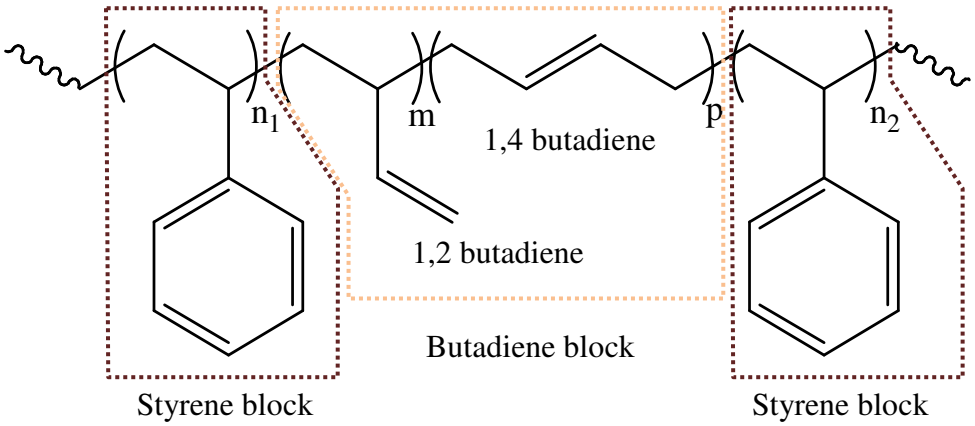

Figure 7.1: Styrene-butadiene-styrene (SBS) block copolymer.

D1102 is a SBS copolymer with 70% (by mass) butadiene content and density of 0.94 g/cm^3. In a polybutadiene polymer, each butadiene block theoretically provides one reactive site that consumes one atom of oxygen each (Beaven and Philips 1974; Li et al. 2008; Li 2010). Since D1102 contains 70% butadiene, the concentration of butadiene monomers is approximately 1.22×10^{-2} mol/cm^3, theoretically being capable of consuming 6.11×10^{-3} moles of O_2 per cm^3 of polymer, or 20.7 grams of O_2 per gram of polymer. In order to make the reaction rates fast enough for practical use in barrier systems, metal catalyst is added.

7.2.2 Measurements

For all data sets evaluated in this chapter, transient sorption experiments were conducted by exposing the scavenging film to a constant oxygen partial pressure (p_{O_2} = 0.21 atm). Mass uptake was monitored by measuring the mass of the film at several points in time, and comparing to the initial mass of the film. The oxygen mass uptake is the difference between the mass of the film at any given time and the mass of the film before exposure to oxygen. To prevent premature oxidation, polymer films were kept free of oxygen (by using an inert environment such as nitrogen) until the beginning of the sorption experiments.

Figure 7.2 shows the mass uptake normalized by the theoretical mass uptake plotted against time. The behavior at early times shows strong dependence on the concentration of cobalt (figure 7.2a, logarithmic scale). On the other hand, at later times, all data sets show very similar results. Figure 7.2b shows the same data in a linear scale, illustrating that the early changes cause a shift in the magnitude of the later portion of the curve (increasing cobalt concentration shifts the curve downwards), but have little influence on its shape.

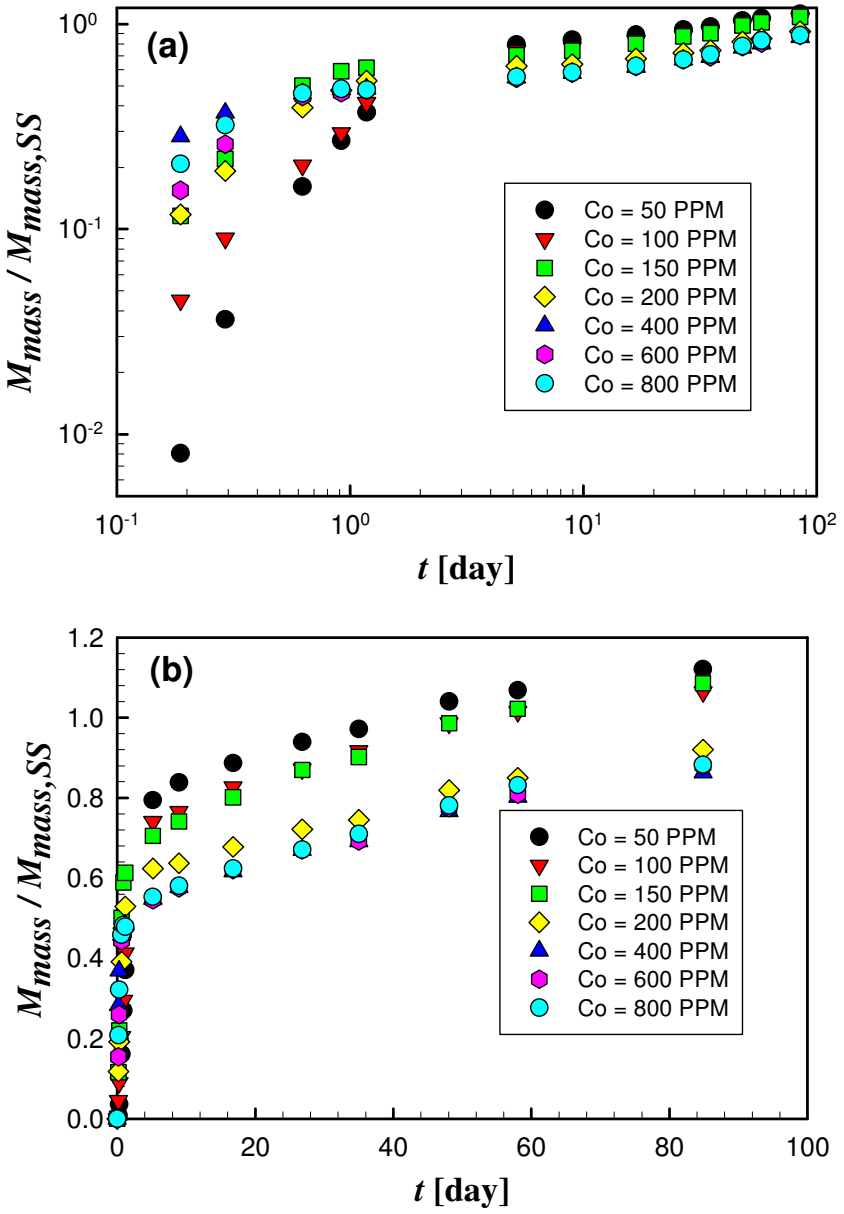

Figure 7.2: Oxygen uptake normalized by theoretical mass uptake versus time for reactive films of various cobalt concentrations, as indicated in chart. (a) data shown in log-log scale, (b) data shown in linear scale. Data courtesy of Kevin Tung, University of Austin, Texas.

Figure 7.3 shows an SEM/EDS image of an oxidized D1102 film, indicating an outer oxidized layer is formed. The formation of an oxidized layer which grows over time as a moving front is also found in polybutadiene films treated with cobalt catalyst (Li 2010). A moving front, as illustrated in figure 7.4, is characteristic of diffusion-controlled reactive systems, where the time scales of diffusion is much greater than the time scale of reaction.

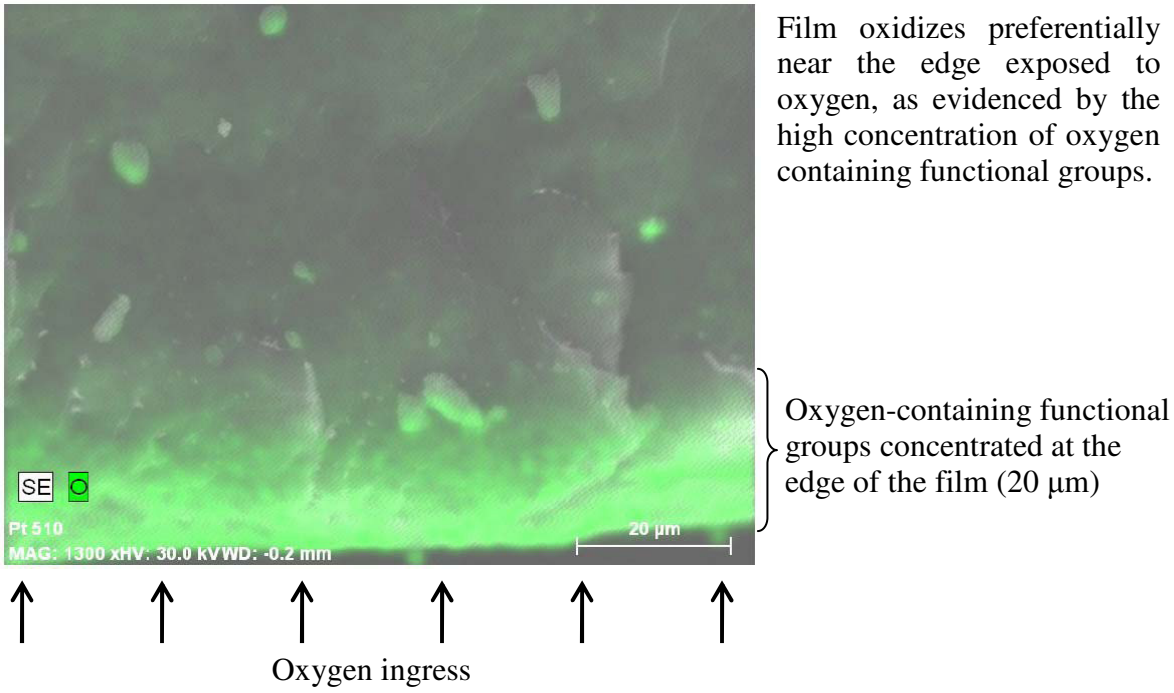

Figure 7.3: SEM/EDS image of D1102 film with 100 PPM cobalt catalyst, 5 days into oxidation. Sample was liquid nitrogen fractured prior to imaging. Image courtesy of Kevin Tung, University of Austin, TX.

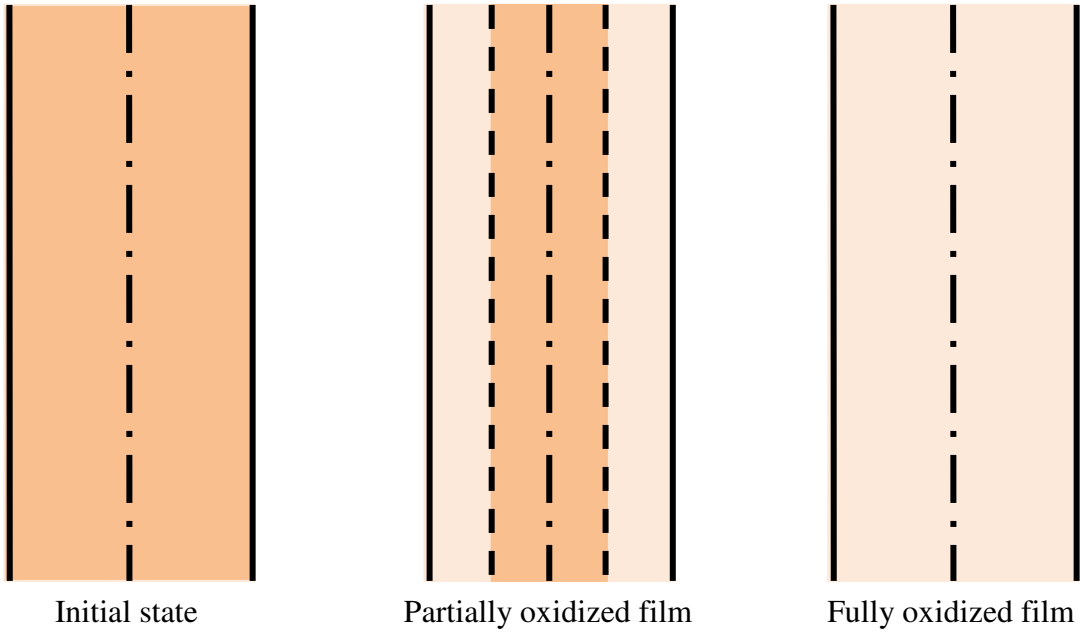

Figure 7.4: Schematic illustration of progressive oxidation. All reactive sites are initially available. Once the film is exposed to oxygen, oxidation is observed on the outer edges, while the film core remains unoxidized. The oxidized layer grows with time, until all reactive sites are consumed.

Note, however, that the experimental curves of figure 7.2 have an apparent secondary time scale that differs from the typical moving front regime and approach to steady-state found in reaction/diffusion systems with constant diffusion coefficient. Experiments with a different SBS polymer (79% butadiene) indicate that oxidation causes the diffusion coefficient to decrease by 2-3 orders of magnitude (Li 2010). The next section proposes a diffusion coefficient that is dependent on the number of reactive sites, and incorporates into the reactive film model.

7.3 MODEL DESCRIPTION

Consider the one-dimensional model of a reactive film of thickness L illustrated in figure 7.4. The film is initially free of oxygen, until it is immersed in an oxygen environment of constant partial pressure p_{O_2}. The immobile reactive sites, with initial concentration n_0, are consumed as the reaction progresses. As discussed in the previous section, the diffusion coefficient of the reactive film significantly decreases as it gets oxidized. This model assumes that the diffusion coefficient can be described as a function of reactive sites which represents the existence of a moving front and the reduction of the diffusion due to oxidation. The variable diffusion coefficient is given by

$$D(n) = D_{un}\frac{n}{n_0} + D_{ox}\frac{(n_0 - n)}{n_0} = D_{un}\left[\frac{n}{n_0}(1-\Delta) + \Delta\right], \tag{7.1}$$

where n is the concentration of available reactive sites at a given time and location within the film, D_{un} is the polymer diffusion coefficient prior to oxidation, D_{ox} is the polymer diffusion coefficient once all reactive sites have been consumed, and $\Delta = D_{ox}/D_{un}$ is the ratio between the diffusion coefficients for the oxidized and unoxidized film. In the limit of a very sharp front, the diffusion coefficient reduces to D_{ox} behind the front (i.e., in the completely oxidized layer), and D_{un} ahead of the front. Oxygen transport through the film is assumed to obey Fick's law with a varying diffusion coefficient. The oxygen concentration at the gas/polymer interface is assumed to obey Henry's law, thus the oxygen concentration at both boundaries is given by $C_0 = S\, p_{O_2}$, where S is the solubility of oxygen in the polymer.

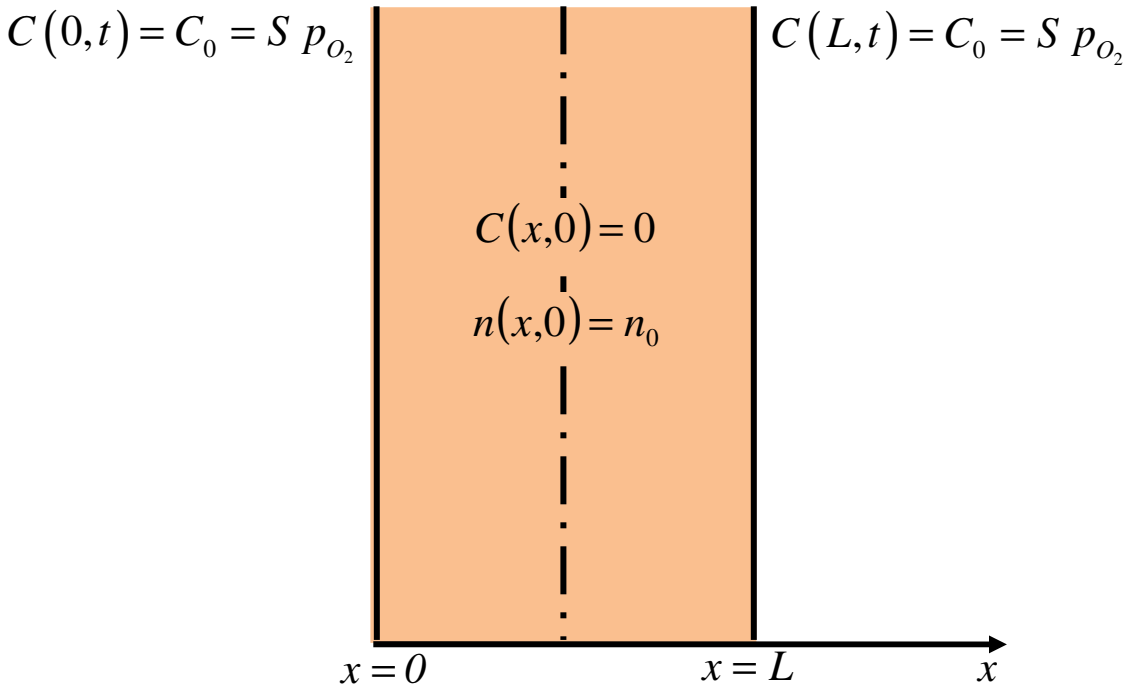

Figure 7.5: Schematic illustration of the reactive film of thickness L. Initially all reactive sites are present with concentration n_0 and the film is devoid of oxygen, until both sides are exposed to oxygen partial pressure.

The transient material balances for oxygen and reactive sites; the initial and boundary conditions are given by

$$\frac{\partial C}{\partial t} = \frac{\partial}{\partial x}\left(D \frac{\partial C}{\partial x} \right) - k_R\, C\, n\,, \tag{7.2}$$

$$\frac{\partial n}{\partial t} = -\hat{\nu}\, k_R\, C\, n\,, \tag{7.3}$$

$$\text{I.C. } C(x,0) = 0, \quad n(x,0) = n_0\,, \tag{7.4}$$

$$\text{B.C. } C(0,t) = C_0 = Sp_{O_2}\,, \quad C(L,t) = C_0 = Sp_{O_2}\,, \tag{7.5}$$

where x is the position along the thickness of the film, t is time k_R is the reaction rate constant and $\hat{\nu}$ is the stoichiometric coefficient for the oxygen scavenging reaction.

For sorption experiments, the uptake of oxygen is monitored over time, and can be calculated in terms of the oxygen flux through surfaces at $x = 0$ and $x = L$. The oxygen flux J at position x and time t is given by

$$J\Big|_x = -\left(D \frac{\partial C}{\partial x} \right)\Big|_x . \tag{7.6}$$

Since both sides are exposed to the same oxygen concentration the flux at both interfaces are of equal magnitude but opposite sign, i.e., $J\Big|_0 = -J\Big|_L$. Thus, the oxygen uptake per unit area at time t can be calculated by doubling the uptake at $x = 0$, making

$$\frac{M_{molar}}{A} = 2\int_0^t J\Big|_0 dt , \tag{7.7}$$

where M_{molar} is the oxygen uptake on a molar basis and A is the area of the film. The oxygen uptake on a mass basis is given by

$$M_{mass} = 64A\int_0^t J\Big|_0 dt . \tag{7.8}$$

Figure 7.6 shows (a) the oxygen flux at $x = 0$ and (b) the mass uptake versus time. For comparison, the plots include computations for fixed diffusion coefficient using the diffusion coefficient of the unoxidized polymer, D_{un}, and the diffusion coefficient of the oxidized polymer, D_{ox}. As illustrated, the early times for the variable diffusion coefficient case match the case for D_{un}, while the case for D_{ox} will match the long times portion.

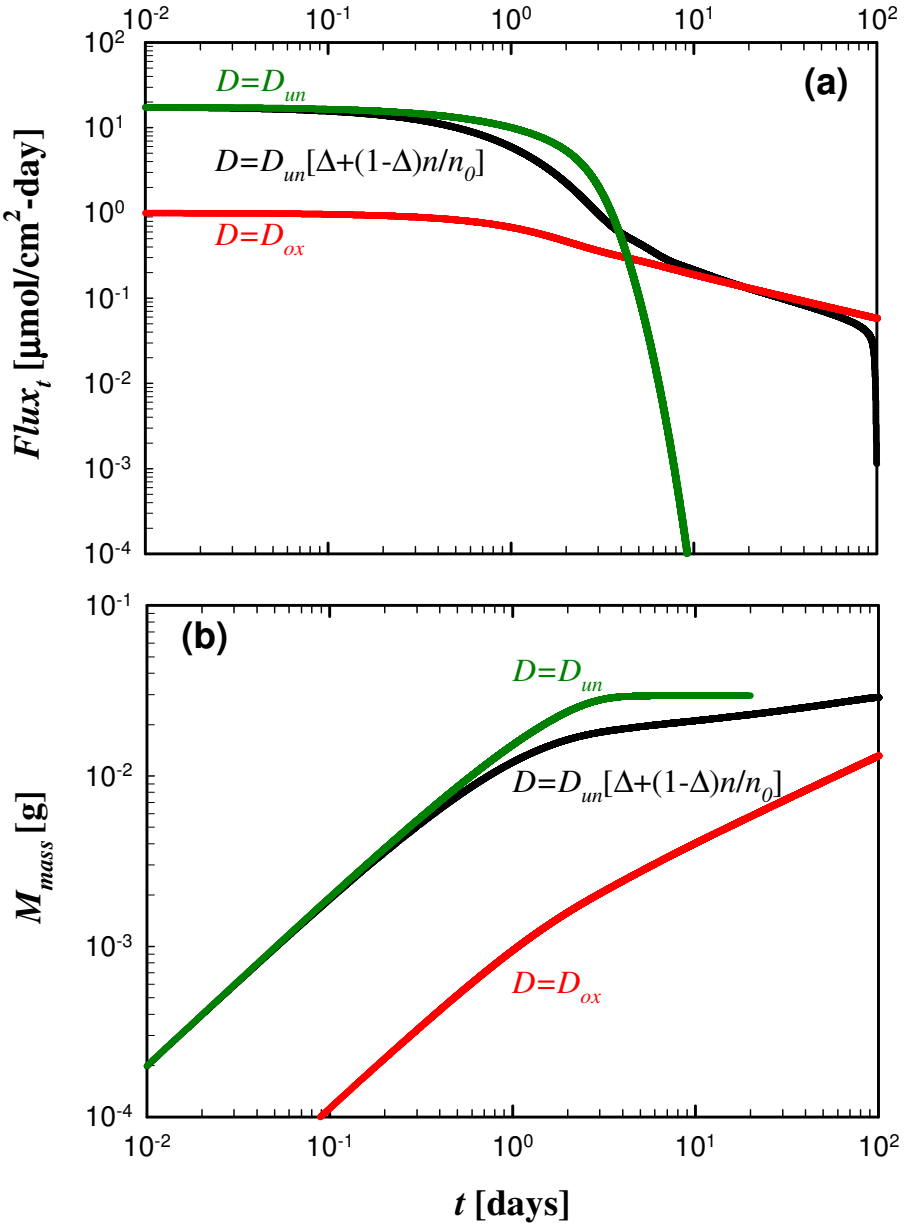

Figure 7.6: (a) Oxygen flux and (b) mass uptake versus time, comparing the cases of constant $D = D_{un}$, constant $D = D_{ox} = \Delta D_{un}$, and varying D, as indicated in the charts. All other parameters are the same for the three cases shown.

7.3.2 Early times

For early times, most reactive sites are still present, i.e., $n \approx n_0$, making $D(n) \approx D_{un}$. Similar to the permeation problems discussed in previous chapters, there is an initial quasi-steady flux plateau. The material balances and boundary conditions thus reduce to

$$0 = \frac{\partial^2 C}{\partial x^2} - \frac{k_R\, n_0}{D_{un}} C\,, \tag{7.9}$$

$$C(0) = C_0\,,\; C(L) = C_0\,. \tag{7.10}$$

Equation 7.9 can be solved analytically to give the concentration profile for early times

$$C(x) = \frac{C_0\left[1-\cosh\left(\Phi_{un}\right)\right]}{\sinh\left(\Phi_{un}\right)}\sinh\left(\Phi_{un}\frac{x}{L}\right) + C_0\cosh\left(\Phi_{un}\frac{x}{L}\right), \tag{7.11}$$

where $\Phi_{un} = \sqrt{L^2 k_R\, n_0 / D_{un}}$ is the Thiele modulus for the unoxidized film, given by the ratio between diffusion and reactive length scales. The flux at $x = 0$ is calculated according to equation 7.6, giving

$$J\big|_0 = \frac{D_{un} C_0}{L}\Phi_{un}\left[\frac{\cosh\left(\Phi_{un}\right)-1}{\sinh\left(\Phi_{un}\right)}\right]. \tag{7.12}$$

Substituting the equation above for flux in equation 7.8 gives the oxygen mass uptake for early times

$$M_{mass} = 64A\frac{D_{un} C_0}{L}\Phi_{un}\left[\frac{\cosh\left(\Phi_{un}\right)-1}{\sinh\left(\Phi_{un}\right)}\right]t\,. \tag{7.13}$$

Equation 7.13 can be more conveniently expressed in terms of the parameter group $c = 64A\frac{D_{un}C_0}{L}\Phi_{un}\left[\frac{\cosh(\Phi_{un})-1}{\sinh(\Phi_{un})}\right]$, giving

$$M_{mass} = c\,t\,. \tag{7.14}$$

7.3.3 Moving front

As discussed in Chapter 2, the moving front for a reactive film of constant diffusion coefficient D is given by $x_F = \sqrt{2\nu Dt}$, and the profiles for the reactive sites collapse into a single curve when plotted versus the moving front coordinate $x - x_F$. Here, it has been determined by inspection of the numerical solution that the reactive site profiles for $0 < x < L/2$ collapse into a single curve when plotted versus $x - x_F$ using $x_F = \sqrt{2\nu D_{ox}t}$, as shown in figure 7.7. Note that for $L/2 < x < L$ the front moves from $x = L$ to $x = L/2$, making the moving front coordinate $L-(x-x_F)$. For a system with constant diffusion, the oxygen uptake in the moving front regime can be calculated by the product between the steady-state mass uptake and the ratio between the moving front position and $L/2$

$$M_{mass} = M_{mass,SS}\left(\frac{2x_F}{L}\right), \tag{7.15}$$

where $M_{mass,SS}$ is the steady-state oxygen uptake on a mass basis (see steady-state analysis). Thus, the mass uptake is proportional to $t^{1/2}$ during the moving front regime.

However, when the diffusion coefficient is not constant, the mass uptake during the moving front shows an offset on the time dependence, given by

$$M_{mass} = M_{mass,SS}\left(\frac{2x_F}{L} + \sqrt{\frac{\tau_{rxn}}{\theta_{0,un}}}\right), \tag{7.16}$$

where $\tau_{rxn} = 1/k_R n_0$ is reaction time scale and $\theta_0 = L^2/6D_{un}$ is the time lag of diffusion for a membrane of thickness L and diffusion coefficient D_{un}. The offset $\sqrt{\tau_{rxn}/\theta_{0,un}}$ was obtained inductively by numerically solving equations 7.2-7.5 and systematically varying each of the parameters.

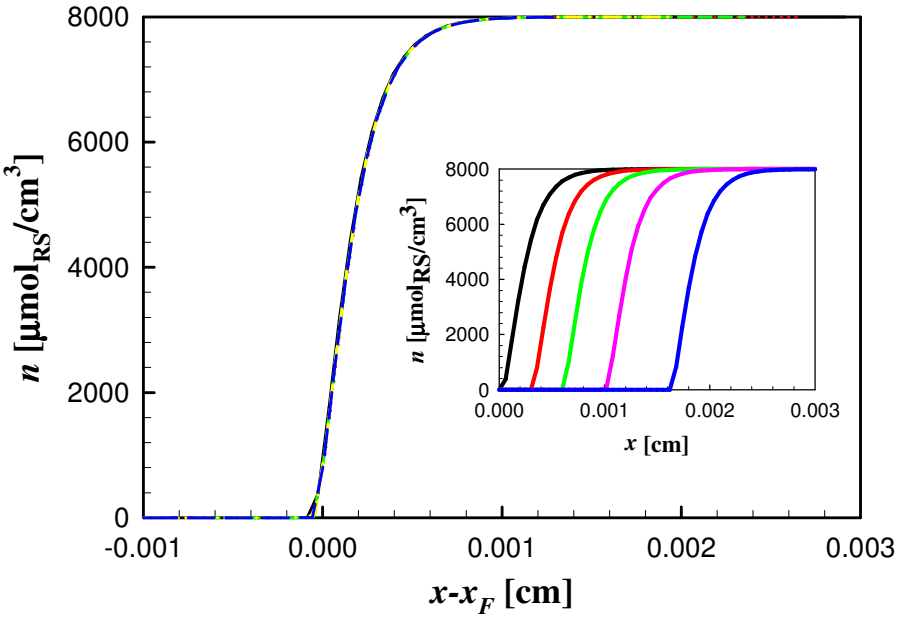

Figure 7.7: Concentration of reactive sites n versus moving front coordinate $x - \sqrt{2\nu D_{ox} t}$ at various times t. Inset shows the concentration profiles plotted against the position along the film x. The profiles for each time collapse into a single curve. All curves shown for half the film, i.e., $0 < x < L/2$.

This prediction matches the moving front regime of the numerical solution of equations 7.2-7.5 quite well, as illustrated in figure 7.8. Equation 7.16 can be expressed more conveniently in terms of the parameter groups $a = M_{mass,SS}\sqrt{6D_{un}/L^2 k_R n_0} = M_{mass,SS}\sqrt{6}/\Phi_{un}$ and $b = \sqrt{4k_R \hat{\nu} C_0 \Delta/3}$, giving

$$M_{mass} = a\left(b\sqrt{t}+1\right). \tag{7.17}$$

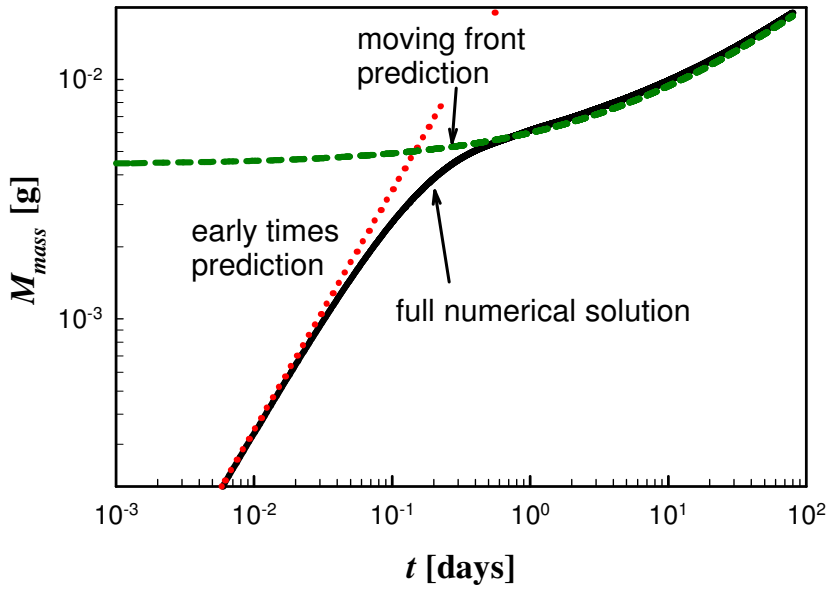

Figure 7.8: Oxygen mass uptake versus time. Numerical solution (solid line) compared to early times (dotted line) and moving front (dashed line) predictions.

7.3.4 Steady state

Here, the steady-state analysis used to calculate time lag in previous chapters is used to calculate the oxygen mass uptake at steady state. Equation 7.2 for oxygen concentration is combined with equation 7.3 for reactive sites concentration,

$$\frac{\partial C}{\partial t} = \frac{\partial}{\partial x}\left(D \frac{\partial C}{\partial x} \right) + \frac{1}{\hat{v}} \frac{\partial n}{\partial t}, \tag{7.18}$$

where D is the variable diffusion coefficient as defined in equation 7.1. Integrating equation 7.18 in space from arbitrary x to L, and subsequently from 0 to L gives

$$\int_0^L \int_x^L \left(\frac{\partial C}{\partial t} - \frac{1}{\hat{v}} \frac{\partial n}{\partial t} \right) dy dx = J\big|_0 \int_0^L dx - \int_0^L D \frac{\partial C}{\partial x} dx, \tag{7.19}$$

where $J\big|_0 = -J\big|_L = \left(D\, \partial C / \partial x \right)\big|_L$. Since the film is exposed to the same concentration at $x = 0$ and $x = L$, at any point in time the flux at any position $0 < x < L/2$ will have a counterpart of opposite sign at $L/2 < x < L$, i.e., $J\big|_x = -J\big|_{L-x}$, making

$$\int_0^L D \frac{\partial C}{\partial x} dx = 0. \tag{7.20}$$

The double integral in the left-hand-side of equation 7.19 can be converted to a single integral by reversal of integration limits, reducing it to

$$\int_0^L \frac{\partial C}{\partial t} dx - \frac{1}{\hat{v}} \int_0^L \frac{\partial n}{\partial t} dx = J\big|_0 L. \tag{7.21}$$

Next, equation 7.21 is integrated from time 0 to t,

$$\int_0^t \int_0^L x \frac{\partial C}{\partial t} dx dt - \frac{1}{\hat{v}} \int_0^t \int_0^L x \frac{\partial n}{\partial t} dx dt = L \int_0^t J\big|_0 dt. \tag{7.22}$$

At very long times all reactive sites are consumed and the oxygen concentration for the entire film is C_0. Evaluating all integrals, using equation 7.7 for oxygen uptake per unit area, and replacing the initial conditions give the steady-state oxygen flux

$$\frac{M_{molar,SS}}{A} = \frac{2}{L}\left(C_0 + \frac{n_0}{\hat{\nu}}\right)\int_0^L x dx = L\left(C_0 + \frac{n_0}{\hat{\nu}}\right). \tag{7.23}$$

The oxygen uptake on a mass basis is given by

$$M_{mass,SS} = 32 A L\left(C_0 + \frac{n_0}{\hat{\nu}}\right). \tag{7.24}$$

Note that for the reactive polymers being studied $n_0/\hat{\nu} \gg C_0$ by several orders of magnitude. In fact, this is one of the characteristics that makes it a viable barrier material, since time lag scales with $1 + 3 n_0/\hat{\nu} C_0$, per discussion in Chapter 2. Thus, the steady-state oxygen uptake may be approximated with very good accuracy by $M_{mass,SS} = 32 A L n_0/\hat{\nu}$.

7.4 FITTING THE EXPERIMENTAL DATA

The analysis of early times, moving front and steady-state regimes were utilized to fit the mass uptake data obtained experimentally. The next sections describe how the data was fit to each regime.

7.4.1 Moving front regime

The least squares method for non-linear equations was used to fit the mass uptake given equation 7.17, i.e., $M_{mass} = a\left(b\sqrt{t} + 1\right)$, where $a = M_{mass,SS}\sqrt{6 D_{un}/L^2 k_R n_0}$ and $b = \sqrt{4 k_R \hat{\nu} C_0 \Delta/3}$, to the moving front portion of the data. The method consists of minimizing the sum of the square of the error E_i at each data point i, where E_i is the

difference between the experimental value M_i and the calculated value (equation 7.17) for each data point, according to the following equations:

$$E = \sum_{i=1}^{m} E_i \,, \tag{7.25}$$

$$E_i = \left[M_i - a\left(b\sqrt{t_i} + 1\right)\right]^2 . \tag{7.26}$$

Figure 7.9 shows the mass uptake obtained experimentally (symbols) and calculated by the moving front prediction (line) versus time. Figure 7.9a shows the results in log scale and figure 7.9b shows the results in linear scale. The prediction is in very good agreement with the experimental data for the moving front portion, as shown in figure 7.9. In fact, all experimental data can be collapsed into a single curve, by plotting $M_{mass}/a - 1$ versus $b\sqrt{t}$, as shown in figure 7.10.

The Thiele modulus of the unoxidized polymer, Φ_{un}, is fully defined in terms of the parameter $a = M_{mass,SS}\sqrt{6}/\Phi_{un}$ and the steady-state oxygen mass uptake, $M_{mass,SS} = 32 A L n_0/\hat{v}$, which is calculated from known quantities such as film area A, film thickness L, and using the theoretical value for concentration of reactive sites as an approximation for the initial concentration (i.e., n_0 = 12200 μmol$_{RS}$/cm^3). The Thiele modulus is thus estimated by

$$\Phi_{un} \equiv \sqrt{\frac{L^2 k_R\, n_0}{D_{un}}} = \frac{\sqrt{6}}{a} M_{mass,SS} \,. \tag{7.27}$$

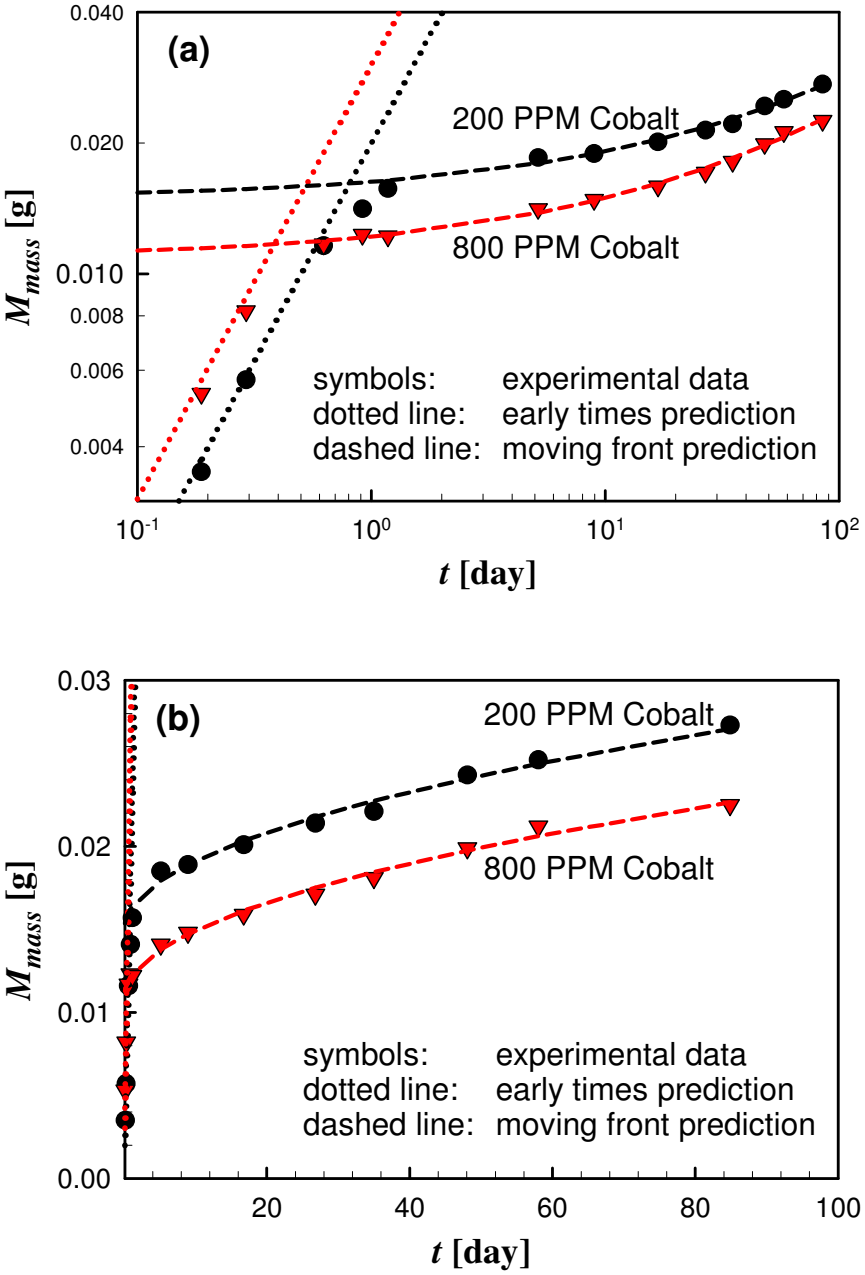

Figure 7.9: Comparison of experimental mass uptake (symbols), early times prediction (dotted lines), and moving front prediction (dashed line), for a film with 200 PPM cobalt catalyst and a film with 800 PPM cobalt catalyst. (a) Mass uptake versus time in log-log scale. (b) Mass uptake versus time on a linear scale.

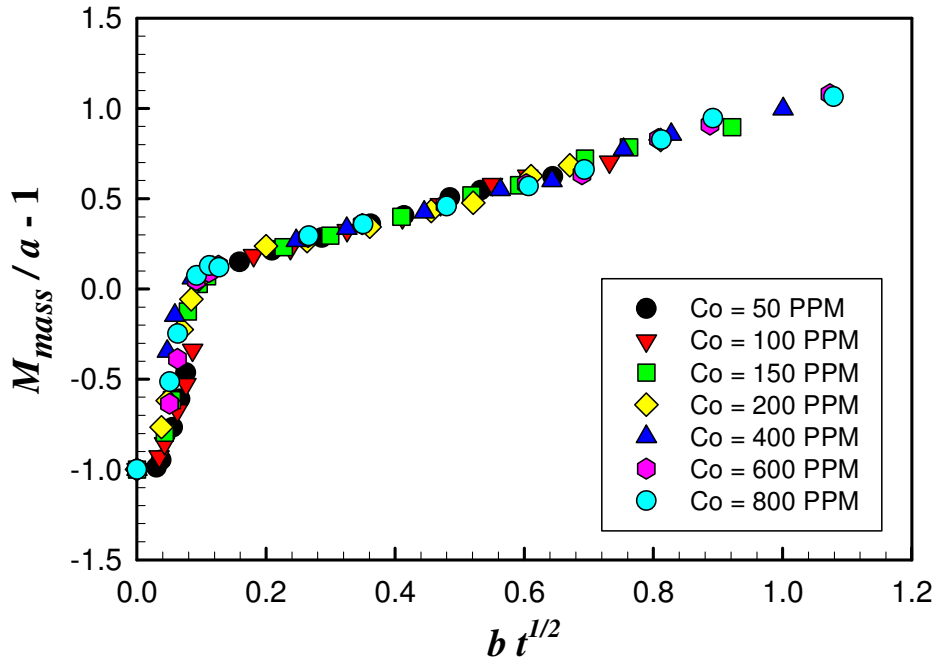

Figure 7.10: Experimental mass uptake normalized by $M_{mass}/a-1$ plotted versus $b\sqrt{t}$, where $a = M_{mass,SS}\sqrt{6}/\Phi_{un}$ and $b = \sqrt{4k_R\hat{\nu}C_0\Delta/3}$ are the parameter groups of the moving front equation 7.17. Experimental data for all cobalt concentrations collapse into a single curve.

Equation 7.27 also gives an expression for reaction the rate k_R in terms of the diffusion coefficient of the unoxidized polymer D_{un},

$$k_R = \frac{6\left(M_{mass,SS}\right)^2}{a^2L^2n_0}D_{un}. \tag{7.28}$$

Replacing equation 7.28 in the definition of parameter b gives an expression for the oxygen concentration C_0 in terms of the diffusion coefficient of the unoxidized polymer D_{un} and the parameter Δ

$$C_0 = \frac{a^2 b^2 L^2}{8\Delta D_{un}\left(M_{mass,SS}\right)^2}\frac{n_0}{\hat{\nu}} \approx \frac{a^2 b^2}{8\Delta D_{un}\left(32A\right)^2\left(n_0/\hat{\nu}\right)}. \tag{7.29}$$

Note that the diffusion coefficient of the unoxidized polymer D_{un} should be the same for all cases, regardless of the concentration of cobalt. On the other hand, the parameter $\Delta = D_{ox}/D_{un}$ requires the measurement of the fully oxidized film, which may be difficult to obtain due to the long time required for full oxidation and because the polymer becomes brittle after oxidation. As discussed next, the early times equation can be used to predict Δ and consequently C_0.

7.4.2 Early times

The quasi-linear oxygen uptake predicted by equation 7.14, $M_{mass} = c\,t$, only occurs at very early times, well before the first data point was collected. Therefore, using least squares to curve fit the data may not result provide accurate parameters. However, it is possible to express the parameter c terms of the parameters a and b which are determined by fitting the experimental data to the moving front equation, and Φ_{un} calculated from the fitting parameters using equation 7.27, leaving only the parameter Δ to be adjusted to fit the data

$$c = ab^2\frac{\sqrt{6}}{4\Delta}\left[\frac{\cosh\left(\Phi_{un}\right)-1}{\sinh\left(\Phi_{un}\right)}\right]. \tag{7.30}$$

The quasi-linear oxygen uptake occurs at very early times, well before the first data point was collected. Therefore, it is not possible to use least squares to curve fit the data, and approximate matching of the data is done for early times.

7.4.3 Summary of results

Table 7.1 summarizes the curve fitting results for all the data sets, listing the parameters a and b for the moving front, c for early times, and the estimation the estimation of k_R and C_0 based on equations 7.28 and 7.29 using parameters indicated in the table. The diffusion coefficient used for all cases (D_{un} = 0.1728 cm^2/day) was based on nitrogen permeation experiments with unreacted films, as an approximation to the diffusion coefficient for oxygen. Note that the theoretical value of n_0 (12,200 μmol$_{RS}$/cm^3) was utilized for all cases and film thickness was calculated based on film mass and density.

Table 7.1: Summary of results from fitting the experimental data to the moving front and early times equations.

Cobalt PPM	a g	b day$^{-0.5}$	c g/s	Δ ND	k_R cm^3/μmol$_{RS}$ day	C_0 μmol$_{O2}$/cm^3	L cm
50	0.017	0.070	0.008	0.0060	3.50	0.09	0.0071
100	0.015	0.079	0.009	0.0065	4.42	0.08	0.007
150	0.014	0.100	0.021	0.0040	5.04	0.19	0.007
200	0.015	0.088	0.020	0.0035	4.60	0.18	0.0085
400	0.012	0.109	0.043	0.0020	7.06	0.31	0.008
600	0.011	0.117	0.023	0.0040	8.12	0.16	0.0076
800	0.011	0.117	0.030	0.0030	8.66	0.20	0.0073

D_{un} = 0.1728 cm^2/day, n_0 = 12,200 μmol$_{RS}$/cm^3 and A = 17.8 cm^2 for all cases

As discussed previously, the determination of parameters a and b for the moving front is completely independent of any parameter choice, as it is done solely by curve fitting equation 7.17 to the moving front portion of the data. The parameter c on the other hand requires the determination of a and b, the knowledge of film dimensions, the knowledge or assumption of n_0 (to determine Φ_{un} per equation 7.27) and the selection of Δ, according to equation 7.30. Note that c determined by this method is proportional to $1/\Delta$ but nearly independent of n_0. A much more robust approach would be to collect enough data points at very early times, so c can be determined by linear regression. Another alternative is to measure the oxygen solubility S (giving $C_0 = Sp_{O_2}$), enabling the determination of Δ, from $b = \sqrt{4k_R \hat{\nu} C_0 \Delta/3}$. If both early times and solubility data are available, the model can be validated by comparing the results from both approaches.

Figure 7.9 shows the dependence of the rate constant k_R on the concentration of cobalt in the reactive film. Except for the anomalous point at 200 PPM, k_R follows a monotonically increasing trend, which can be fitted to a logarithm or power law curve. Recall that k_R was obtained by moving front parameters and estimated values of initial concentration of sites n_0 and the diffusion coefficient D_{un} for the unoxidized film, which are assumed the same for all films, and can be estimated with a reasonable degree of confidence. While the concentration C_0 and Δ vary to some extent in table 7.1, there is no obvious trends and both values are expected to be constant for a given polymer, regardless of catalyst concentration. The variation is likely due to the limited data used for their determination.

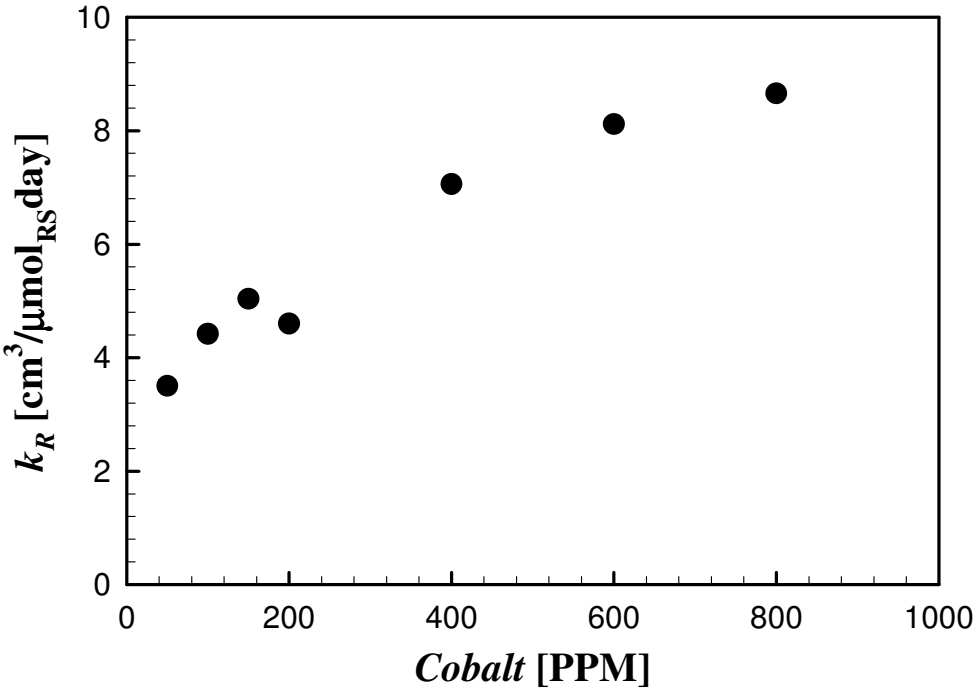

Figure 7.11: Influence of cobalt concentration on the rate constant k_R.

7.5 SUMMARY AND CONCLUSIONS

A one-dimensional model has been developed to describe the transient mass uptake in a diffusion-limited reactive film, where the diffusion coefficient is a function of the number of reactive sites. Analogous to the reactive membrane models described in previous chapters, three regimes were observed. At early times, nearly all reactive sites are still available, and there is a nearly constant oxygen flux into the membrane, making the mass uptake linearly dependent on time. At intermediate times, a moving front is established, with position varying with the square root of time. At long times, all the reactive sites are consumed and the film becomes completely saturated with oxygen.

Analytical expressions were developed to predict mass uptake during each regime. These expressions were used to fit the experimental data. The moving front prediction showed excellent agreement with the experimental data for all data sets. The prediction during early times was limited by the availability of data points at very early times, and in some data sets, due to the time dependence inconsistent with the linear approximation. To get a complete and accurate set of parameters, it is recommended that future sorption experiments collect additional data at early times. Alternatively, measurements of diffusion coefficient and solubility for the unoxidized polymer may be used in conjunction with the moving front equations to estimate the reaction rate constant and the diffusion coefficient of the fully oxidized polymer.

SUPPLEMENTAL MATERIAL - 7.A

Equations 7.2 and 7.3 were discretized using a two-point forward difference for the time derivatives and a three-point central difference for the spatial derivatives, centering accordingly to accommodate the varying diffusion coefficients (Press et al. 2007). The discretized equations are given by

$$\frac{C_j^{m+1} - C_j^m}{\Delta t} = \frac{D_{j+1/2}^m \left(C_{j+1}^m - C_j^m \right) - D_{j-1/2}^m \left(C_j^m - C_{j-1}^m \right)}{\left(\Delta x \right)^2} - k_R \, C_j^m \, n_j^m \,, \tag{7.A.1}$$

$$\frac{n_j^{m+1} - n_j^m}{\Delta t} = -\hat{v} \, k_R \, C_j^m \, n_j^m \,, \tag{7.A.2}$$

where Δt is the time step, Δx is distance between two grid points in space, m is the index for time, and j is the index for the space grid. The diffusion coefficient is given by

$$D_j^m = D_{un} \left[\frac{n_j^m}{n_0} (1 - \Delta) + \Delta \right]. \tag{7.A.3}$$

To obtain $D_{j+1/2}^m$ and $D_{j-1/2}^m$ equation 7.A.3 was evaluated with $n_{j+1/2}^m = \left(n_j^m + n_{j+1}^m \right) \big/ 2$ and $n_{j-1/2}^m = \left(n_j^m + n_{j-1}^m \right) \big/ 2$, respectively.

Nomenclature

a , b , c	parameter groups for curve fitting
C	oxygen concentration in polymer, μmol/cm^3
C_0	oxygen concentration at the surface $C_0 = p_{O_2} S$, μmol/cm^3
D_{un}	diffusion coefficient for oxygen in unoxidized scavenging polymer, cm^2/day
D_{ox}	diffusion coefficient for oxygen in oxidized scavenging polymer, cm^2/day
J	oxygen flux, μmol/cm^2 day
k_R	reaction rate constant, cm^3 /μmol$_{RS}$ day
L	film thickness
n	concentration of reactive sites, μmol$_{RS}$/cm^3
n_0	initial concentration of reactive sites, μmol$_{RS}$/cm^3
p_{O_2}	oxygen partial pressure
M_{mass}	oxygen uptake on a mass basis
M_{molar}	oxygen uptake on a molar basis
RS	subscript in units denotes reactive sites
S	solubility coefficient for oxygen in scavenging polymer, μmol/cm^3 atm
t	time, day
x	position in film, cm
x_F	moving front position, cm

Greek Symbols

β oxygen scavenging capacity, $\beta = n_0 / \hat{\nu}$, $\mu mol_{O2}/cm^3$ OSP

Δ ratio between the oxygen diffusion coefficients for the oxidized and unoxidized polymer, $\Delta = D_{ox} / D_{un}$, dimensionless

θ_0 time lag of diffusion, $\theta_0 = L^2 / 6 D_{un}$, day

Φ_{un} Thiele modulus for the unoxidized polymer, $\Phi_{un} = \sqrt{L^2 k_R n_0 / D_{un}}$, dimensionless

$\hat{\nu}$ stoichiometric coefficient, $\mu mol_{RS} / \mu mol_{O2}$

ν ratio between dissolved oxygen and scavenging capacity, $\nu = \hat{\nu} C_0 / n_0$, dimensionless

τ_{rxn} time scale of reaction, $\tau_{rxn} = 1 / k_R n_0$, day

Chapter 8: Concluding Remarks

8.1 CONCLUSIONS

This dissertation focused on the study of reactive barrier materials through modeling and analysis. Models were developed for reactive homogeneous films, polymer blends and multilayer composites. The reactive term is dependent on both the concentration of the mobile species and the immobilized reactive sites.

The resulting set of non-linear partial differential equations was solved numerically, revealing three distinct regimes associated with early, intermediate and long times. Traditionally, the time lag, which marks the exhaustion of reactive sites at long times and is independent of reaction rate, has been considered the figure of merit when designing reactive membranes. However, the behavior at early and intermediate times is also important when designing barrier materials. Asymptotic analysis of the homogeneous reactive membrane led to development of design equations to predict the barrier performance for each of the three regimes, obviating the need to solving coupled non-linear differential equations.

Based on these results, a multiscale model was developed for polymer blends with reactive particles, and using average effective properties to model the transport thought the whole film. The three regimes observed for homogeneous films were also observed for blends. The methodology developed for homogeneous films was expanded for this system, resulting in predictive equations for each regime. As discussed in Chapter 6, the design equations for blends are very similar to those for homogeneous films. The key

difference is in the definition of the dimensionless parameter groups used in the equations.

Multilayer films, consisting of alternating inert matrix and reactive layers, were also studied. The model was developed in part to enable comparison to the performance of polymer blend, exploring the influence of design parameters such as number of layers and layer ordering on barrier performance. As discussed in Chapter 6, the choice between polymer blends and multilayer composites depend on the properties of the reactive and inert polymers utilized. If the diffusion coefficient of the reactive polymer is much smaller than the diffusion coefficient of the inert matrix, multilayer films will outperform blends. Conversely, polymer blends will outperform multilayer films will outperform blends for cases where the diffusion coefficient of the reactive polymer is greater than the diffusion coefficient of the inert matrix. For intermediate cases, the predictive equations developed can be used to determine the most suitable configuration for a particular application.

This research was motivated by ongoing experimental efforts at the University of Texas to develop and characterize oxygen scavenger materials and composites. As much of the initial material characterization is done via sorption experiments, the development of a model to describe the transient mass uptake in a diffusion-limited reactive film was the focus of Chapter 7. Experimental observation indicated that the diffusion coefficient decreases as the polymer oxidizes, thus the model developed includes a diffusion coefficient that is a function of the number of reactive sites. Analogous to the reactive membrane models described, three regimes were observed. Analytical expressions were developed to predict mass uptake during each regime. The moving front prediction

showed excellent agreement with the experimental data for all data sets. It was difficult to test the early times prediction due to the limited availability of data in the early regime.

8.2 RECOMMENDED AREAS FOR FUTURE RESEARCH

The model developed for the multilayer composite yielded analytical predictions of the initial flux plateau for all layer configurations studied, allowing reactive and inert layers to have different diffusion and solubility coefficients. However, the predictions developed for time lag were not as broadly applicable. Predictions were developed for films of all layer configurations with same diffusion coefficient and same solubility coefficient for all layers. For films with odd numbered total layers, a predictive equation was also developed for films with different solubility and different diffusion coefficient for reactive and inert layers. Thus, an obvious next step would be to develop time lag equations that can be used for all layer configurations and that allow for diffusion and solubility coefficients to be different for inert and reactive layers.

Finally, the model proposed in Chapter 7 to extract parameters from experimental data is based on a diffusion coefficient that varies as the oxygen sites get consumed. However, the models developed in Chapters 2-5 are based on constant diffusion coefficients. Thus, exploring the effect of this model assumption on the predictive equations of 2.5 would determine what adjustments, if any, may be made to the model to accommodate this behavior of the pure scavenging film.

Bibliography

Adam, C., Lacoste, J., Lemaire, J., 1989. Photo-oxidation of elastomeric materials. Part 1-Photo-oxidation of polybutadienes, Polymer Degradation and Stability 24, 185-200.

Ashcraft, D.K., 2007. Fundamental Exploration of Oxygen Scavenging Barrier Systems, M.S. Thesis, The University of Texas at Austin, December 2007.

Bauman, R.G., Maron, S.H., 1956. Oxidation of polybutadiene. I. Rate of oxidation, Journal of Polymer Science 22, 1-12.

Beavan, S.W., Phillips, D., 1974. Mechanistic studies on the photo-oxidation of commercial poly(butadiene), European Polymer Journal 10, 593-603.

Blinka, T.A., Edwards, F.B., Miranda, N.R., Speer, D.V., Thomas, J.A., 1998. Zeolite in packaging film, U. S. Patent 5,834,079, assigned to W. R. Grace.

Burrows, P.E., et al., 2001. Gas permeation and lifetime tests on polymer-based barrier coatings, Proceedings of SPIE, 4105, 75-83.

Cahill, P.J., Chen, S.Y., 2000. Oxygen scavenging condensation copolymers for bottles and packaging articles, U. S. Patent 6,083,585, assigned to BP Amoco Corporation.

Carranza, S., Paul D.R., Bonnecaze, R.T., 2010a. Design formulae for reactive barrier membranes. Chemical Engineering Science 65 (3), 1151-1158.

Carranza, S., Paul, D.R., Bonnecaze, R.T., 2010b. Analytic formulae for the design of reactive polymer blend barrier materials. Journal of Membrane Science 360, 1-8.

Choi, M.C., Kim, Y., Ha, C.S., 2008. Polymers for flexible displays: from material selection to device applications, Progress in Polymer Science 33, 581-630.

Cochran, M.A., Folland, R., Nicholas, J.W., Robinson, E.R., 1991. Packaging, U.S. Patent 5,021,515, assigned to CMB Foodcan.

Coles et. al., Eds., 2003. Food packaging technology, page 70

Coquillat, M., Verdu, J., Colin, X., Audouin, L., Nevière, R., 2007a. Thermal oxidation of polybutadiene. Part 1: Effect of temperature, oxygen pressure and sample thickness on the thermal oxidation of hydroxyl-terminated polybutadiene, Polymer Degradation and Stability 92, 1326-1333.

Coquillat, M., Verdu, J., Colin, X., Audouin, L., Nevière, R., 2007b. Thermal oxidation of polybutadiene. Part 2: Mechanistic and kinetic schemes for additive-free non-crosslinked polybutadiene, Polymer Degradation and Stability 92, 1334-1342.

Coquillat, M., Verdu, J., Colin, X., Audouin, L., Nevière, R., 2007c. Thermal oxidation of polybutadiene. Part 3: Molar mass changes of additive-free non-crosslinked polybutadiene, Polymer Degradation and Stability 92, 1343-1349.

Crank, J. 1975. The Mathematics of Diffusion, 2nd Ed., Oxford University Press, Oxford.

Czichos, H.; Saito, T.; Smith, L.M. (Eds.), 2006. Springer Handbook of Materials Measurement Methods, pp.371-387

Do, D.D., 1982. On the validity of the shrinking core model in noncatalytic gas solid reaction, Chemical Engineering Science, 37 (10), 1477-1481.

Ferrari, M.C., Carranza, S., Bonnecaze, R.T., Tung, K.K., Freeman, B.D., Paul, D.R., 2009. Modeling of oxygen scavenging for improved barrier behavior: Blend films. Journal of Membrane Science 329, 183–192.

Finger, K.F, Lemberger, A.P., Higuchi, T., Busse, L.W., Wursten, D.E., 1960. Investigation and development of protective ointments. IV The influence of active fillers on the permeability of semisolids, Journal of the American Pharmacists Association 49, 569-573.

Fogler, H.S., 1999. Elements of Chemical Reaction Engineering, 3rd Ed., Prentice Hall, Upper Saddle River, NJ.

Frisch, H.L., 1957. The time lag in diffusion. The Journal of Physical Chemistry 61, 93–95.

Gillen, K.T., Clough, R.L., 1992. Rigorous experimental confirmation of a theoretical model for diffusion-limited oxidation, Polymer, 33 (20), 4358-4365.

Hodge, K., Prodpran, T., Shenogina, N.B., Nazarenko, S., 2001. Diffusion of oxygen and carbon dioxide in thermally crystallized syndiotactic polystyrene, Journal of Polymer Science Part B: Polymer Physics 39, 2519-2538.

Hui, H.Y., Editor, 2005. Handbook of Food Science, Technology, and Engineering, Volume 3, Chapter 131

Ivanov, V.B., Burkova, S.G., Morozov, Y.L., Shlyapintokh, V.Y., 1979. Kinetics of the chain-propagation and chain-termination reactions in the oxidation of polybutadiene and copolymers of butadiene with styrene, Kinetika i Kataliz, 20 (5) 1330-1333.

Katsumoto, K., Ching, T.Y., 1998. Multi-component oxygen scavenging composition, U. S. Patent 5,776,361, assigned to Chevron Chemical Company.

Lape, N.K., Yang, C., Cussler, E.L., 2002. Flake-filled reactive membranes, Journal of Membrane Science 209, 271-282.

Lehto, V.P., Lankinen T., 2004. Moisture transfer into medicament chambers equipped with a double-barrier-desiccant system. International Journal of Pharmaceutics 275, 155–164

Levenspiel, O., 1999. Chemical Reaction Engineering, 3rd Ed., John Wiley & Sons, New York (1999).

Lewis, J., 2006 Material challenge for flexible organic devices, Materials Today 9, 38-45.

Li, H., 2010. Metal-Catalyzed Oxidation of Polybutadiene in Oxygen Scavenging Packaging Applications, Ph.D. Dissertation.

Li, H., Ashcraft, D.K., Freeman, B.D., Stewart, M.E., Jank, M.K., Clark, T.R., 2008. Non-invasive headspace measurement for characterizing oxygen scavenging in polymers, Polymer, 49, 4541-4545.

Maxwell, J.C., 1873. Treatise on Electricity and Magnetism, Vol. I, p.365, Oxford University Press, London.

Mueller, C.D., Nazarenko, S., Ebeling, T., Schuman, T.L., Hiltner, A., Baer, E., 1997. Novel structures by microlayer coextrusion—Talc-filled PP, PC/SAN, and HDPE/LLDPE, Polymer Engineering and Science. 37 (2), 355-362.

Ng, E.P., Mintova, S., 2008. Review: nanoporous materials with enhanced hydrophilicity and high water sorption capacity. Microporous and Mesoporous Materials 114, 1–26

Nuxoll, E.E., Siegel, R.A., Cussler, E.L., 2005. Layered reactive barrier films, Journal of Membrane Science 252, 29-36.

Nuxoll, E.E., Cussler, E.L., 2005. The third parameter in reactive barrier films. AIChE Journal 51 (2), 456–463.

Paul, D.R., 1969. The effect of immobilizing adsorption on the diffusion time lag. Journal of Polymer Science 7A-2, 1811–1818.

Paul, D.R., Bucknall, C.B., (Eds.), 2000. Polymer Blends, Vol. 1, Formulation, John Wiley, New York.

Paul, D.R., Kemp, D.R., 1973. The diffusion time lag in polymer membranes containing adsorptive fillers. Journal of Polymer Science 41C, 79-93.

Paul, D.R., Koros, W.J., 1976. Effect of partially immobilizing sorption on permeability and the diffusion time lag. Journal of Polymer Science: Polymer Physics Edition 14, 675-685.

Piton, M., Rivaton, A., 1996. Photooxidation of polybutadiene at long wavelengths ($\lambda >$ 300 nm), Polymer Degradation and Stability 53, 343-359.

Polyakova, A., Liu, R.Y.F., Schiraldi, D.A., Hiltner, A., Baer, E., 2001. Oxygen-barrier properties of copolyesters based on ethylene terephthalate, Journal of Polymer Science Part B: Polymer Physics 39, 1889-1899.

Press, W.H., Teukolsky, S.A., Vetterling, W.T., Flannery, B.P., 2007. Numerical Recipes: The Art of Scientific Computing, Third Edition, Cambridge University Press, New York, NY, page 1046.

Rabek, J.F., Lucki, J., Rånby, B., 1979. Comparative studies of reactions of commercial polymers with molecular oxygen, singlet oxygen, atomic oxygen and ozone-I, European Polymer Journal 15, 1089-1100.

Rincon-Rubio, L.M., Fayolle, B., Audouin, L., Verdu, J., 2001. A general solution of the closed-loop kinetic scheme for the thermal oxidation of polypropylene, Polymer Degradation and Stability 74, 177-188.

Russ J.C., Dehoff, R.T., 2000. Practical Stereology, 2nd ed., Kluwer Academic/Plenum Publishers, New York, 2000.

Sheldon, R.A., Kochi, J.K., 1981. Metal-Catalyzed Oxidations of Organic Compounds, Academic Press: New York, 1981.

Siegel, R.A., 1991. Algebraic, differential, and integral relations for membranes in series and other multilaminar media: permeabilities, solute consumption, lag times, and mean first passage times. The Journal of Physical Chemistry 95 (6) 2556-2565.

Siegel, R.A., Cussler, E.L., 2004. Reactive barrier membranes: some theoretical observations regarding the time lag and breakthrough curves. Journal of Membrane Science 229, 33–41.

Siegel, R.A., Cussler, E.L., 2005. Layered reactive barrier films, Journal of Membrane Science 252, 29-36.

Solovyov, S.E., Goldman, A.Y., 2005a. Theory of transient permeation through reactive barrier films I. Steady state theory for homogeneous passive and reactive media. International Journal of Polymeric Materials 54, 71-91.

Solovyov, S.E., Goldman, A.Y., 2005b. Theory of transient permeation through reactive barrier films II. Two layer reactive-passive structures with dynamic interface. International Journal of Polymeric Materials 54, 93-115.

Solovyov, S.E., Goldman, A.Y., 2005c. Theory of transient permeation through reactive barrier films III. Solute ingress dynamics and model lag times. International Journal of Polymeric Materials 54, 117-139.

Solovyov, S.E., Goldman, A.Y., 2006a. Optimized design of multilayer barrier films incorporating a reactive layer I. Methodology of ingress analysis, Journal of Applied Polymer Science 100, 1940-1951.

Solovyov, S.E., Goldman, A.Y., 2006b. Optimized design of multilayer barrier films incorporating a reactive layer II. Solute dynamics in two-layer films, Journal of Applied Polymer Science 100, 1952-1965.

Solovyov, S.E., Goldman, A.Y., 2006c. Optimized design of multilayer barrier films incorporating a reactive layer III. Case analysis and generalized multilayer solutions, Journal of Applied Polymer Science 100, 1966-1977.

Solovyov, S.E., Goldman, A.Y., 2008. Mass Transport Reactive Barriers in Packaging, DEStech Publications, Lancaster, PA, 2008.

Speer, D.V., Morgan, C.R., Roberts, W.P., 1993. Methods and compositions for oxygen scavenging, U.S. Patent 5,211,875, assigned to W. R. Grace.

Speer, D.V., Roberts, W.P., Morgan, C.R., VanPutte, A.W., 1996. Multilayer structure for a package for scavenging oxygen, U. S. Patent 5,529,833, assigned to W. R. Grace.

Stewart, M.E., Estep, R.N., Gamble, B.B., Clifton, M.D., Quillen, D.R., Buehrig, L.S., Govindarajan, V., Dauzvardis, M.J., 2006. Blends of oxygen scavenging polyamides with polyesters which contain zinc and cobalt, U. S. Patent Application Publication US 2006/0148957, assigned to Constar International Inc., Eastman Chemical Company.

Thomas, G., Goringe, M.J., 1979. Transmission Electron Microscopy of Materials, Wiley, New York, 1979.

Tobolsky, A.V., Metz, D.J., Mesrobian, R.B., 1950. Low temperature autoxidation of hydrocarbons: the phenomenon of maximum rates, Journal of the American Chemical Society 72, 1942-1952.

Tung, K.T., 2010. Unpublished data.

Yang, C., Cussler, E.L., 2001. Oxygen barriers that use free radical chemistry. AIChE Journal 47 (12) 2725-2732.

Yang, C., Nuxoll, E.E., Cussler, E.L., 2001. Reactive barrier films. AIChE Journal 47 (2) 295-302.

Vita

Susana Carranza was born and raised in Brazil, where she completed her undergraduate studies in Chemical Engineering at UNICAMP, in Campinas, Brazil. After college, she worked for 3M in Brazil for a couple of years, got married, moved to California, and returned to school to pursue a master's degree in Mechanical Engineering at the California State University, Chico, CA. Susana was hired by Makel Engineering in 1998 and continued working while pursuing her doctoral degree in Chemical Engineering at the University of Texas at Austin.

Permanent e-mail: scarranza@austin.rr.com

This dissertation was typed by the author.